UNIVERSITAT DE BARCELONA

Rheological Characterization of Healthy and non-Healthy Blood using Electronic Detection of the Fluid Front

Lourdes Méndez-Mora

Doctoral thesis

Rheological Characterization of Healthy and non-Healthy Blood using Electronic Detection of the Fluid Front

Author: Lourdes Méndez-Mora

Directors:

Dr. Aurora Hernández-Machado

Dr. Tomás Alarcón Cor

UNIVERSITAT DE BARCELONA

Rheological Characterization of Healthy and non-Healthy Blood using Electronic Detection of the Fluid Front

Tesis presentada para optar por el título de doctor por la Universidad de Barcelona

Programa de doctorado en Ingeniería y Ciencias Aplicadas

Autor: Lourdes Méndez-Mora

Directores:

Dr. Aurora Hernández Machado

Dr. Tomás Alarcón Cor

Tutor: Dr. Mauricio Moreno Sereno

Barcelona, España

2024

UNIVERSITAT DE BARCELONA

rheological variations with respect to the properties of the normal blood. To avoid effects of hematocrit levels in the results, we employ a mathematical model to normalize blood viscosity of different samples according to their plasma viscosity. In this case, we analyze samples from patients with beta-thalassemia traits (β-TT) and iron deficiency anemia (IDA), two diseases in which red blood cell volume and deformability are affected. Additionally, the results we obtain are compared to the Laser Optical Rotational Red Cell Analyzer (LORRCA), the gold standard for single cell deformability analysis.

Moreover, we studied the effects caused by changes in tonicity, by adding deionized water (DIW) and sodium chloride (NaCl) to blood samples from healthy donors. In this occasion, however, we designed a new geometry of the PDMS channels, so they feature four different width sizes. This is done to obtain a normalized curve of viscosity at different shear rate values in one single experiment, as opposed to obtaining one single shear rate for each experiment. We have presented a method and a mathematical model that allows us to obtain a viscosity curve in one single experiment, with the accuracy of previous results. Blood viscosity is changed when the RBC is altered, our results show that DIW causes blood to have more non-Newtonian behavior. Inversely, NaCl causes the sample to become a hypertonic solution, causing the red blood cells to create, producing a more Newtonian behavior in blood. In addition, we have been able to observe images of the effects of crenation and rupture of the RBC when the tonicity is changed.

Subsequently, we continue our research in the field of malaria infected blood samples. Here, we apply a lab-on-a-chip approach to study red blood cells infected by malaria. To conduct the experiments, we constructed two models of microfluidic channels with micro slits of 2 µm, emulating the process of pitting that takes place in the spleen when a malaria infection is present. These microfluidic channels emulate fluidic performance in living organs. The deformability capability of RBCs is altered during the infection state of rings, in which a parasite is inside the RBC, causing an increase in the cell wall rigidity. Using this experimental approach, we characterized *plasmodium falciparum*-infected RBCs (P.f.-RBCs) after their passage through the devices, determining hemolysis and the proportion of once-infected RBCs (O-iRBCs), by detecting the presence of a parasite antigen and absence of 4’,6-diamidino-2-phenylindole

(DAPI) staining of parasite DNA using a flow cytometer. The passage of P.f.-RBCs through the devices at the physiological flow rate did not affect cell integrity and resulted in an increase of the amount of detected O-iRBCs. Both microfluidic device models could replicate the pitting of P.f.-RBCs ex vivo through mechanical constraints without cellular involvement, casting new light on the function of the spleen in the pathophysiology of malaria. Furthermore, we did an invited review on the current data of these frontier technologies in malaria, giving more attention to the major challenges to the study of *plasmodium vivax* cryptic infections.

As part of the research, we also present results obtained during our work that have not yet been published. We conducted experiments to test the capacity of our microrheometer for industrial applications. For this, we conducted rheology experiments and obtained the viscosity of different dilutions of hyaluronic acid (HA) and sodium alginate (SA) in DIW. As a result, we obtained viscosity of the shear thinning type, which increased when the concentration was augmented. Regarding the fabrication of microfluidic channels, we tested a method to change the wettability of the surface of the internal walls of a PDMS microfluidic channel. Normally, cured PDMS is hydrophobic. In this test, we achieved a change in the contact angle of water drops on the surface of PDMS that could be sustained for more than 24 hours, therefore turning PDMS from hydrophobic to hydrophilic. We did this using a plasma treatment in the clean room, which proved to be fast, easy, and stable enough method to be used in future applications where hydrophilic PDMS channels would be of use.

Table of Contents

List of figures

PART I

General Introduction

1.1. Introduction to microfluidics

Microfluidics consists in various techniques used for the processing and analysis of small samples of fluid, in the range of 10^{-9} to 10^{-18} liters, by using channels with dimensions of tens to hundreds of micrometers [1]. The application of microfluidics brings in the advantages of using small sample amounts, require little laboratory space, allow for high throughput screening, at a low cost with high accuracy and in relatively short times [2]. Another important advantage, is the unique flow characteristics and field properties that are achieved at the micro scale (e.g. laminar flow, enhanced surface effects)[3]. The scaling down of geometric features also enables confinement of deformable particles such as drops, bubbles, polymer chains, and biological cells [4], [5].

1.2. Fabrication techniques and materials for microfluidics

According to Whitesides, microfluidics started with four main applications: molecular biology, molecular analysis, national security, and microelectronics [1], [6]. Here, we are especially interested in the path took by microelectronics and its relation to microfluidics. This was specifically applied in silicon microelectronics, and in microelectromechanical systems (MEMS), to be directly applicable to microfluidic channels. The initial applications were usually made of silicon and glass. However, this was rapidly replaced by a wide range of materials that include not only silicon/glass combinations, but also elastomers, thermosets, thermoplastics and even hydrogels and paper based materials [7]. Polymer-based materials such as Polydimethylsiloxane (PDMS), are optically clear, biocompatible, flexible, and hydrophobic [8]. PDMS is a silicon-based hybrid organic/inorganic polymer consisting of an inorganic -Si-O- backbone and organic component side

chain. The special organic/inorganic structure provides PDMS with excellent physicochemical properties, such as optical transparency, hydrophobicity, chemical inertness, permeability, non-toxicity and good biocompatibility. In addition, PDMS is chemically and mechanically robust with good flexibility and ease of prototyping as well as having a low cost [9]. Thanks to these properties, it has been successfully used in a variety of applications from microfluidics [1], to protective coatings [10].

These new materials allow for fast prototyping of microfluidic structures, with high quality and at a relatively low cost [11]. PDMS can be modified by different techniques such as lithography (photo-, soft- and X-ray-), printing technology (3D), mechanical micro cutting, micro milling, direct laser plotting etc. [12] Another advantage of using PDMS is that its hydrophobicity can be modified by using plasma treatment [13] or by combining this with the use of silanes [14]. Most of these processes can be carried out in laboratory set-ups within clean room facilities with readily available equipment.

Conversely, for applications that require wall rigidity, polystyrene (PS), polycarbonate (PC), poly (methyl methacrylate) (PMMA), cyclic olefin copolymer (COC), poly (ethylene terephthalate) (PET), polypropylene, and polyvinyl chloride (PVC) are more commonly used [15]. For these reasons, many microfluidic applications for biological fluids and cells make use of these novel materials [16]–[18].

In this work, we employ soft lithography techniques for the design and fabrication of microfluidic channels made of PDMS. Photolithography is a cheap and reliable process in which a photo-sensitive resin is exposed to a controlled UV light to obtain a cast to replicate microfluidic channels from [19], [20]. The fabrication process starts with a photomask design and mask printing. Then, we continue in the lab with the coating of a photo resin layer on a silicon wafer, followed by the photo resin baking, mask alignment and UV light exposure. Finally, the resulting structures are washed during the development process. A post-bake is often necessary to ensure the mechanical properties of the newly formed structures is stable and could stand several uses [21]. The photo resin of our choice is SU-8, a negative resin. This means that once spread on a silicon wafer, the parts not covered by the photomask and exposed to a UV source will remain after the development[22]. This resin is often used in the fabrication of cast microfluidic channels [23], [24].

For the fabrication of electrodes, a similar process is followed. Normally, the photo-resin used is AZ 5214. This resin has the resolution needed to ensure that the heigh of electrodes is in the tenths of micrometers. The lift off soft photolithography technique was used to fabricate parallel-plate electrodes [20]. Gold (Au) ions were decomposed on the glass surface with appropriate dimensions to obtain the desired structure of the parallel electrodes. Initially, the glass surface was coated with photoresist AZ 5214 and the pattern of the electrodes is obtained by exposing the photoresist under UV light. A developer is used to reveal the pattern on the glass surface. Next, the conductive material for the electrodes, in our case gold (Au), is then sputtered onto the patterned glass surface. An ultrasonic bath is used to clean the resin and leave only the remaining Au electrodes on the surface [25].

It is our purpose to explain these two thoroughly, in the second part of this introduction, since the main aspects of this work are reliant on the fabrication techniques that enabled the experimental setup used to obtain the results using the microrheometer.

1.3. Model for microfluidic flow in two dimensions

Rheology is the science that studies the flow and deformation of a material [26]. It analyzes how materials deform and flow as a result of an external force [27]. The name was coined by Eugene Bingham, who founded the Society of Rheology in the USA, and its root lies in the Greek word for flow [26]. A rheometer is an instrument for measuring the rheological properties of a fluid by applying a flow to the material and measure the subsequent force generated, or by applying a force mode to a material and then measuring its deformation [28], [29]. Rheometers are typically used in industries where rheological characteristics are fundamental for the transportation, storage and handling of the goods being produced, i.e., paints, food and beverages, cosmetics, etc. There are two basic types of rheometers: rotational also called of the shear type, and capillary extrusion. Capillary extrusion is normally

used for relatively concentrated suspension/pastes while the rotational design is for relatively less concentrated suspensions.

To describe the mechanical motion of an incompressible viscous fluid, the Navier-Stokes equation [30] gives us the most general description:

$$\rho\left[\frac{\partial\,\vec{v}}{\partial t}+(\vec{v}\cdot\nabla)\vec{v}\right]=\rho\vec{f}-\nabla p+\eta\nabla^2\vec{v} \qquad (1)$$

Where $\vec{v}=(v_x,v_y,v_z)$ represents a three-dimensional velocity field, ρ is the density of the fluid, η is the dynamic viscosity, p is the pressure in the fluid and $\vec{f}$ are the forces applied to the fluid. This is mainly due to the non-linear term, $(\vec{v}\cdot\nabla)\vec{v}$. In a one-dimensional flow, the velocity field of the fluid points in a single direction, and the nonlinear term becomes negligible. When the velocity field is stationary, the movement of fluid particles results from the balance between the pressure gradient and the viscous friction forces [31]. To explain this, we describe the one-dimensional flow in a plane Couette flow, shown in Figure 1. This originates between two parallel planes, separated at a distance b, while the upper plate moves parallel to itself at constant velocity V. This can be described with equation (2).

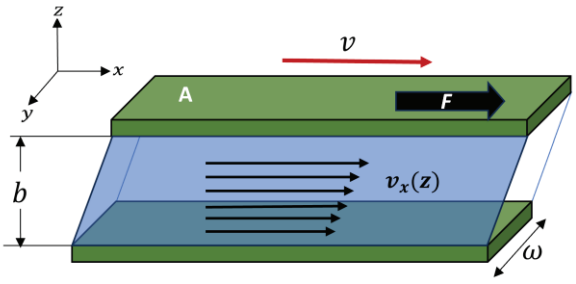

Figure 1. Diagram of a plane Couette flow describing the velocity gradient or shear rate, $\dot{\gamma}_{xz}=\frac{dv_x}{dz}$, of a steady shear flow. Our microchannel satisfies $\frac{b}{\omega}<<1$.

$$|\sigma_{xz}|=\eta\frac{\partial v_x}{\partial z}=\eta\frac{v}{b} \qquad (2)$$

Now, consider a microfluidic channel with a rectangular cross section, of height b, width ω , and the total length of the channel, L_c, as depicted in Figure 2.

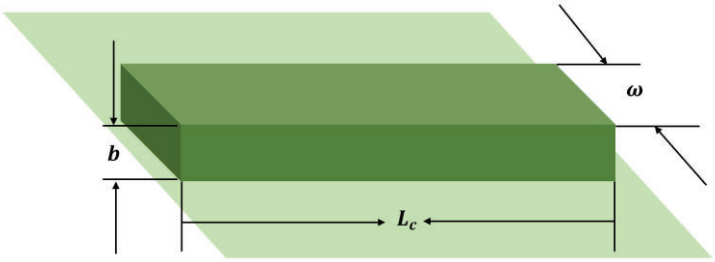

Figure 2. Schematic of the microfluidic channel.

A viscous fluid flowing inside the channel, behaving as the flow between two parallel plates at a distance b, can be described as a Poiseuille flow, Q_c and can be written as:

$$Q_c = \frac{\Delta P}{12\eta}\frac{b^3}{L_c} \tag{3}$$

The microchannel is connected to a cylindrical tube of length L_t, and radius R, as the one depicted in Figure 3. A Poiseuille flow states that the velocity profile of a flow moving inside a tube, Q_t can be written as:

$$Q_t = \frac{\Delta P}{8\eta}\frac{\pi r^4}{L_t} \tag{4}$$

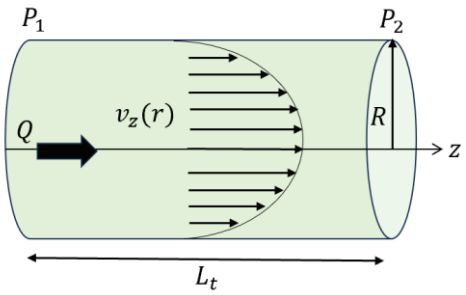

Figure 3. Diagram of a Poiseuille flow inside the tubing connected to the microfluidic channel. The velocity $v_z(r)$ of the flow Q_t in the direction z is represented by the arrows of the flow profile. The pressure difference is $\Delta P = P_2 - P_1$.

1.4. Flow at the microscale of Newtonian and Non-Newtonian fluids

Viscosity is the opposition of a material poses to flow [32]. The viscosity of fluids can be described by mainly two behaviors, which are Newtonian and non-Newtonian viscosity behavior. A Newtonian fluid shows a viscosity that follows a linear relationship with the shear applied. They flow proportionally to the stress they are put under and can be characterized with a single constant viscosity value. Water is the best example of a Newtonian fluid [33]. With a constant viscosity around $1\ mPa \cdot s$ at room temperature, it is very useful for calibration [34].

1.5. Rheology of the fluid front

The Reynolds number is important for describing the transport properties of a fluid or a particle moving in a fluid. It correlates the inertia forces to the viscous forces. [35], [36]. The Reynolds number was first described by Reynolds in 1883 [37] although others have used the quantity before, e.g., Stokes [5]. It can be defined as non-dimensional parameter obtained a function of the density ρ, the shear viscosity of a fluid, is velocity v inside a channel of height b. It can be written as:

$$Re = \frac{\rho v b}{\eta} \tag{5}$$

Laminar flow is closely related to the Reynolds number, which is one of the most important dimensionless quantities in microfluidics. Laminar flow is a type of fluid flow in which fluid particles move in parallel layers without mixing or generating turbulence. In laminar flow, layers of fluid slide smoothly over each other, and particles move along uniform, predictable paths. This type of flow is common in situations where the fluid moves at low speed and in small pipes or tubing, such as microfluidic channels. A low Reynolds number, Re < 2000, the flow is generally laminar, which is of our interest, since is the type of flow inside structures at the micro scale.

At the microfluidic level, the values of b and v are in the order of $10^{-4}\ (m)$, when considering water as our calibration fluid, the value of the Reynolds number is $Re \approx 10^{-2} \ll 1$. Now, we can write a Stokes equation for a two-dimensional flow:

$$0 = -\overline{\nabla} P\eta + \overline{\nabla}^2 \vec{v}(z) \tag{6}$$

Inside a microfluidic channel of rectangular cross section, the linear displacement of a fluid layer with respect to another in the time interval dt allows obtaining the rate of displacement (or velocity). If we consider a fluid flow moving into the x direction between two plates, the only non-zero velocity component is v_x, which varies in the z direction due to the interaction with the planes, being $\vec{v} = \{v_x(z), 0, 0\}$. The shear produced between the layers depends on the z dimension, and is depicted in Figure 4 :

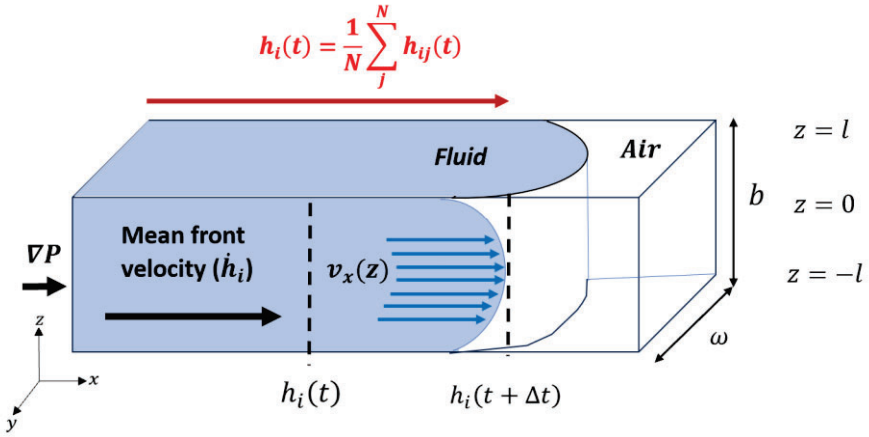

Figure 4. Schematic representation of a fluid interface moving through a microchannel of width ω and height b. Here ∇P is the pressure gradient $v_x(z)$ is the x component of velocity inside the microfluidic channel as a function of height (z); $h(t)$ indicates the mean position of the fluid front. Mean front velocity is $\dot{h}$. The channel dimensions satisfy the relation b/ω ≪ 1.

In equation (7) the shear rate is the rate of change of velocity at which one layer of fluid passes over an adjacent layer [38].

$$\dot{\gamma}(z) = \frac{[dv_x(z)]}{dz} \tag{7}$$

Taking the Stokes equation in the form of equation (6), and considering that $\frac{\partial v}{\partial t} = 0$, we can write:

$$\eta \nabla^2 v = \nabla p_x \tag{8}$$

Now, integrating twice respect to z , being $v(z = \pm l) = 0$ the boundary conditions, we have:

$$\eta \int \frac{\partial^2 v(z)}{\partial z^2} dz = \int \nabla p_x \, dz \tag{9}$$

$$v_z = \frac{1}{2\eta} \nabla p_x \, (z^2 - l^2) \tag{10}$$

Then, we calculate the mean velocity of the interface, through the height b of the microchannel from $z = l$ to $z = -l$.

$$\langle v \rangle = \frac{1}{2\eta} \nabla p_x \, (\langle z^2 \rangle - l^2) \text{ with } \langle z^2 \rangle = \frac{l^2}{3} \tag{11}$$

$$\langle v \rangle = \frac{b^2}{12\eta} \nabla p_x \tag{12}$$

$\nabla P_x = \frac{\Delta P}{h}$ is the pressure gradient, where h is the position of the fluid interface inside the microchannel. Equation (12) can now be written as:

$$\langle v \rangle = \frac{b^2}{12\eta} \frac{\Delta P}{h} \tag{13}$$

This expression can now be used to write an expression to calculate the viscosity of a fluid advancing in the confined space of our microchannel depicted in Figure 4. This new expression is known as the Darcy Law:

$$\eta = \frac{b^2}{12\langle v \rangle} \frac{\Delta P}{h} \tag{14}$$

1.6. Front microrheology for Newtonian and non-Newtonian fluids

Newtonian fluids are characterized by having linear viscosity behavior, independent of the force applied onto the fluid. Water is a Newtonian fluid, its viscosity is linearly related to the shear stress [32]. Newtonian fluids are characterized by having linear viscosity behavior, independent of the force applied onto the fluid. Water is a Newtonian fluid, its viscosity is linearly related to the shear stress [32].

For a steady flow, the viscosity, η of for Newtonian fluids, is constant and depends only on the temperature. The viscosity is then defined as the ratio between the shear stress σ, and the shear rate $\dot{\gamma}$:

$$\eta = \frac{\sigma}{\dot{\gamma}} \tag{15}$$

On the other hand, the viscosity of non-Newtonian fluids is dependent on the shear applied onto them [34]. In some cases, viscosity is a decreasing function of the shear rate, this is called shear thinning behavior. The opposite is known as shear thickening.

The Carreau–Yasuda and power-law models are commonly used to describe viscosity [39]. For this study, we use the power-law, a shear rate dependent model, which calculates viscosity using the parameter *m* and the exponent *n*. Also known as the Oswaldt–De Waele equation [33], the power-law model describes the viscosity of a fluid on dependence of its shear rate as:

$$\eta(\dot{\gamma}) = m\dot{\gamma}^{n-1} \tag{16}$$

where *m* corresponds to the value of viscosity at $\dot{\gamma} = 1$. The exponent *n* indicates the nature of the viscosity of the studied fluid. The latter defines the Newtonian or non-Newtonian nature of the fluid, as follows:

$$\eta(\dot{\gamma}) = \mathrm{m}\dot{\gamma}^{\mathrm{n}-1}, \begin{cases} \mathrm{n} < 1, \ \mathrm{non} - \mathrm{Newtonian, shear\ thinning} \\ \mathrm{n} = 1, \ \mathrm{Newtonian} \\ \mathrm{n} > 1, \ \mathrm{non} - \mathrm{Newtonian, shear\ thickenning} \end{cases}$$

1.7. Rheometry and microrheometry

Since Poiseuille times, efforts have been made to describe the resistance that fluids oppose to flow. For this, methods such as the sphere technique, long parallel tubing, or the use of capillaries have been developed in the early years of rheology [40].

A rheometer is an instrument that measures the stress and deformation history of a material. Viscometers are a specific kind of rheometers that can only measure the steady shear viscosity function of a material [65]. Rheometers may be differentiated on the type of induced flow between drag flows and pressure-driven flows. There are two basic types of rheometers: rotational (shear type) and capillary extrusion. Capillary extrusion is normally used for relatively concentrated suspension/pastes while the rotational design is for relatively less concentrated suspensions [41]. The disadvantages of using this type of equipment include their high operation costs and the large size of samples they require. The initial investment of acquiring such equipment is also high. A viscometer is designed for simple flow measurements on Newtonian materials. A viscometer can also be portable and used for field or remote testing. Rheometers, though more expensive than viscometers, are more versatile and have a much wider dynamic range of control and measurement parameters [41].

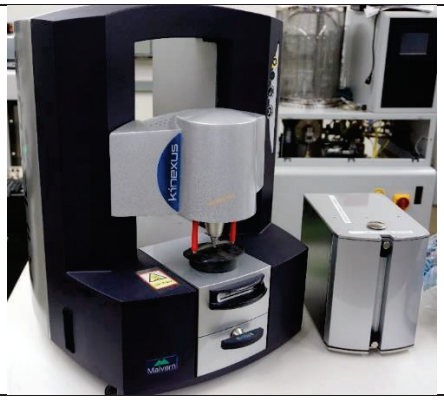

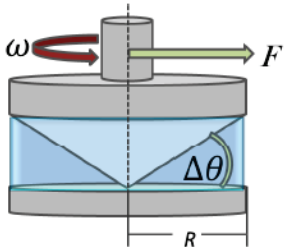

Figure 5. Malvern rheometer from Netzsch is an example of coaxial cone-plate type of rheometer.

The rheological study of biofluids is useful to describe their physiological mechanisms and biological functions. The use of microfluidic techniques has become a widely used method to analyze the viscosity of complex fluids [42]–

[44]. An example is the study of viscosity through shear rheology [45]–[47]. These methods use diverse techniques to generate shear forces inside a fluid. The shear response that is generated is then analyzed and compared to the available rheological mathematical models. However, the development of new materials and the discovery of rheological properties make necessary the formulation of new models capable to describe their viscosity behavior. The interaction of fluid forces and these deformable particles under geometric confinement can produce interesting rheological behaviors that are yet to be fully explored [48]. At the microscale, surface effects and viscosity are the main drivers of fluid behavior, and laminar flows can be observed, which are more predictable [49]

Plasma is also a biological fluid of the Newtonian type, in which viscosity is an important factor influencing whole blood viscosity. Its viscosity value is determined almost entirely by the concentration of high molecular weight proteins [50], [51]. In contrast, non-Newtonian fluids show different nonlinear behaviors that must be defined inside a shear rate window. Due to their complex properties, most biological fluids have non-Newtonian behavior. The viscosity of a Newtonian fluid is independent of the shear rate applied. Blood is a fluid of the shear-thinning type, its viscosity is characterized by a monotonically decreasing dependence on the shear rate [52]. Two types of non-Newtonian fluids are commonly studied: shear thinning and shear thickening. A shear thinning fluid, such as blood, presents a high viscosity at low shear rates, while at high shear values the opposition to flow decreases.

Complex fluids are mixtures that have a coexistence between two or more phases [34], [53], [54]. The rheometric properties of complex fluids have been traditionally studied using macroscopic devices. The disadvantages present in this type of equipment include their inability to perform tests in real time, and the large size of samples they require. Because of that, many proposals have been made towards miniaturization, to carry the advantages of microfluidics into the field of rheometric analysis.

Understanding the rheology of complex fluids at these small length scales is not only fundamentally rich but also important for a wide range of applications including porous media flows and blood flow in capillaries. The ability to precisely control the flow geometry has led to devices that can measure shear and

extensional fluid rheology. In particular, the simplicity and rapid prototyping offered by methods such as polydimethylsiloxane (PDMS)-based soft lithography has allowed the widespread adoption of microfluidic devices for probing complex fluids and their rheology at a wide range of length scales [55] [56].

Many state-of-the-art microrheometers are limited to Newtonian fluids, such as plasma. Nevertheless, emerging techniques are being proposed for the analysis of complex fluids [57], [58]. These types of novel devices, however, are complex to manipulate and require time and experienced personnel. To address this and the problems related to the traditional laboratory rheometers, we designed a microrheometer composed of a microfluidic device, that uses electronic detection of the fluid front advancement. The focus of the project is the analysis of blood components affecting viscosity and, of course, diseases that affect the red blood cell wall elasticity and red blood cell count. The patented technology consists of a method, apparatus, and micro-rheometer for measuring rheological properties of Newtonian and non-Newtonian fluids [66]. The microrheometer comprises a microchannel with an inlet and an outlet; and a sensor array arranged along the microchannel to measure rheological properties of a fluid. The sensor array comprises a plurality of pairs of electrodes, the two electrodes of each pair of electrodes being placed face to face within the microchannel to function as an electronic switch when the fluid flows through them. The micro-rheometer is intended to be the basis for a small portable device useful for medical diagnosis in diseases associated to changes in blood viscosity, operating in a wide range of shear rates.

1.8. Hemorheology and red blood cell membrane deformability

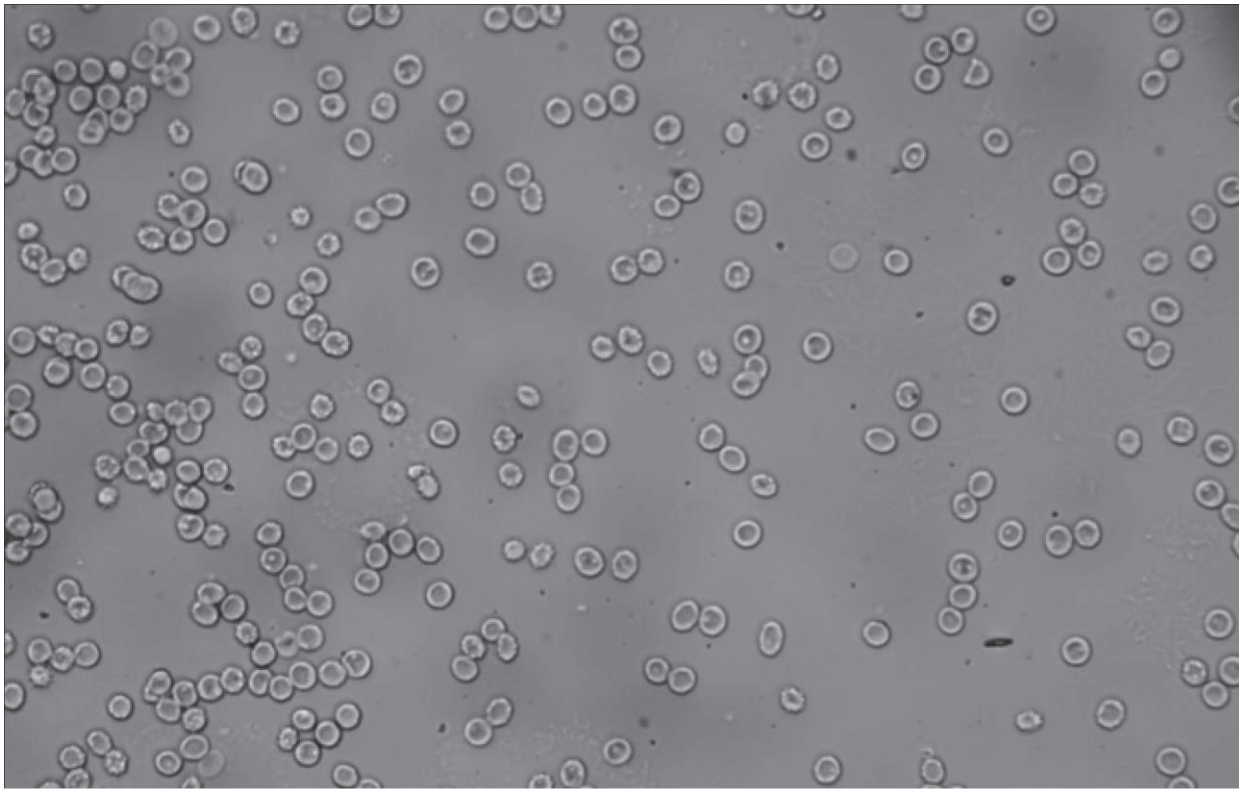

Figure 6. Red blood cells from a 28% ht blood sample from a healthy donor observed using a 40X objective.

The presence of solid or semi-solids in suspension can alter the viscosity behavior of a fluid. Such is the case of blood, which presents non-Newtonian behavior of the shear-thinning type. This means that its viscosity decreases as the shear applied increases [59]. Blood is a two-phase suspension of formed elements, such as red blood cells (RBCs), white blood cells (WBCs), and platelets, suspended in an aqueous solution of organic molecules, proteins, and salts called plasma [60]. Blood viscosity is determined by hematocrit, plasma viscosity, RBC aggregation, and the mechanical properties of RBCs. RBCs are highly deformable, and this physical property significantly contributes to aiding blood flow both under bulk flow conditions and in the microcirculation [61]. The tendency of RBCs to undergo reversible aggregation is an important determinant of apparent viscosity because the size of RBC aggregates is inversely proportional to the magnitude of shear

forces; the aggregates are dispersed with increasing shear forces, then reform under low-flow or static conditions. RBC aggregation also affects the in vivo fluidity of blood, especially in the low-shear regions of the circulatory system.

Hemorheology studies the flow and deformation behavior of blood and its formed elements[62]. Blood viscosity, which is highly affected by factors such as plasma [51], hematocrit, deformability, and aggregation, are considered promising parameters for effectively monitoring variations in physiological and pathological conditions [52]. The normal hematocrit level for men ranges from 40 to 50%, while in women differs between 36 to 46% [60]. Leukocytes and thrombocytes only comprise near the 1% of the cellular content in blood [63]. For this reason, blood rheology focuses on the physical properties and deformability of the red blood cell (RBC). Healthy erythrocytes have a characteristic shape of a biconcave disc. They have no nucleus and have a distinctive elasticity that allows them to go through small capillaries. They have a diameter of 7.8 µm and a height of 2.5 µm at their highest point. The central valley has a thickness of approximately 1 µm [64]. This shape has an important biological function, since is facilitates the exchange of substances through the membrane, while at the same time allows the RBC to travel through slits as small as 2 µm [65]. Some important properties of the RBC are related to their aging and aggregation processes. They present a tendency to form cell column shaped aggregates known as *rouleaux* [61]. They can reversibly and continuously disaggregate to single flowing discocytes for increasing shear rates (See Figure 7). Another important characteristic is that they contain a concentration hemoglobin solution which affects the speed at which they deform [14]. This phenomenon can be observed as blood is exerted at different pressures through capillaries.

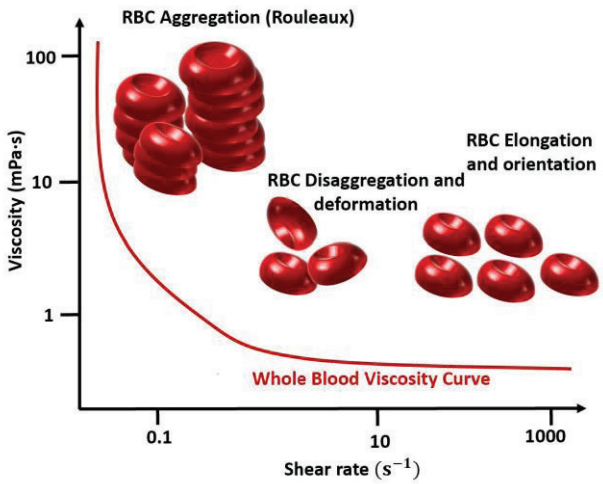

Figure 7. Red blood cell aggregation and disaggregation [50].

We obtained photos of *rouleaux* formation after conducting day by day observation of healthy blood samples (Figure 8).

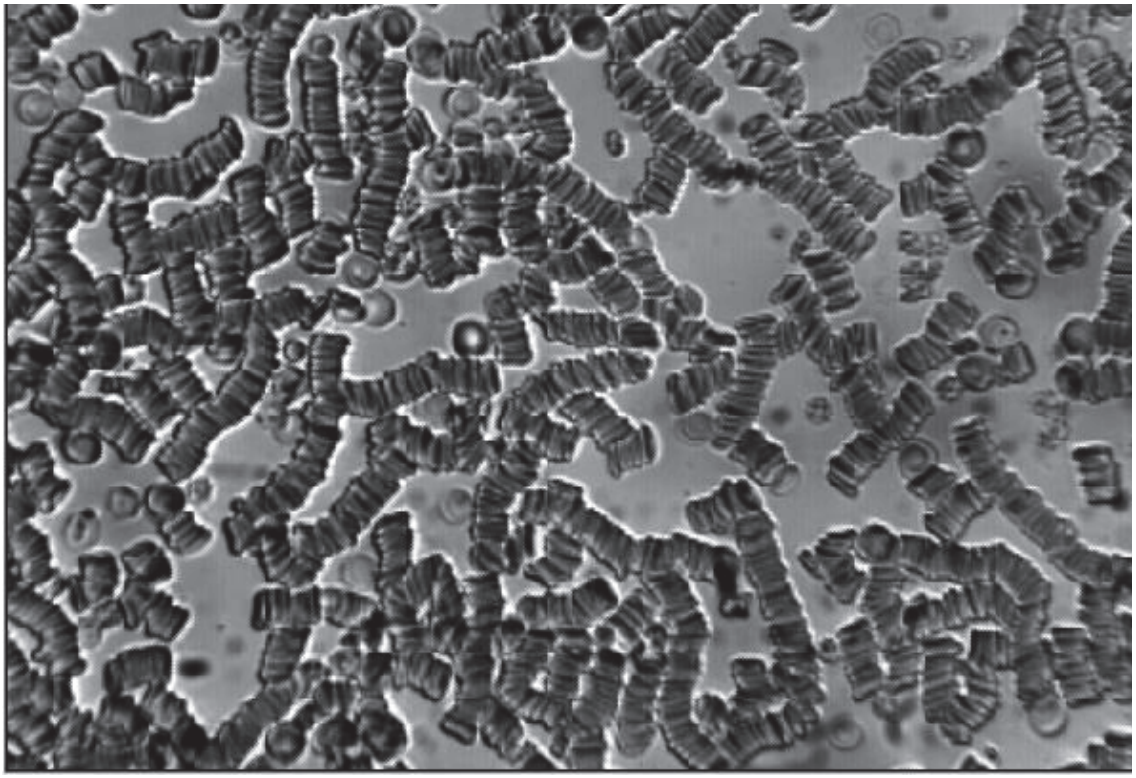

Figure 8. *Rouleaux* from a 38% hematocrit sample from a healthy donor, using an inverted microscope Optika XDS-3 and a 50X objective (Méndez-Mora).

Blood rheology is highly affected by alterations of hematocrit and RBC deformability. RBC deformability change is often the result of alterations in the

properties of the membrane skeletal proteins, the ratio of RBC membrane surface area to cell volume, cell morphology, and cytoplasmic viscosity. This could be caused by genetic disorders such as beta or alpha thalassemia. Another important factor, RBC aggregation, is mainly determined by plasma protein composition and surface properties of RBCs, with increased plasma concentrations of acute phase reactants in inflammatory disorders a common cause of increased RBC aggregation [66]. Fibrinogen and coagulation factors in plasma also play an important role in blood viscosity [51].

The shear rate is directly related to the velocity at which the fluid is exerted by the pressure applied. The low shear region is described as the phase of low velocities where blood cells are aggregated and oppose the highest resistance to flow. As the pressure applied rises, the RBCs disaggregate and start to deform [67]. At the highest shear rates, the blood cells adopt certain alignment to allow an efficient flow through the small structures of the blood vessels [68]. Viscosity decrease with shear rate is intimately related to the dynamics and interactions of red blood cells (RBCs), the main cellular component of whole blood. When RBCs circulate through the vascular system, deformability, and dynamics of RBCs account for a further decrease in blood viscosity. Blood viscosity strongly depends on other parameters such as temperature, hematocrit and hemoglobin content [69], [70].

PART II

Materials and methods

2. Fabrication of microfluidic channels

The design and experimentation using micro-nanoscale devices and systems has been one of the most important trends in many areas of biomedical research over the past decades [17]. One of the main purposes of building smaller instruments and more compact analytical systems is their ability to offer high-precision assessment of micro and nanometric biological components, as well as to facilitate the obtention of results in a high-throughput fashion, as well as to reduce consumption of expensive reagents [71]. Micro-nanofabrication technology has played a central role in such an implementation. Using the established micro-nanofabrication techniques, microchips for various biological and clinical applications have been successfully fabricated in recent years. One major advantage of using the conventional clean room-based fabrication technology is the capacity to directly integrate lab-on-a-chip devices with powerful electronic processing units, which eliminates large electrical wiring and reducing overall system dimensions [72].

However, there still exist constraints yet to be addressed. These include the limited access to clean room facilities, incompatible chemical and thermal treatments, complicated and inflexible process flows, and restricted material selection options, in addition to high-maintenance and operation costs of fabrication equipment [73].

The fabrication technique used to produce the devices for this thesis is soft lithography. Soft lithography refers to a collection of techniques that enable the fabrication of structures or the transfer of materials using elastomeric soft masters (e.g., stamps, casts, and photomasks)[74]. In this thesis, the elastomeric material used is polydimethylsiloxane (PDMS)[8], [17]. PDMS is a clear, non-cytotoxic elastomer that cures at room temperature when mixed with a curing agent. By pouring it on a rigid cast, it would create a negative stamp that is flexible, optically transparent, and easy to cut and handle.

The casts are fabricated using photolithography, also called optical lithography or UV lithography. This is a process used in microfabrication to pattern parts on a thin film or the bulk of a substrate, also called a wafer. It uses light to transfer a geometric pattern from a photomask to a photosensitive or light-sensitive chemical photoresist on the substrate. A series of chemical

treatments then either etches the exposure pattern into the material or enables deposition of a new material in the desired pattern upon the material underneath the photoresist. The relation between the lithography process for the cast fabrication and the soft lithography for the PDMS channel formation is presented in the diagram on Figure 9.

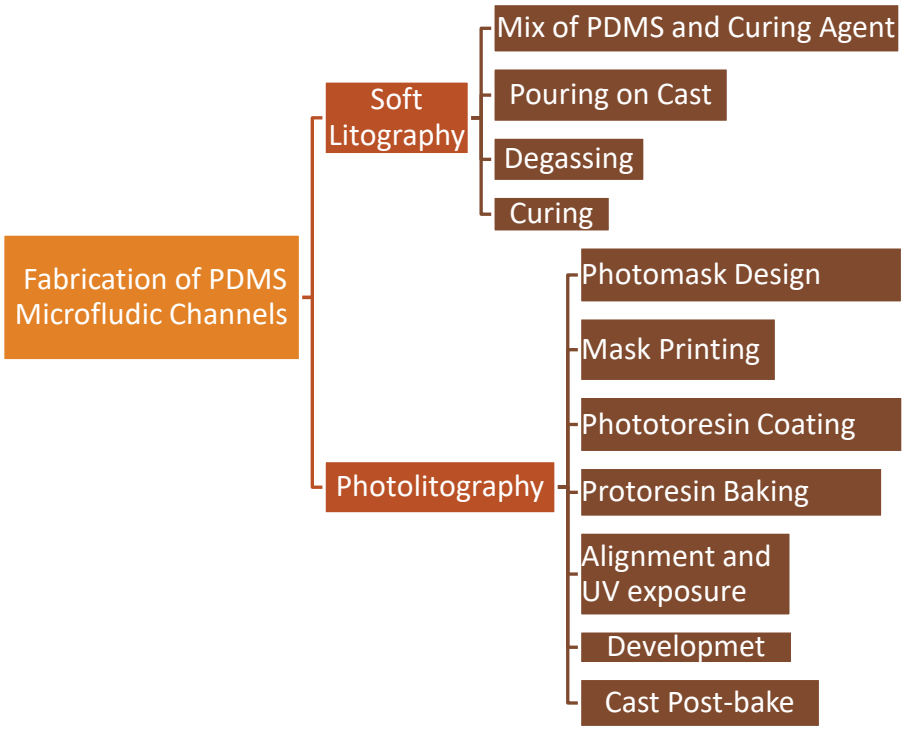

Figure 9. Diagram of the fabrication process of PDMS microfluidic channels.

Photolithography shares some fundamental principles with photography in that the pattern in the photoresist etching is created by exposing it to light, either directly (without using a mask) or with a projected image using a photomask. This procedure is comparable to a high precision version of the method used to make printed circuit boards. Subsequent stages in the process have more in common with etching than with lithographic printing. This method can create extremely small patterns, down to a few tens of nanometers in size. It provides precise control of the shape and size of the objects it creates and can create patterns over an entire surface cost-effectively. Its main disadvantages are that it requires a flat substrate to start with, it is not very effective at creating shapes that are not flat, and it can require extremely clean operating conditions. Photolithography is the standard method of printed circuit board (PCB)

and microprocessor fabrication. Directed self-assembly is being evaluated as an alternative to photolithography [19].

Photolithography is also commonly used to produce computer chips. When producing computer chips, the substrate material is a resist covered wafer of silicon. This process allows hundreds of chips to be simultaneously built on a single silicon wafer. In microfluidics, however, is a popular technique for the fabrication of casts and microelectrodes integrated into microfluidic devices.

2.1. Design of photomasks

To imprint the desired structures into the PDMS material, a cast must be created. For this, the selected photoresist needs to be irradiated with light on certain areas. For that purpose, masks to avoid or permit the exposure of these areas must be designed [75].

Most micro and nano technologies require different types of patterning processes at certain stages during design and production cycles. There are various methods of patterning, of which the application of photo masks is the most common one. Therefore, the definition of such masks is a critical step during micro product development [71]. The mask used are designed using CleWin 5 software, which is a hierarchical layout editor. Typical layouts designed using this software consist of symbols, also known as cells, which may be nested, and can be directly accessed by using the hierarchical tree-view of the design. Editing a symbol in one location will change several other instances of the same symbol. The basic drawing primitives are boxes, circles, wires, and polygons, which can be stored in standard CIF format. Rings and spirals are automatically generated as wires. Options of including text elements can be realized as polygons [76]. In Figure 10, the mask design for electrodes and microfluidic channels is shown. The design is then printed on acrylic base, which is a flexible sheet of thin material, that permits the fabrication of low resolution and low complexity designs. When better resolution is required, a chrome photomask is preferred. The latter can achieve a 1,5-2 µm resolution [77]. Chrome is well-established as the standard absorber for photomasks due to its opacity, durability, and adhesion properties [75], [78]. For this reason, a chrome mask is used to print the masks in Figure 10.

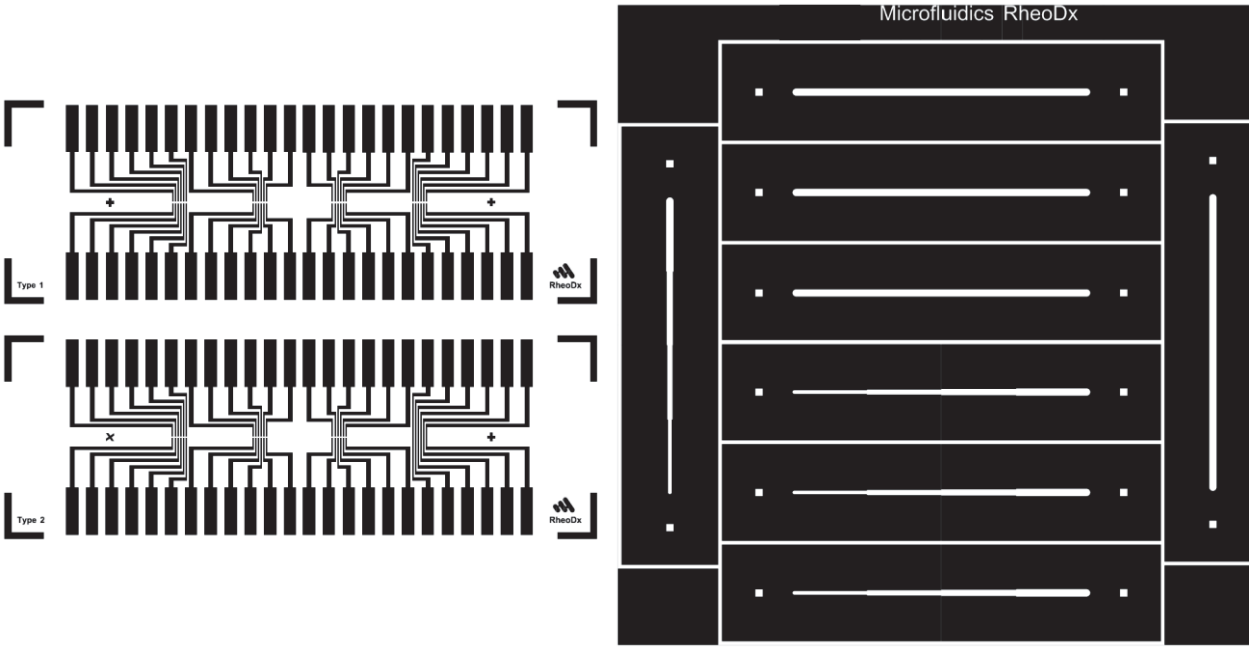

(a) **(b)**

Figure 10. Mask design for (b) microelectrodes and (b) microfluidic channels (Méndez-Mora).

The dark areas represent the parts on which the UV light will not impact the photoresist. This depends on the type of light-sensitive resin that is chosen for the cast. In this case, the photoresist of choice is SU-8, a negative photoresist [79]. The SU-8 is a negative, epoxy-type, near-UV photoresist based on EPON SU-8 epoxy resin that has been originally developed, and patented (US Patent No. 4882245 (1989) and others) by IBM [22]. This photoresist can be as thick as 2 mm and aspect ratio >20 and higher have been demonstrated with a standard contact lithography equipment [23], [24], [80].

As depicted in Figure 11, the mask includes two types of microfluidic channel design a) channels of constant width $(\omega) = 1000\ \mu m$ and length of 4 m and b) channels with four different widths $(\omega_1 = 1000\ \mu m,\ \omega_2 = 800\ \mu m,\ \omega_3 = 700\ \mu m,\ \omega_4 = 500\ \mu m)$.

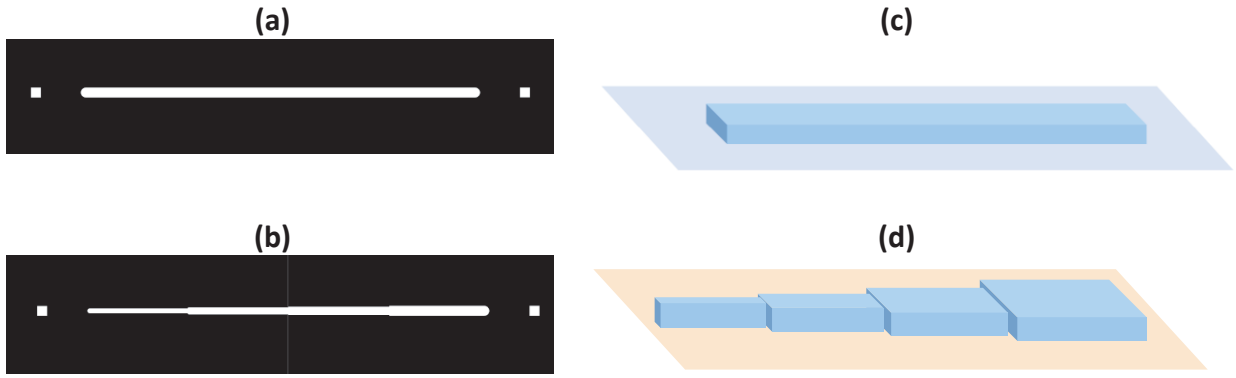

Figure 11. Photomask for microfluidic channel of (a). constant width and (b). multiwidth. Resulting PDMS microfluidic channel of (c). constant and (d) multiwidth channel.

2.2. Fabrication of casts for microfluidic channels

The first step is the preparation of the surfaces where the photoresist is to be deposited. This comprises a cleaning and drying process to ensure that the glass substrates are absent of particles that may interfere with the SU8-50 resin adhesion. Substrates are chemically cleaned to remove particulate matter on the surface as well as any traces of organic, ionic, and metallic impurities. Glass substrates are submerged in an acetone bath, and then placed inside the ultrasonic cleaner for 10 minutes. A second bath is performed, like the previous, using isopropanol as solvent. Using the tweezers, the substrates are removed from the isopropanol bath. Liquid excess is removed using compressed nitrogen. To ensure dehydration of the surface, glass substrates are placed on a hotplate at 95°C for at least 10 minutes. A brief description of the process is depicted in Figure 6.

In contact printing, the resist-coated substrate is brought into physical contact with the photomask. The wafer is held on a vacuum chuck, and the whole assembly rises until the wafer and mask contact each other. The photoresist is exposed to UV light while the wafer is in contact position with the mask. Because of the contact between the resist and mask, very high resolution is possible in contact printing (e.g. 1µm features in 0.5µm of positive resist). The problem with contact printing is that debris, trapped between the resist and the mask, can damage the mask and cause defects in the pattern. The process is depicted in Figure 12.

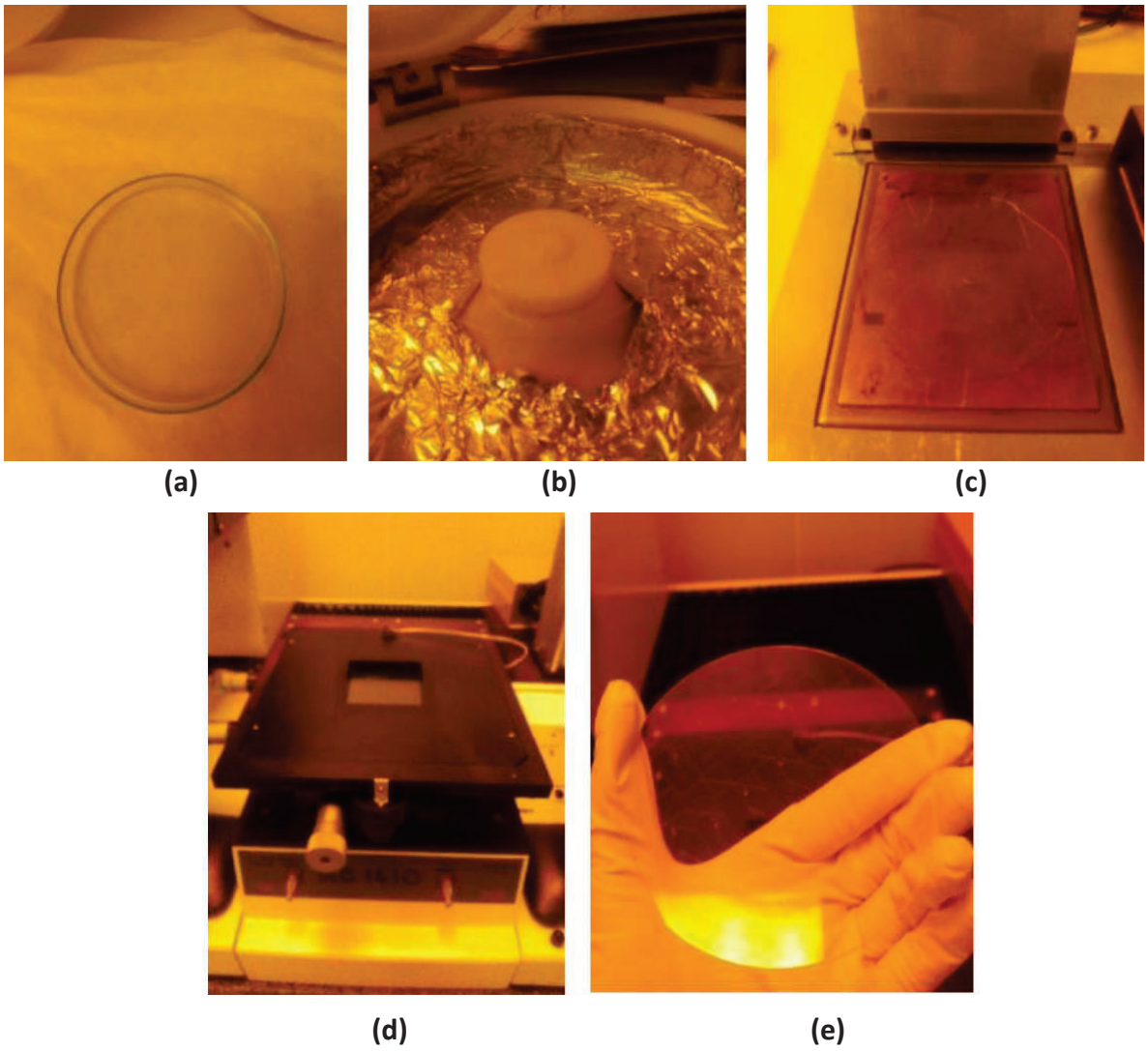

Figure 12. Once the wafer is cleaned (a), the SU-8 resin is spin coated onto the substrate (b), then it is soft baked on a hot plate (c). Exposition is made on a UV aligner (d) and last bake is done, again on the hot plate in (c). The result is a wafer with the mask motives printed on SU8-50 ready to be develop (e).

After the casts are formed, measurements can be made to ensure that the height and quality of the structure is adequate. For this, a confocal microscope or a profilometer can be used. It is important to conduct these measurements in a controlled clean room environment, to avoid dust, hair, and other particles attaching to our newly formed casts. After this, the deposit of flexible PDMS can be made for the fabrication of channels.

2.3. Fabrication of gold microelectrodes

For the fabrication of microelectrodes, the glass surface used is coated with photoresist AZ 5214 (AZ E. Materials, Japan [81]). Figure 13 shows the fabrication procedure of the parallel-plate gold electrodes. As shown in Figure 13 (a) the pattern of the electrodes is obtained by exposing the photoresist under UV light (Figure 13 (b)). Developer AZ 300 MIF is used to wash off the pattern on the glass surface (see Figure 13 (c)). Later, Au is sputtered onto the patterned glass surface for four minutes (see Figure 13(d))). Finally, using an ultrasonic cleaner, AZ 5214 is removed (see Figure 13 (e)), leaving the remaining Au electrodes on the glass surface (see Figure 13 (f)).

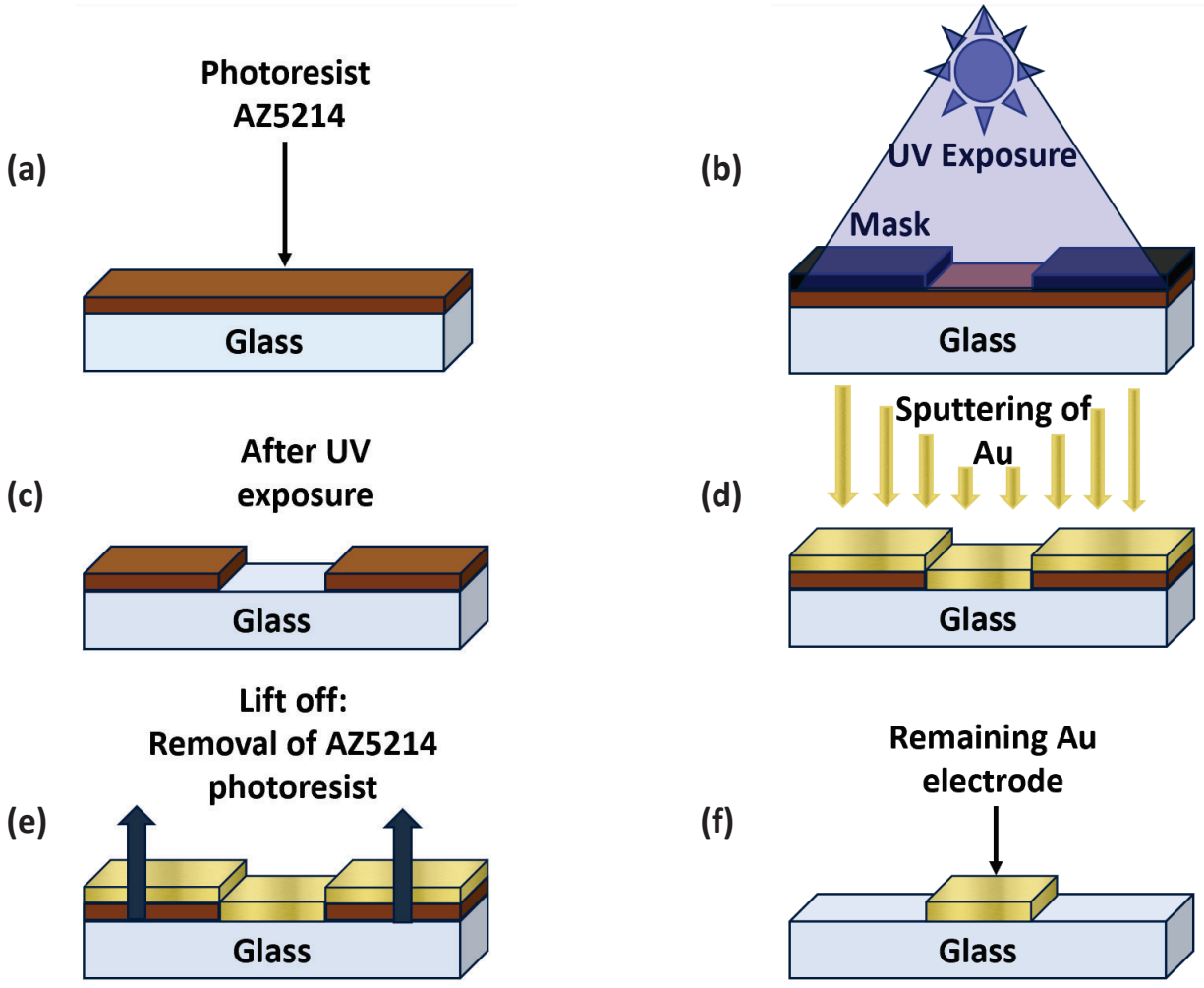

Figure 13. Photolithography process for the fabrication of parallel-plate gold electrodes

2.4. Assemblage of PMDS channels

For this PDMS the ratio used between the curing agent and the PDMS is one part of curing to 10 parts of PDMS (1:10). For specific applications the ratio can be changed to have a PDMS softer or harder. To prepare the mix it is necessary weight the PDMS, then add the curing agent and mix them thoroughly. It is important that the PDMS is poured first and then the curing agent, doing the opposite may lead to a bad cross linkage of the polymer. Next step is degassing to removing bubbles. The preparation is filled with bubbles from the mixing. These need to be removed from the resin to avoid discontinuities inside the microfluidic channels and the cured PDMS. A vacuum pump was used to achieve zero bubbles. The preparation is placed in a vacuum for at least one hour.

SU8-50 casts are positioned in a petri dish. Once the preparation is free of bubbles, it is carefully poured on the casts. The resin cross linkage will take up to 24 hours to conclude. Using the scalpel, the PDMS is easily peeled off the petri dish and the casts, as seen in Figure 14. The different chips are cut and pierced using the scalpel and the punch. Punch holes are made from behind the channels formed on the cured PDMS, observing that these penetrate enough to reach the opposite side of the material. The PDMS remains inside the newly formed holes are then removed using tweezers.

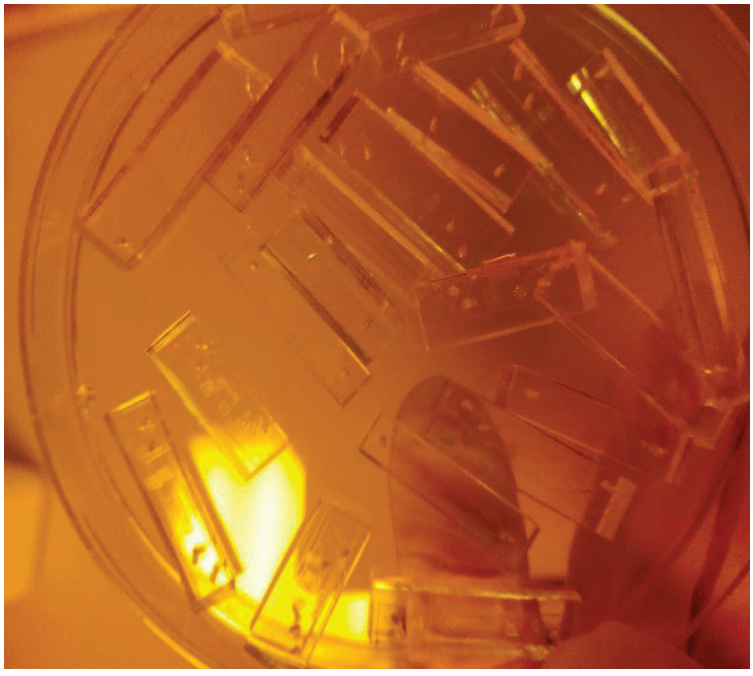

Figure 14. PDMS channels peeled off the casts and ready to be attached on glass.

Once the chips are already separated and punched, they are properly cleaned and dried using isopropanol and compressed nitrogen. Each individual chip and its glass substrate are placed inside the plasma cleaner, with both the surfaces bonded facing each other. The surfaces are treated as follows: Vacuum is activated (>1 minutes), air entrance in open for 30 seconds, High plasma is switched ON. When the blue/violet mist appears inside the plasma chamber, one minute of treatment is performed. The vacuum system and plasma are switched OFF. The chamber door is opened carefully. When the plasma cleaning is complete, the two pieces are taken out and then finally aligned and pressed together. The resulting piece is a microfluidic channel with electrodes, Figure 15.

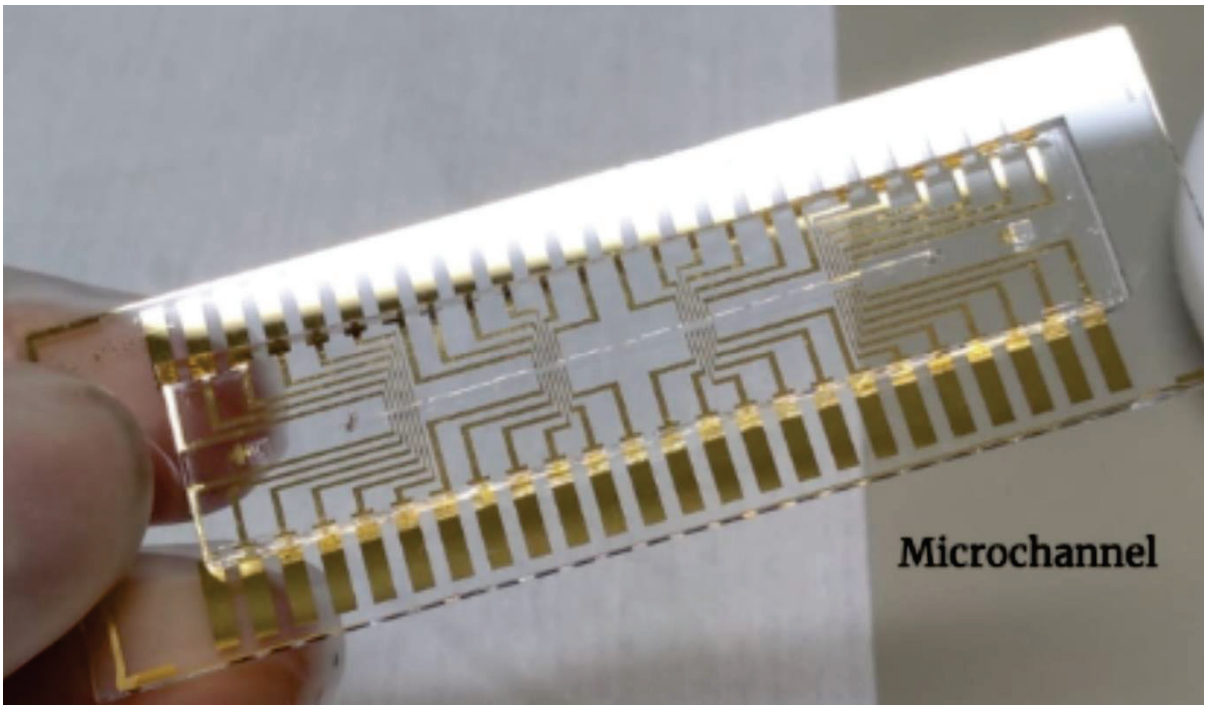

Figure 15. Microfluidic channel made of PDMS assembled on a glass substrate with gold electrodes.

3. Experimental setup

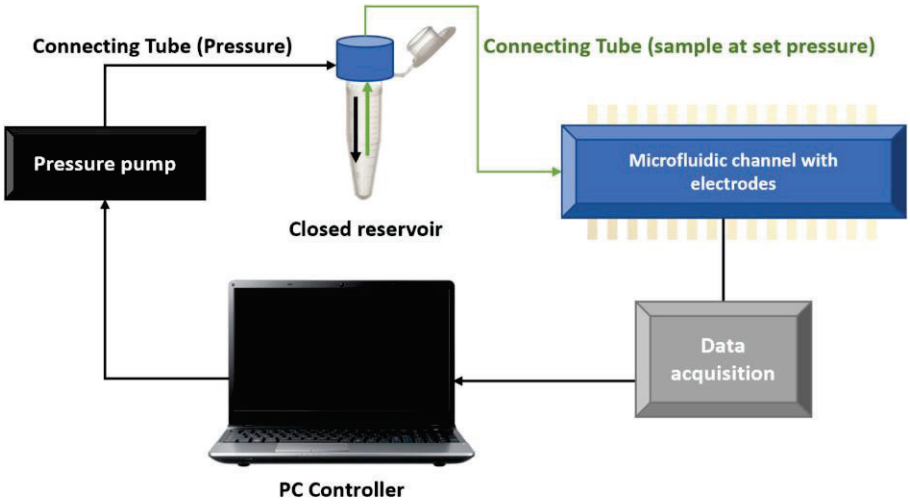

Figure 16. Diagram of the experimental setup used for the microrheometer.

The experimental setup is composed of a pump (Dolomite Fluika) as a pressure source connected to a closed fluid reservoir. We use tubing to connect the microchannel to the sample container. Each electrode is connected via a pin array box to an acquisition control card. As soon as the pressure starts being applied, electronic reading is activated thanks to the controller of a myRIO National Instruments card. The sample fluid comes out from the reservoir at the set pressure and goes directly into the channel. As the fluid goes into contact with the electrodes, the time required for the fluid front to reach each electrode pair inside the microfluidic channel is obtained. The Cole Parmer Tygon tubing used for connections, is biocompatible, flexible and easy to work with. The tubing connecting transporting the sample from the reservoir to the microfluidic channel has internal radius $r_t = 127\ \mu m$ and length $l_t = 20\ cm$.A diagram is shown in Figure 16. In Figure 17, an image of the laboratory arrangement is presented.

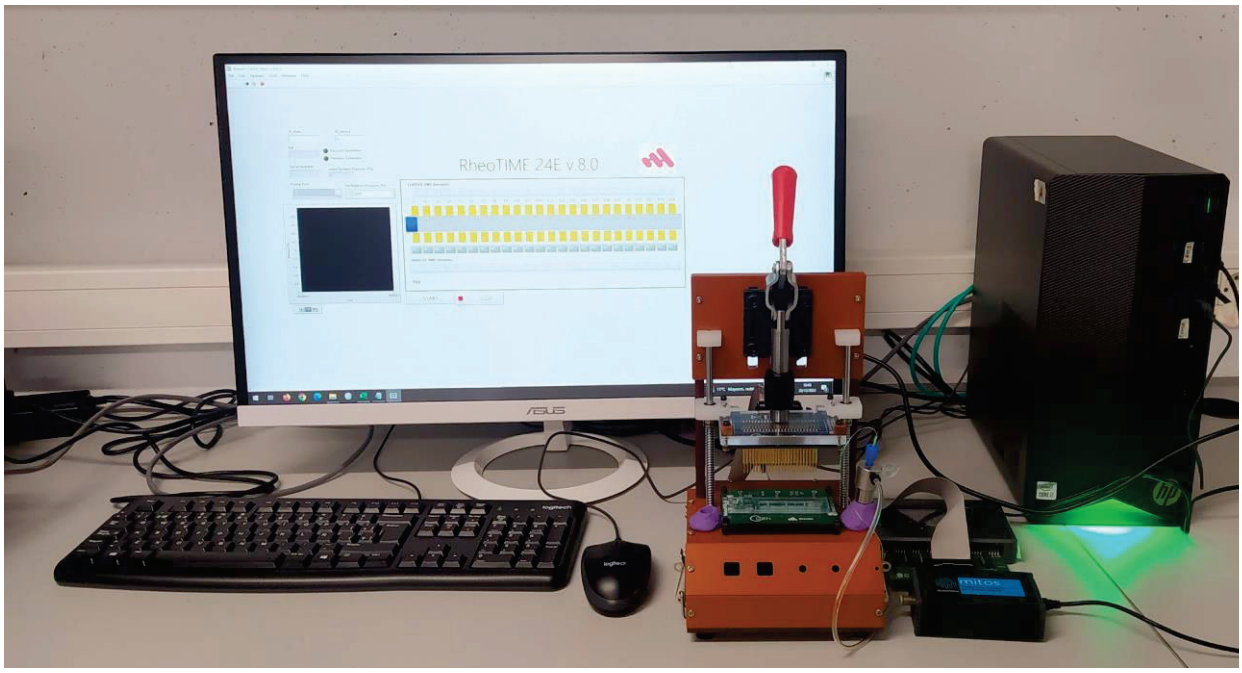

Figure 17. Laboratory setup used for the experiments.

The experiments are performed using microfluidic chips made of polydimethylsiloxane (PDMS) attached to glass substrates of $2.6\ x\ 7.6\ cm^2$ by using plasma bonding. The glass substrates have a printed pattern of 24 pairs of gold electrodes, which were in contact with the flowing fluid. The electrodes have a 350 μm separation in between and are placed in the form of four groups of six pairs located along the length of the channel. The distance between each set is $8.5\ mm$. The channel height for all channels is $b = 300 \mu m$, and the length from inlet to outlet is $l_c = 4\ mm$. (See Figure 18).

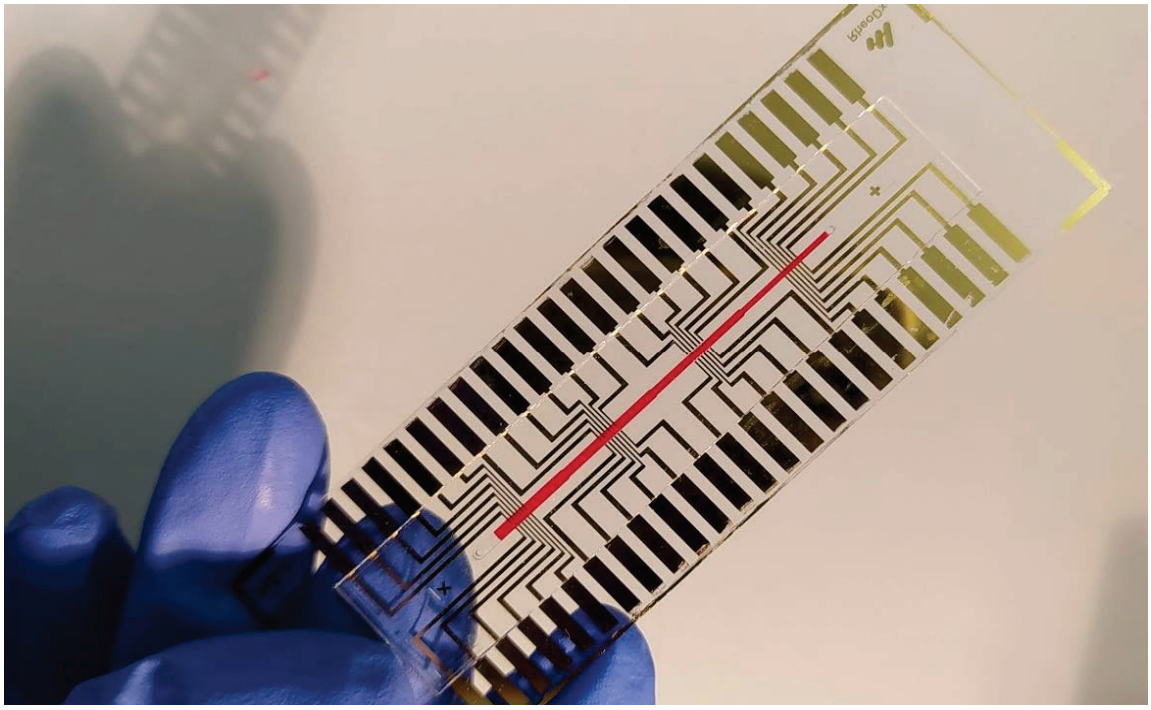

Figure 18. Blood sample inside a PDMS microfluidic channel with gold electrodes after one experiment.

4. Results and discussion

4.5. Rheological characterization of blood through electronic fluid front shear rate.

4.5.1. General case: model for non-Newtonian fluids

To perform experiments on the rheological properties of blood, we start by preparing blood samples at known hematocrits. Healthy blood is obtained from Banc de Sang i Teixits. Tubes, as the ones shown in Figure 19, are extracted from different donors two days before the experiment.

Figure 19. Tubes of 10 mL of whole healthy human blood obtained from Banc de Sang I Teixits.

By employing a centrifuge RBCs are separated from plasma. After a first centrifugation, we can separate whole plasma from red cells. The resulting plasma can also be then further separated into two aliquots: Plasma which is contained in the supernatant and Platelet Rich Plasma (PRP), contained in buff-coat area between plasma and RBCs (see Figure 20).

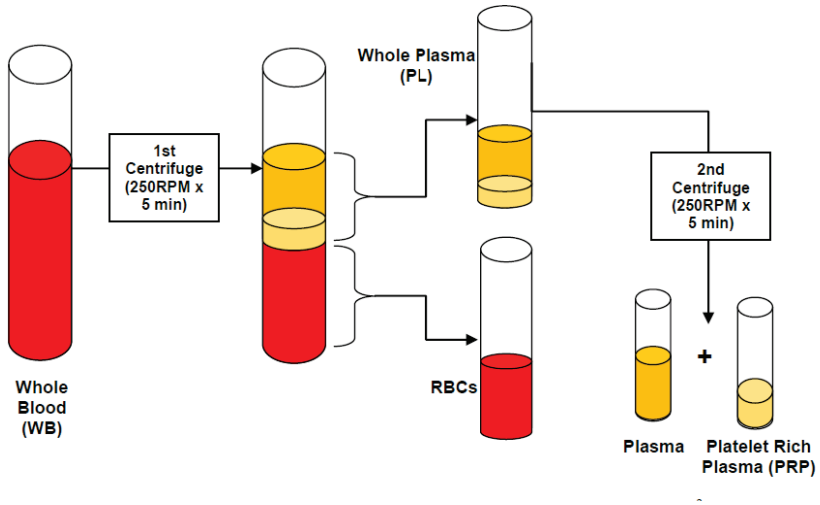

Figure 20. Plasma separation process from whole blood. Adapted from F. Liu [82]**.**

By using the experimental setup described in Figure 21, the fluid front advances through the microfluidic channel (Figure 22).

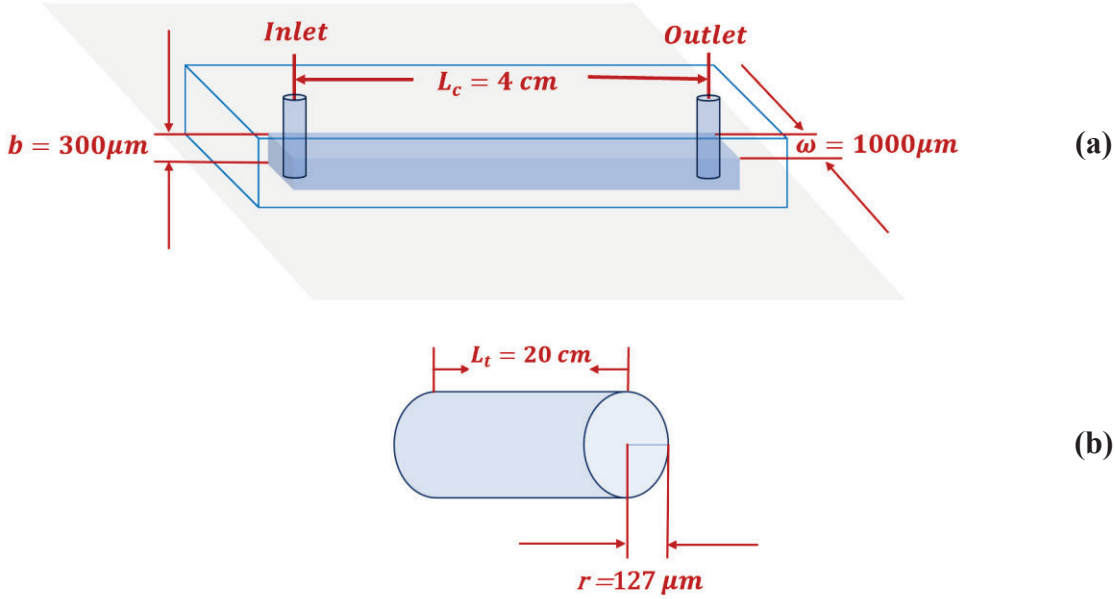

Figure 21. Dimensions of the (a) microfluidic channel and (b) the tubing used in the experiments.

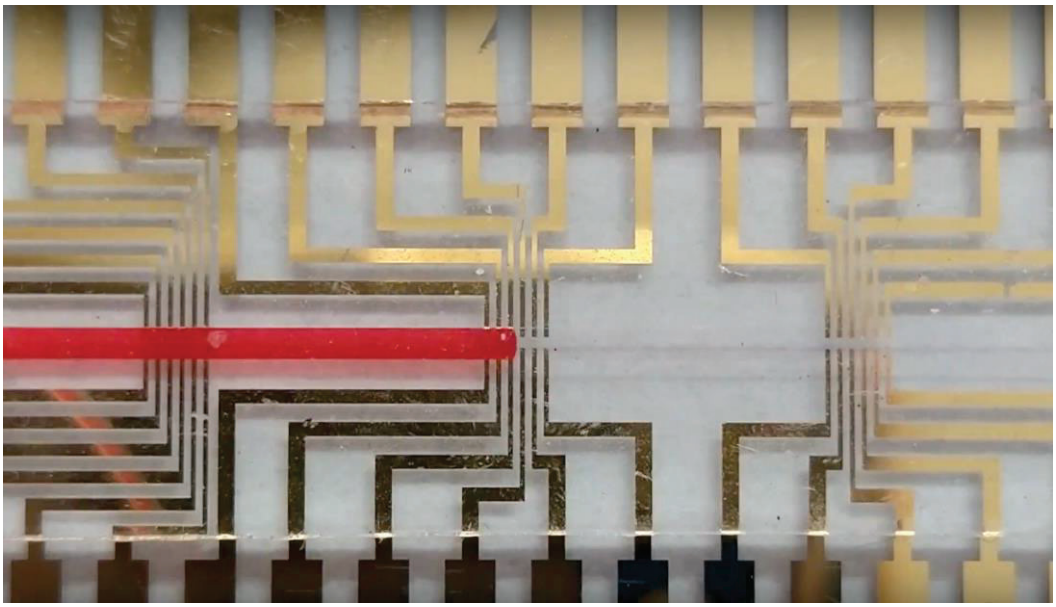

Figure 22. Detail of the fluid front from a blood sample advancing through the microfluidic channel.

Then, we obtain time readings for the fluid advancement on the computer terminal, using the custom-made software RheoTIME (Figure 23).

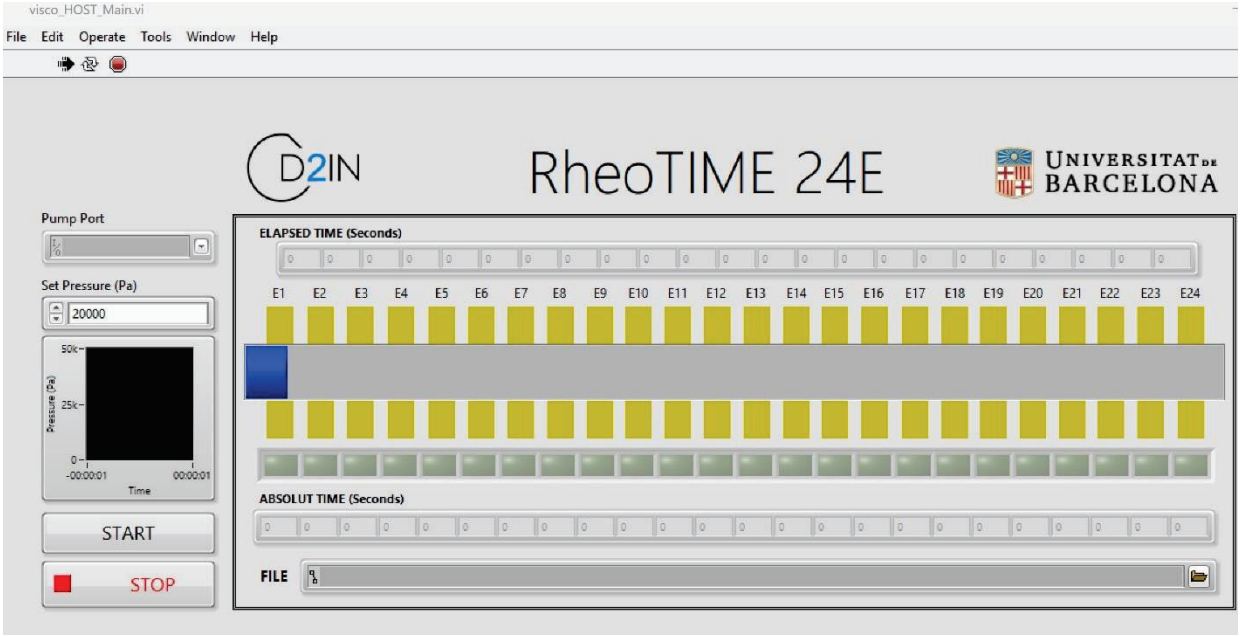

Figure 23. Screenshot of the software used for the fluid advancement detection.

By obtaining the fluid/air interface advancement, the shear rate $(\dot{\gamma})$ can be calculated as the normalization of the mean front velocity $\dot{h}(t)$ according to the microchannel height, b as defined by Eq. (17)

$$\dot{\gamma} = \frac{\dot{h}}{b} \tag{17}$$

Using the Stokes equation, it is possible to calculate the flow through a known geometry as a function of the average velocity. In most cases, microfluidic systems are composed of pressure sources and microfluidic channels connected by cylindrical tubing, creating coupled fluidic systems. The flows passing through two coupled geometries are equivalent due to the mass conservation principle. The mathematical deductions concerning these calculations are detailed in Appendix A.1 from Méndez-Mora *et al.* [38].

In a closed system composed of a pressure source, a fluid reservoir, and the coupling of tubing with a microchannel of rectangular cross-section, the pressure inside the rectangular microchannel, ΔP is the summation of all the pressures in the system.

As it is explained in appendix A.2 from Méndez-Mora et al. [38], the effective pressure (P_{eff}) is the pressure resulting from the combination of the pumping system pressure, the capillary pressure, and the hydrostatic pressure into the whole system (see Eq. (A.25) deduced in Appendix A.2 [38]). Effective pressure P_{eff} has an algebraic dependence with $\dot{\gamma}$, as shown in Eq. (18):

$$P_{eff} = K(m,n)\dot{\gamma}^{n} \tag{18}$$

By plotting the effective pressure against the shear rate calculated using Eq. ((17), we obtain the fit shown in Figure 24.

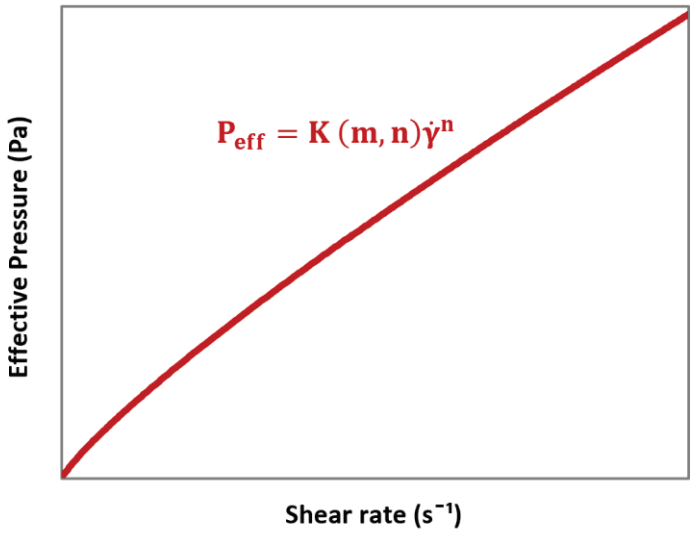

Figure 24. Effective pressure vs. shear rate of whole blood, a non-Newtonian fluid of the shear thinning type.

Here, all the independent variables are grouped in K, which depends on the fluid properties (m and n) and the geometrical parameters of the system shown in Eq. (19):

$$K(m,n) = m2l_t\left(\frac{\omega b^2}{\pi r^2}\right)^n\left(\frac{1}{r^{1+n}}\right)\left(\frac{1}{n}+3\right)^n \qquad (19)$$

Where the connecting tubing of length, is l_t, and internal radius, r_t, is inserted into a microfluidic channel of width, ω and height, b. Once m and n are obtained, we can calculate viscosity of a fluid on dependence of its shear rate, using the Power-law model in Eq. (20):

$$\eta(\dot{\gamma}) = m\,\dot{\gamma}^{\,n-1} \qquad (20)$$

where the pre-factor m corresponds to the value of viscosity at $\dot{\gamma} = 1$. The exponent n indicates the nature of the viscosity of the studied fluid. Depending on the value of n, the behavior of a fluid is characterized as Newtonian or Non-Newtonian. Values of $n < 1$, correspond to shear thinning behavior, while $n > 1$ corresponds to shear thickening behavior. On the other hand, Newtonian fluids have a value of n=1. Now, we can obtain a viscosity curve like the one shown in Figure 25.

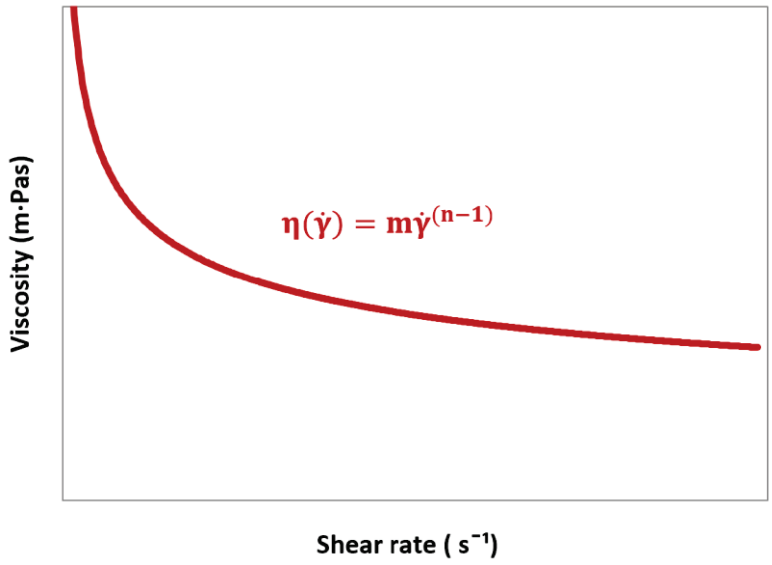

Figure 25. Viscosity vs. shear rate of whole blood, a non-Newtonian fluid of the shear thinning type.

4.5.2. Newtonian fluids

Newtonian fluids have a constant viscosity, which does not depend on the applied pressure. Analogously as it has been done in the general case, the mathematical model for Newtonian fluids $(\mathrm{n} = 1)$ has been developed in Appendix A.3 [38].

Pressure for the entire system is described in Eq. (7), which has a linear dependence on the mean front velocity.

$$P_{eff} = K(m, n = 1)\dot{\gamma}^{n} \tag{21}$$

For the Newtonian case K can also be expressed in terms of the geometry of the system and the experimentally obtained front velocity:

$$K(m, n = 1) = m\frac{8\omega b^2 l_t}{\pi r^4} \tag{22}$$

The experimental data of the shear rate values obtained from applying a known pressure to a Newtonian fluid have the linear relation shown in Eq. (9):

$$P_{eff} = A\dot{\gamma} \tag{23}$$

When we plot the effective pressure against the shear rate calculated using Eq. (23), we obtain the fit in Figure 27.

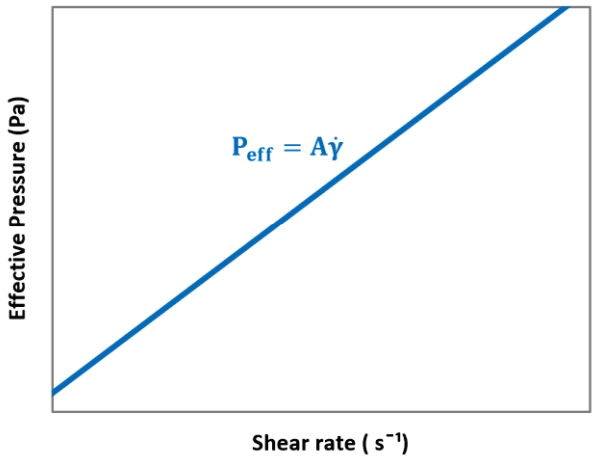

Figure 26. Effective pressure vs. shear rate of a Newtonian fluid.

We calculate m using:

$$m(n = 1) = \frac{A}{\frac{8\omega b^2 l_t}{\pi r^4}} \tag{24}$$

Now, we rewrite Eq. (20) as:

$$\eta = m \tag{25}$$

And now we can obtain the plot for the viscosity of a Newtonian fluid, like the one shown in Figure 27.

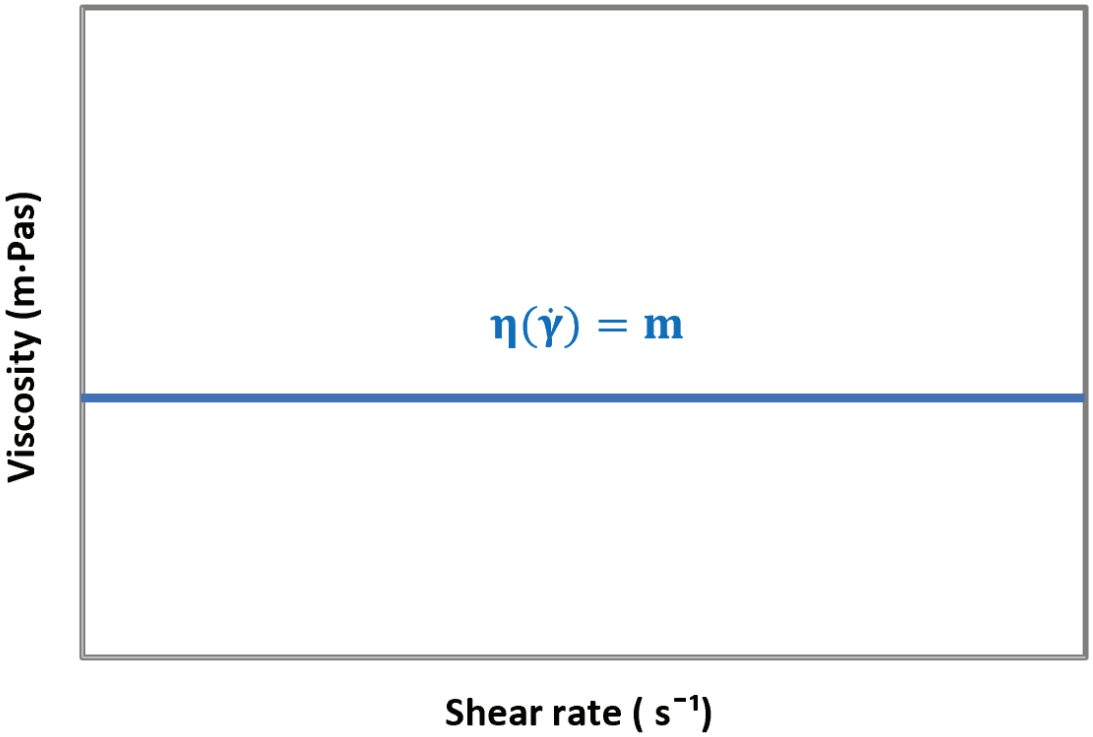

Figure 27. Viscosity vs. shear rate of a Newtonian fluid.

PART III

Compendium of articles

a. Rheological characterization of blood and plasma samples from healthy donors

Article I: Microrheometer for Biofluidic Analysis: Electronic Detection of the Fluid-Front Advancement

Authors: L. Méndez-Mora, Lourdes, M. Cabello-Fusarés, J. Ferré-Torres, C. Riera-Llobet, S. Lopez, C. Trejo-Soto, T. Alarcón, A. Hernandez-Machado

Journal: Micromachines

Year: 2021

Volume and Issue: 12 (6)

Doi: 10.3390/mi12060726

Impact Factor: 3,4

Quartile: Q2

Citations: 12

In this article, we present microfluidic rheometer, that fluid front advancement by means of electronic detection. In a previous research by Trejo et al.,[83], an microfluidic-based microrheometer was also presented, however, there are significantly differences between the two. The most important one is the detection method. While in the precedent work, the detection was made using an optical method based on a microscope and a high-speed camera, the new method proposes the electronic detection of the fluid front by integration electrodes into the microchannel, and array of pins for detection and a acquisition card to communicate to a computer. This allows for the obtention of more readings, at a

higher speed and they are automatically saved in a digital format for further analysis.

Thanks to the new method, we have obtained results of the viscosity for Newtonian fluids such as water and human plasma, as well as the viscosity of human blood samples for healthy donors at distinct hematocrit percentages (ht %). This opened up the possibility to continue forward to characterize samples from non-healthy donors at a higher pace and with more accuracy.

To test our proposed method, we performed measurements with a traditional rheometer, and compared our results, as shown in Figure 28.

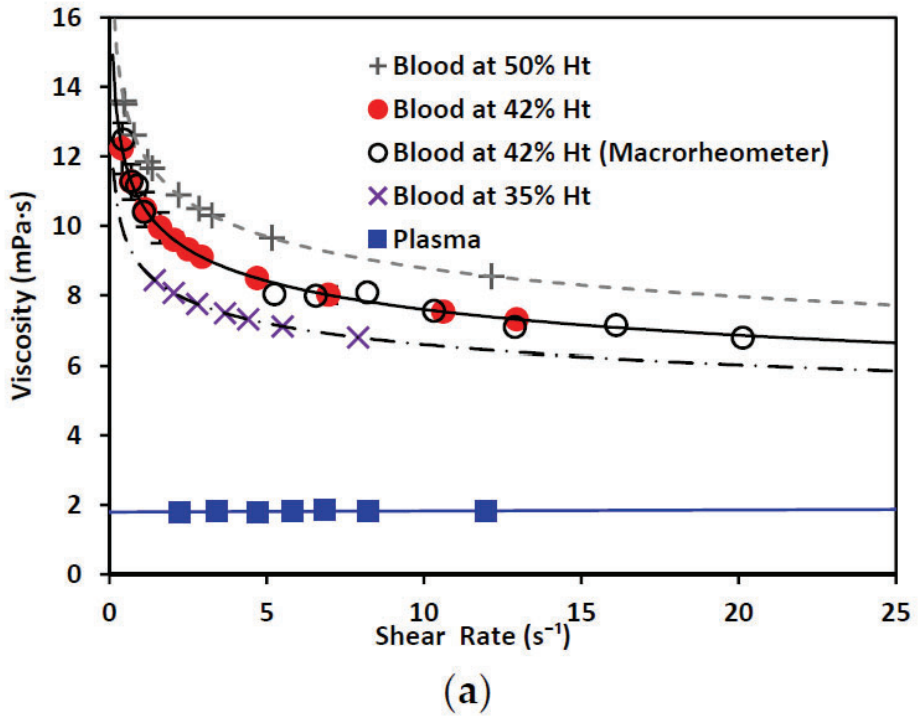

Figure 28. (a) Viscosity vs. shear rate of blood, a non-Newtonian fluid, at 50% Ht, 42% Ht, and 35% Ht. Blood at 42% Ht. using the macrorheometer (white circles). Viscosity vs. shear rate of plasma, a Newtonian fluid.

Throughout this study, it has been demonstrated that the microrheometer using electronic detection of the fluid front can deliver viscosity results comparable to those obtained using traditional equipment, while saving time and reducing the sample size and space required. At the same time, the use of microfluidics grants better control at low shear rates for shear-thinning fluids, such as blood, while

using a small amount of sample. The development of this experimental and theoretical method for blood will be useful soon to determine the presence of RBC abnormalities through the rheological characterization of blood. It could be a powerful tool for medical diagnosis in the study of diseases associated with changes in blood viscosity, operating in a wide range of shear rates.

micromachines

MDPI

Article

Microrheometer for Biofluidic Analysis: Electronic Detection of the Fluid-Front Advancement

Lourdes Méndez-Mora [1,*], Maria Cabello-Fusarés [2], Josep Ferré-Torres [1], Carla Riera-Llobet [1], Samantha López [1], Claudia Trejo-Soto [3], Tomas Alarcón [2,4,5] and Aurora Hernandez-Machado [1,2,6]

1 Department of Condensed Matter Physics, University of Barcelona (UB), 08028 Barcelona, Spain; josep.ferre@fmc.ub.edu (J.F.-T.); crierall7@alumnes.ub.edu (C.R.-L.); samantha.lopezm94@gmail.com (S.L.); a.hernandezmachado@ub.edu (A.H.-M.)
2 Centre de Recerca Matemàtica (CRM), 08193 Bellaterra, Spain; cabello.maria1@gmail.com
3 Instituto de Física, Pontificia Universidad Católica de Valparaíso, Casilla 4059, Chile; claudia.trejo@pucv.cl
4 Catalan Institution for Research and Advanced Studies (ICREA), 08010 Barcelona, Spain; talarcon@crm.cat
5 Departament de Matemàtiques, Universitat Autónoma de Barcelona (UAB), 08193 Bellaterra, Spain
6 Institute of Nanoscience and Nanotechnology (IN2UB), Universitat de Barcelona (UB), 08028 Barcelona, Spain
* Correspondence: lmendemo9@alumnes.ub.edu; Tel.: +34-(600)-895-288

Abstract: The motivation for this study was to develop a microdevice for the precise rheological characterization of biofluids, especially blood. The method presented was based on the principles of rheometry and fluid mechanics at the microscale. Traditional rheometers require a considerable amount of space, are expensive, and require a large volume of sample. A mathematical model was developed that, combined with a proper experimental model, allowed us to characterize the viscosity of Newtonian and non-Newtonian fluids at different shear rates. The technology presented here is the basis of a point-of-care device capable of describing the nonlinear rheology of biofluids by the fluid/air interface front velocity characterization through a microchannel. The proposed microrheometer uses a small amount of sample to deliver fast and accurate results, without needing a large laboratory space. Blood samples from healthy donors at distinct hematocrit percentages were the non-Newtonian fluid selected for the study. Water and plasma were employed as testing Newtonian fluids for validation of the system. The viscosity results obtained for the Newtonian and non-Newtonian fluids were consistent with pertinent studies cited in this paper. In addition, the results achieved using the proposed method allowed distinguishing between blood samples with different characteristics.

Keywords: rheometer; microrheometer; rheology; hemorheology; viscosity; blood; plasma

Citation: Méndez-Mora, L.; Cabello-Fusarés, M.; Ferré-Torres, J.; Riera-Llobet, C.; López, S.; Trejo-Soto, C.; Alarcón, T.; Hernandez-Machado, A. Microrheometer for Biofluidic Analysis: Electronic Detection of the Fluid-Front Advancement. *Micromachines* **2021**, *12*, 726. https://doi.org/10.3390/mi12060726

Academic Editor: Yutaka Kazoe

Received: 9 April 2021
Accepted: 15 June 2021
Published: 20 June 2021

1. Introduction

The study of the viscosity of biofluids, such as blood, has been used to understand their physiological mechanisms and biological functions [1]. Due to their complex properties, most biological fluids have a non-Newtonian behavior. While a Newtonian fluid shows a viscosity that is independent of the shear rate, non-Newtonian fluids' viscosity shows a dependence on the applied shear rate.

As illustrated in Figure 1, blood exhibits shear-thinning behavior. Shear-thinning fluid viscosity is characterized by a monotonically decreasing dependence on the shear rate. Such behavior is closely related to the dynamics and interactions of red blood cells (RBCs), the main cellular component of blood. Blood viscosity variation as a function of shear rate due to rheological properties of RBCs is shown in Figure 1 [2–5]. RBCs have a biconcave disklike shape at rest; they aggregate and form rouleaux structures that can, reversibly and continuously, disaggregate to single-flowing discocytes for increasing shear rates. This change in microstructure implies a viscosity variation. When RBCs circulate through the vascular system, deformability and dynamics of RBCs account for a further decrease in

blood viscosity. Furthermore, blood viscosity value strongly depends on other parameters such as temperature, whole blood cellular components (for example hematocrit value), and hemoglobin content [6].

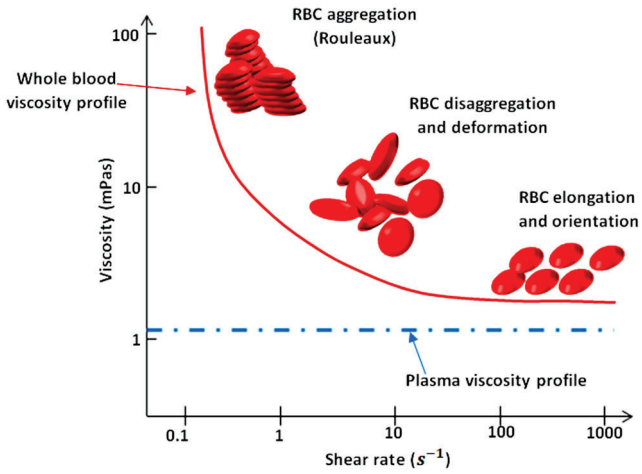

Figure 1. Viscosity profiles of whole blood and plasma. Adapted from Rosencranz [7].

The gold standard for viscosity measurements comprises a wide range of types of rheometers (instruments that measure the stress and deformation history of a material). The specific kind of rheometer that can only measure the steady shear viscosity function of a material is called a viscometer [8]. Rheometers may be differentiated on the type of flow they induce; i.e., drag flows and pressure-driven flows. Typical drag-flow rheometers are the coaxial cylinder Couette flow and coaxial cone-plate, while capillary rheometers are pressure-driven. The disadvantages of using this type of equipment include their high operation costs and the large size of samples they require. The rheometrical properties of complex fluids have been traditionally studied using such macroscopic devices.

In general, macroscopic rheometers provide less accuracy than their microfluidic counterparts. In contrast to classical methods, the study of rheology through microfluidic techniques is a widely used method to analyze the viscosity of complex fluids. Several microfluidic platforms have been developed to reach high confinement levels [9–11] (and thus, high precision), such as broader shear rate crystal microbalance (QCM) [12], laser-induced capillary wave [13], and the use of multiple microfluidic channels. This relatively new field has come up with some viscometers that measure viscosity as a function of shear rate and temperature, although most of them are not applied in biofluids. Novel microfluidic systems' accuracy is equivalent to traditional methods, being also preferable for measuring complex viscosity behavior [14] and microflows [15]. A substantial number of viscometers for biofluid characterization exist [16–18]. However, they still present disadvantages in terms of space and sample amount required.

Some new applications use lab-on-a-chip structures from diverse materials aiming for miniaturization, such as glass and polydimethylsiloxane (PDMS) [19,20]. Microfluidic techniques that use shear as a mean to understand viscosity include pressure sensing, flow-rate sensing, surface tension, coflowing streams, and diffusion-based and velocimetry-based sensing [1]. The microrheometer proposed by Solomon [21] used a mobile phone camera to detect the fluid-front advancement through a microchannel. Srivastava [22], on the other hand, proposed a microrheometer in which the measurement of viscosity was based on monitoring with a camera the capillary pressure-driven movement of fluid sample, and shear rate varied with time. The device fabrication was not simple, and required much more time and specialized equipment and materials to produce, than our PDMS on glass microchannels. By contrast, the method of detection in our device is based on an array of electrodes that automatically detect the advancement of the fluid. By adding electronic sensing, we do not need further video processing and analysis. Additionally, our

method has been demonstrated to measure viscosity of blood and differentiate between samples at distinct hematocrit levels.

The scale reduction allows for an increase in sensitivity and accuracy. Other factors such as hematocrit level, plasma, and coagulation could affect blood viscosity. On that matter, point-of-care devices such as thromboelastograph (TEG) (Haemoscope Corporation, Niles, IL, USA) and the ROTEM thromboelastometer (Pentapharm GmbH, Munich, Germany) [23,24] have led the research toward successful results for blood and plasma [25].

The technology presented here consists of a front microrheometer mainly composed of three parts: a microfluidic consumable that comprises a microchannel with an inlet and an outlet; the electronic setup, including pump, electronic detection, and data acquisition; and a mathematical model to properly convert obtained data into viscosity measurements. The electronic detection is performed with a sensor array (of metallic electrodes) located along the microchannel. This technology allows us to characterize the rheological properties of the fluid as a function of the fluid-front advancement, using a small amount of sample, reducing space required, and finally minimizing time and material consumption. The tested samples come into contact only with the walls of the microfluidic channel; therefore, there is neither a need for cleaning protocols, nor for the use of cleaning substances. Unlike other rheometers that require extensive cleaning of their components, the microfluidic chip is intended to be used as a consumable. The consumable is disposed of after each experiment. Thanks to the number of pairs of electrodes (24), situated at each side of the microchannel, it is possible to obtain a high number of data points, thus enhancing the accuracy of measurements. Finally, the integration of electronic detection into microfluidic devices improves the reliability of measurements.

The general goal of this study was to develop the method and model for a microrheometer capable of characterizing the viscosity of biofluids by analyzing the fluid-front advancement, and reducing the required sample's amount, space, and time consumption. First, we characterized the viscosity of healthy blood samples at distinct hematocrit levels. The viscosity of blood obtained at $\dot{\gamma} = 1$ was 12.2 mPa·s for the sample at 50% Ht; 10.67 mPa·s for 42% Ht; and 8.81 mPa·s for 35% Ht. These results were consistent with results obtained by other authors [26–28]. This constitutes a necessary benchmark to, in the near future, compare and detect rheological anomalies associated with hematological diseases, since the shape and biomechanical properties of RBCs can be altered in several diseases related to hematological disorders [29]. Second, we validated the new technology by comparing its results to data obtained using traditional equipment. We compared our viscosity results to results obtained using a rotational rheometer (Malvern Kinexus Pro+, Malvern Instruments Limited, Worcestershire, UK). The viscosity value obtained for blood at 42% Ht using this macrorheometer for comparison was 10.69 mPa·s.

2. Materials and Methods

2.1. Mathematical Model

The development of mathematical models describing the Newtonian and non-Newtonian characteristics of blood as a complex fluid [30,31] are very important for understanding viscosity behavior at the microscale, and determine how different blood conditions affect the viscosity values. Deformation of RBCs at high shear rates and the formation of aggregates in the form of rouleaux at low shear rates are essential aspects to keep in focus when developing models for blood [32,33].

The linear displacement of a fluid layer with respect to another in the time interval dt allows obtaining the rate of displacement (or velocity). If we consider a fluid flow moving into the x direction between two plates, the only nonzero velocity component is v_x, which varies in the z direction due to the interaction with the planes, being $\vec{v} = \{v_x(z), 0, 0\}$. The shear rate is the rate of change of velocity at which one layer of fluid passes over an adjacent layer. The shear produced between the layers depends on the z dimension, and is:

$$\dot{\gamma}(z) = (dv_x(z))/dz \quad (1)$$

An easy method to study fluid flow consists of the study of the fluid-front (fluid–air interface) advancement. In a microfluidic channel, the front velocity, $\dot{h}(t)$, is the change in position of the fluid, $h(t)$, through time along the microfluidic channel. The term $h(t)$ is defined as the average position of the front $h(t) = \frac{1}{n}\sum_{j=1}^{n} h_j(t)$, where $h_j(t)$ is the fluid-front position with respect to z, as shown in Figure 2. One of the advantages of working with the mean front velocity is that its value is independent of the z position. The theoretical model used assumes that velocity inside the microchannel behaves according to Darcy's law. In past experiments [34], Trejo C. observed that this theoretical description of the velocity of the fluid inside the microchannel held for microchannels of 1 mm width and heights over 150 um. To test distinct aspect ratios, the authors considered microchannels of different heights: b = 300 µm, b = 200 µm, b = 150 µm, and b = 50 µm; width w = 1 mm; and length lc = 4 cm. For heights lower than 150 um the model is not longer valid.

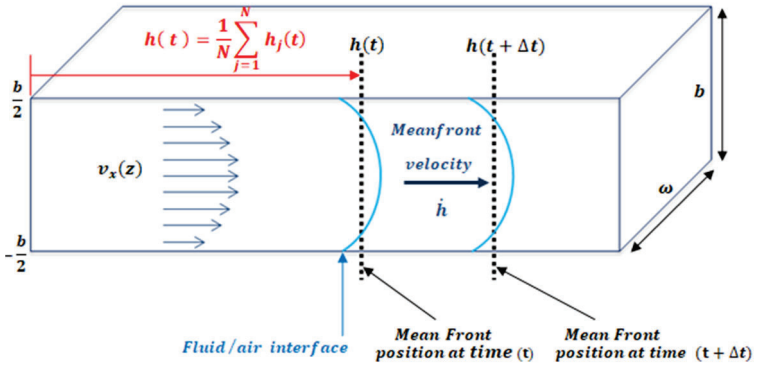

Figure 2. The velocity $v_x(z)$ is the x component of velocity inside the microfluidic channel as a function of height (z); $h(t)$ indicates the mean position of the fluid front. The channel dimensions satisfy the relation $b/\omega \ll 1$.

By studying the fluid/air interface, the shear rate $(\dot{\gamma})$ can be defined as the normalization of the mean front velocity, $\dot{h}(t)$, according to the microchannel height, b, as defined by Equation (1) (see Figure 2).

$$\dot{\gamma} = \frac{\dot{h}}{b} \tag{2}$$

The viscosity of non-Newtonian fluids can be described using different models according to the characteristics of each fluid. The most commonly used are the Carreau–Yasuda and power-law models [35]. The power-law model, also known as the Oswaldt–De Waele fluid model, describes the viscosity of a fluid on dependence of its shear rate:

$$\eta(\dot{\gamma}) = m\dot{\gamma}^{n-1} \tag{3}$$

where the prefactor m corresponds to the value of viscosity at $\dot{\gamma} = 1$. The exponent n indicates the nature of the viscosity of the studied fluid. Depending on the value of n, the behavior of a fluid is characterized as Newtonian or non-Newtonian. Values of $n < 1$ correspond to shear-thinning behavior, while $n > 1$ corresponds to shear-thickening behavior. On the other hand, Newtonian fluids have a value of $n = 1$.

Using the Stokes equation, it is possible to calculate the flow through a known geometry as a function of the average velocity. In most cases, microfluidic systems are composed of pressure sources and microfluidic channels connected by cylindrical tubing, creating coupled fluidic systems. The flows passing through two coupled geometries are equivalent due to the mass conservation principle. The mathematical deductions concerning these calculations are detailed in Appendix A.1.

In a closed system composed of a pressure source, a fluid reservoir, and the coupling of tubing with a microchannel of rectangular cross-section, the pressure inside the rectangular microchannel, ΔP, is the summation of all the pressures in the system, as shown in Figure 3.

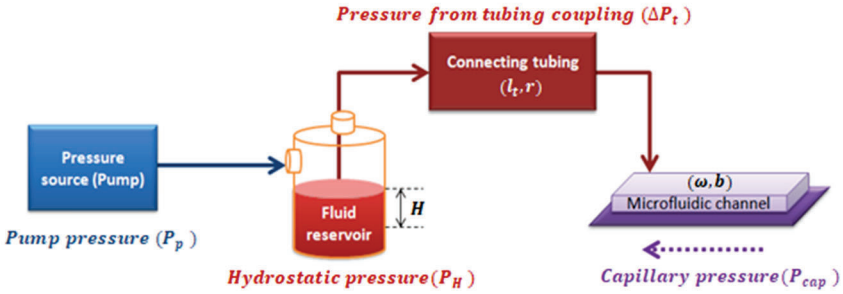

Figure 3. Diagram of the pressures involved in the system.

As properly deduced in Appendix A.2, the effective pressure (P_{eff}) is defined as the pressure resulting from the combination of the pumping system pressure, the capillary pressure, and the hydrostatic pressure into the whole system shown in Figure 3 (see Equation (A25) deduced in Appendix A.2). Effective pressure P_{eff} has an algebraic dependence with $\dot{\gamma}$:

$$P_{eff} = K(m,n)\dot{\gamma}^n \tag{4}$$

where all the independent variables are grouped in K, which depends on the fluid properties (m and n) and the geometrical parameters of the system shown in Equation (4):

$$K(m,n) = m2l_t\left(\frac{\omega b^2}{\pi r^2}\right)^n\left(\frac{1}{r^{1+n}}\right)\left(\frac{1}{n}+3\right)^n \tag{5}$$

According to the mass conservation principle, in our system, $Q_c = Q_t \rightarrow \omega b\dot{h} = \pi r^2 v_t$ (Appendix A.2). This is why we can write velocity inside the tubing as a function of the velocity measured inside the microchannel, $\dot{h}$:

$$v_t = \eta\frac{8l_t b\omega}{\pi r^4}\dot{h} \tag{6}$$

2.2. Experimental Model

2.2.1. General Case: Non-Newtonian Fluids

We used a coupled system in which a tube was connected to a microchannel structure. The effective pressure, P_{eff}, acting in the system (see Figure 3) caused fluid to flow through the coupled system. Through electronic detection, the mean front velocity was measured along the microfluidic channel. By calculating velocity values and the channel dimensions, shear-rate values were obtained. By plotting P_{eff} vs. shear rate, and fitting a curve for the relation between P_{eff} and $\dot{\gamma}$, we obtained:

$$P_{eff} = A\dot{\gamma}^n \tag{7}$$

Terms A and n can be obtained from Equation (6). By equating experimental data in Equation (5) with the mathematical model in Equations (3) and (6), we could calculate the value of m as follows:

$$m = \frac{A}{2l_t\left(\frac{\omega b^2}{\pi r^2}\right)^n\left(\frac{1}{r^{1+n}}\right)\left(\frac{1}{n}+3\right)^n} \tag{8}$$

Once n and m were obtained, the viscosity values of a fluid were calculated using the power-law model in Equation (2).

2.2.2. Newtonian Fluids

A Newtonian fluid has a constant viscosity. In opposition to non-Newtonian fluids, it does not depend on the applied pressure. Analogously, as it has been done in the general case, the mathematical model for Newtonian fluids ($n = 1$) is shown in Appendix A.3.

Pressure for the entire system is described in Equation (8), which has a linear dependence on the mean front velocity.

$$P_{eff}(m, n = 1) = K(m, n = 1)\dot{\gamma} \quad (9)$$

For the Newtonian case, K can also be expressed in terms of the geometry of the system and the experimentally obtained front velocity:

$$K(m, n = 1) = m\frac{8\omega b^2 l_t}{\pi r^4} \quad (10)$$

Along the same lines, the experimental data of the shear rate values obtained from applying a known pressure to a Newtonian fluid have the linear relation shown in Equation (10):

$$P_{eff} = A\dot{\gamma} \quad (11)$$

Using the experimental results alongside the mathematical model, m can be calculated as:

$$m(n = 1) = \frac{A}{\frac{8\omega b^2 l_t}{\pi r^4}} \quad (12)$$

In Newtonian fluids for which $n = 1$, the power-law equation for viscosity in Equation (2) can be re-written as:

$$\eta = m \quad (13)$$

2.3. Experimental Method

The experiments were performed using microfluidic chips made of polydimethylsiloxane (PDMS) attached to glass substrates $(2.6 \times 7.6\ cm^2)$ by using plasma bonding; schematics of the final structures are shown in Figure 4a. The glass substrates had a printed pattern of 24 pairs of gold electrodes, which were in contact with the flowing fluid. The electrodes had a 350 μm separation in between, and were in the form of 4 groups of 6 pairs located along the length of the channel. The distance between each set was 8.5 mm (Figure 4b). The channel width was $\omega = 1000$ μm, the channel height was $b = 300$ μm, and the length from inlet to outlet was $l_c = 4$ cm. Commonly, PDMS, glass, and Cole Parmer Tygon tubing are employed due to their good biocompatibility, low cost, and high adaptability.

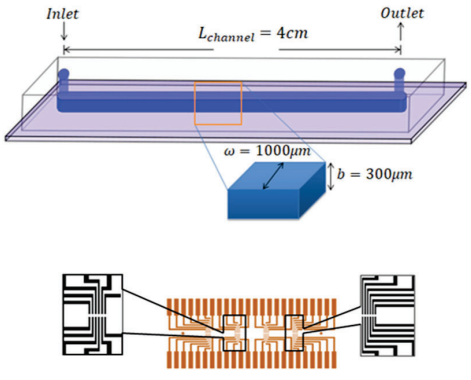

Figure 4. Schematics of the microfluidic consumable. (**a**) The microfluidic channel made of PDMS sealed on a glass substrate. The channel dimensions are $\omega = 1000$ μm, $b = 300$ μm, and $L_c = 4$ cm. (**b**) Gold electrodes printed on the glass surface and beneath the PDMS layer.

The experimental setup used to carry out the experiments was composed of a pressure pump (Dolomite Fluika) connected to a closed fluid reservoir. From the reservoir, Tygon tubing with an internal radius $r = 127$ μm and length $l_t = 20$ cm was connected to the microchannel. The pressure exerted on the fluid was set using a simple graphic interface,

which controlled the pressure pump's performance. A schematic representation of the experimental setup described is presented in Figure 5. Different pressures for the Fluika Pump were set to run the experiment, ranging from 500 Pa to 5000 Pa. Each electrode was connected via a pin array box to a National Instruments control card. As soon as the pressure began to be applied, electronic reading was activated by the controller of a myRIO National Instruments card. This tool communicated with the fluidic pump and the electronic reading pins through a computer. The sample fluid came out from the reservoir at the set pressure and went directly into the channel. As the fluid came into contact with the electrodes, the time required for the fluid front to reach each electrode pair inside the microfluidic channel was obtained. Using the time data and the geometry of the microfluidic system, it was possible to calculate the fluid-front velocity between electrode pairs through the microchannel.

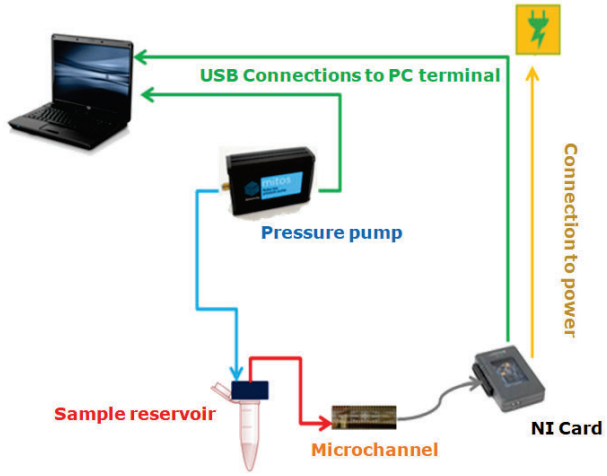

Figure 5. Experimental setup for laboratory use.

Ten samples of 500 µL from each different test fluid were used during this study: (fluid standard MGVS60, deionized water (DI water), plasma, and blood from healthy donors). We selected MGVS60, a viscosity standard tested in strict accordance with ASTM D2162, the primary method for viscosity standards calibration that is typically used for the calibration and verification of viscosity-measuring equipment. Its viscosity is 6.00 mPa·s at 24 °C. Deionized water was selected because its viscosity is constant and known: $\eta = 1.01$ mPa·s [36]. Blood samples and their respective plasma were provided in 10 mL tubes by Banc de Sang i Teixits (Barcelona, Spain), from 10 anonymous healthy donors. The use of these samples was authorized by the Bioethics Committee of the University of Barcelona (IRB 00003099).

To obtain the plasma samples, we centrifuged whole blood samples at 2500 rpm for 5 min. The plasma that rested at the top was collected with a pipette. Samples were prepared at three different hematocrit concentrations, Ht (%) of 50%, 42%, and 35%. These were prepared by taking plasma previously separated from whole blood and then adding to it the desired volume of RBCs corresponding to each hematocrit percentage. The hematocrit selected for further comparison to a benchtop device was 42% Ht, consistent with the levels found in healthy adults. All the tests were performed at room temperature (25 °C) and, for the case of blood, within two days of extraction, to avoid cell damage from aging [28]. At the beginning of each experiment, the DI water was evaluated to guarantee that the setup was properly calibrated.

3. Experimental Results and Discussion

For a correct rheological characterization of the fluid, it was necessary to properly determine the pressures inside the system (Figure 3). The pressure set for the pumping source (P_p) was automatically recorded. Considering that a sample of 500 µL inside a

reservoir supposes a height, $H = 5$ mm, the contribution generated by the hydrostatic pressure ($P_H = \rho gH$) can be obtained. Parameters for the different tested fluids at room temperature can be found in Table 1. The material used for the microchannel was hydrophobic, meaning that it opposed the fluid-front advancement. Fluid-front images at different pressures were obtained by using a camera and an inverted microscope. The contact angle, θ, was extracted optically via Image J free software. The surface tension (τ) of the standard fluid was experimentally measured with a capillary tube with an internal diameter of 1.15 mm [37,38]. By using Equation (A20) deduced in Appendix A.2, it was possible to calculate P_{cap} for a rectangular cross-section channel at each measured pressure by analyzing the fluid-front contact angle. The contact angle also depended on the fluid being analyzed and the total pressure applied. The curvature of the fluid–air interface was expected to be almost constant for water, standard MGVS60, and plasma; however, it changed as the pressure was increased when measuring blood (Table 2).

Table 1. Characteristic values for water, MGVS60 plasma, and blood.

Sample	$\rho(\frac{kg}{m^3})$ at 25 °C	P_H(Pa) at H = 5 mm	$\tau(\frac{N}{m})$ at 25 °C	θ(°)
Water	1000	49.00	0.072	102.42
MGVS60	1134	55.56	0.107	106.90
Plasma	1025	50.22	0.057	102.27
Blood	1050	51.45	0.058	* (Table 2)

* Contact angle for blood was nonconstant at different pressures. See Table 2.

Table 2. Contact angle and capillary pressure at each pump pressure applied for healthy blood at 42% hematocrit and RT (25 °C). P_{cap} was obtained using Equation (A20).

P_p(Pa)	θ(°)	P_{cap}(Pa)
500	103.24	115.11
1000	106.94	146.46
1500	109.60	168.62
2000	111.76	186.35
2500	113.62	201.37
3000	115.27	214.54
3500	116.76	226.35
5000	120.64	256.22

When studying blood-front behavior, dependence between the applied pressure and the dynamic contact angle measured was observed. Hence, P_{cap} depended on the applied pressure, P_p. To obtain the contact angle of blood inside our microfluidic channel, we conducted a separate experiment for blood at 42% Ht. By using a microscope (Optika XDS-3, Optika SRL, Bergamo, Italy) and a high-speed camera (Photron Fastcam SA3, Photron Limited, Tokyo, Japan), we captured images of the fluid front at different set pressures, P_p. We measured the contact angle using the angle-measurement tool in Image J, as depicted in Figure A2. Calculation of P_{cap} was done as per Appendix A.2. The obtained contact angle when changing the applied pressure and thus, the capillary pressure obtained can be seen in Table 2. The contact angles of blood used in this paper have been considered independent of the Ht (%) value.

To validate our setup and the use of electronic detection as a proper method to determine viscosity for Newtonian fluids, two different strategies were followed: first, a Newtonian standard fluid and DI water with reported viscosity value were evaluated. Second, the obtained results with our technology were compared to the results obtained with a commercial macrorheometer, the Malvern Kinexus Pro+ (Malvern Instruments Limited, Worcestershire, United Kingdom).

From the data obtained (applied pressure and time), knowing the device geometry, resistances, and the pressures added to the system, it was possible to plot the effective pressure as a function of shear rate for each sample.

A linear fit of the data obtained when plotting the applied pressure with an external pressure pump (P_p) as a function of $\dot{h}$ or $\dot{\gamma}$ is shown in Figure 6. It was used to determine P_{eff} for Newtonian fluids, as detailed in Equation (A33), as:

$$P_{eff}(n=1) = m\frac{8\omega b l_t}{\pi r^4}\dot{h} = m\frac{8\omega b^2 l_t}{\pi r^4}\dot{\gamma} \quad (14)$$

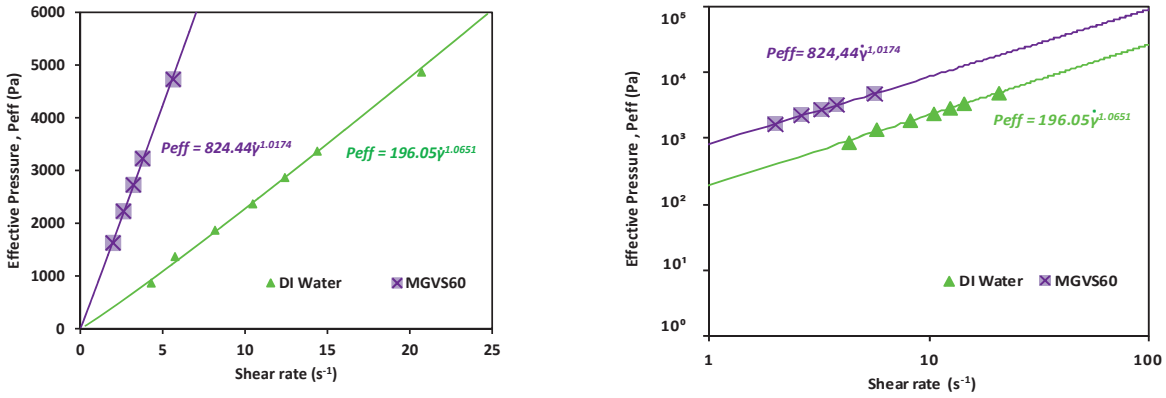

(**a**) (**b**)

Figure 6. Effective pressure vs. shear rate obtained for the Newtonian calibration fluids studied. Newtonian fluids: DI water and MGVS60: (**a**) linear scale and (**b**) log-log scale.

As shown in Figure 6 and detailed in Table 3, in both cases, n was very close to 1, which indicated that the fluid was Newtonian, compatible with the behavior expected for both.

Table 3. Viscosity obtained using the developed microrheometer (with the corresponding n values obtained) and a commercial macrorheometer and electronic detection methods. The samples analyzed were DI water and MGVS60, a commercial standard fluid.

Sample	Viscosity (mPa·s) Microrheometer	n	Viscosity (mPa·s) Macrorheometer
DI water	1.08 ± 0.03	1.017	1.02 ± 0.01
MGVS60	5.87 ± 0.05	1.065	5.88 ± 0.02

From these data, as previously explained, the viscosity could be obtained by using Equation (13). These results were compared to those obtained with a commercial macrorheometer (see Figure 7).

Water has been found to exhibit a constant viscosity of $\eta \approx 1.002$ mPa·s [39]. The same results were obtained with both rheometers (differing from each other by 3%). The viscosity obtained with the standard MGVS60 was around $\eta \approx 5.55$ mPa·s using the microrheometer, while the macrorheometer delivered a viscosity of 5.8 mPa·s. The expected value for this fluid was 6.00 mPa·s.

These results validated that the accuracy of the new electronic sensing method was adequate (equivalent to standard macrorheometer measures) regarding the measurement of viscosity in an automatic, fast, and effective way.

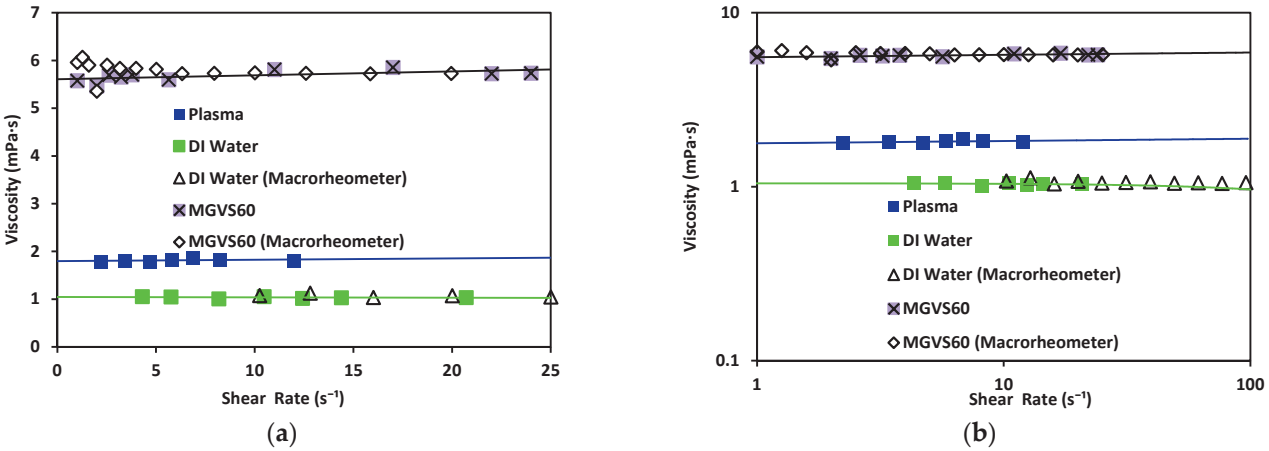

Figure 7. Viscosity vs. shear rate using the microrheometer for DI water (green) and standard MGVS60, and using the macrorheometer: (**a**) linear scale and (**b**) log–log scale.

Once the measurement system was validated for Newtonian fluids with known characteristics, the experiment was repeated with plasma and blood at different % Ht values. The results are shown in Figure 8.

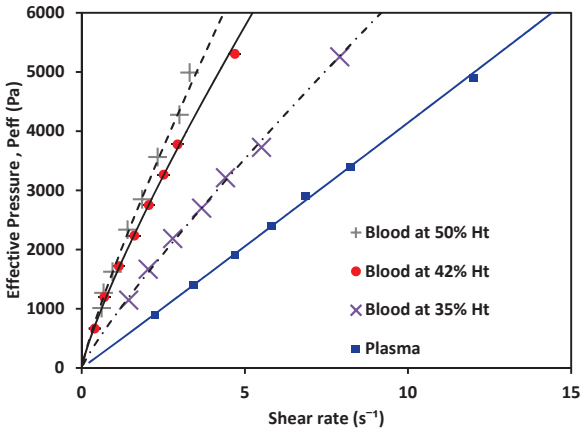

Figure 8. Effective pressure vs. shear rate of blood, a non-Newtonian fluid, at 50% Ht, 42% Ht, 35% Ht; and plasma, a Newtonian fluid.

The behavior of the shear rate as P_{eff} applied to the fluid variance is shown in Figure 8. Non-Newtonian fluids (in this case, blood as a shear-thinning fluid) showed a nonlinear relation between the pressure and their shear-rate response, while plasma showed a Newtonian behavior. Using the experimentally obtained values alongside Equations (6) and (7) for the non-Newtonian case, and Equations (10) and (11) for the Newtonian cases, the value of K could be calculated. Then, m and n were obtained. The values for each are shown in Table 4 (see references in Appendix B); water and MGVS60 values are also included.

Table 4. Values for prefactor m and n for Newtonian and non-Newtonian fluids.

Sample	m (Pa·s)	n
*Blood at 50% Ht	0.0122	0.8500
*Blood at 42% Ht	0.0107	0.8519
*Blood at 35% Ht	0.0088	0.8720
MGVS60	0.0058	1.0174 ± 0.002
Plasma	0.0018 ± 0.0002	1.0131 ± 0.028
Water	0.0010 ± 00101	1.0651 ± 0651

*Blood viscosity values presented at $\dot{\gamma} = 1$.

With the effective pressure, and after obtaining m and n (Table 4), viscosity plots were obtained. Viscosity was calculated using Equation (2) (for non-Newtonian fluids: blood at different Ht (%). levels) and Equations (11) and (12) (for Newtonian fluids: plasma).

As depicted in Figure 9, plasma exhibited Newtonian behavior with a constant viscosity, between 1.50–1.81 mPa·s [40]. Blood exhibited shear-thinning behavior, as its viscosity decreased as the shear increased. Note that the viscosity of blood at 42% Ht (see Figure 9) varied from 12 to 7 mPa·s within the $\dot{\gamma}$ range evaluated, with a value of viscosity 10.67 mPa·s at $\dot{\gamma} = 1\ s^{-1}$; blood at 50% Ht had a viscosity of 12.2 mPa·s; and blood at 35% Ht had the lowest viscosity of the three tested hematocrit levels, 8.8 mPa·s. At a constant shear rate, the viscosity of blood increased as the hematocrit grew. This also demonstrated that our new device could be used to distinguish between different hematocrit levels. The hematocrit selected for further comparison to a benchtop device was 42%, consistent with the levels found in healthy adults. The viscosity obtained by this method was 10.69 mPa·s. for blood at 42% Ht. This can be compared to results also obtained under room-temperature conditions by consulted authors, who situated the viscosity of blood at $\dot{\gamma} = 1\ s^{-1}$ between 9–10 mPa·s [40]. Dispersion in the measurements at the low shear-rate values observed in Figure 9 would be reduced by increasing the number of samples studied. With a sufficiently large N, a general curve and validity intervals for healthy blood could be obtained, which would indicate what the behavior of the viscosity must be as a function of the shear rate in a healthy patient (at a constant hematocrit value).

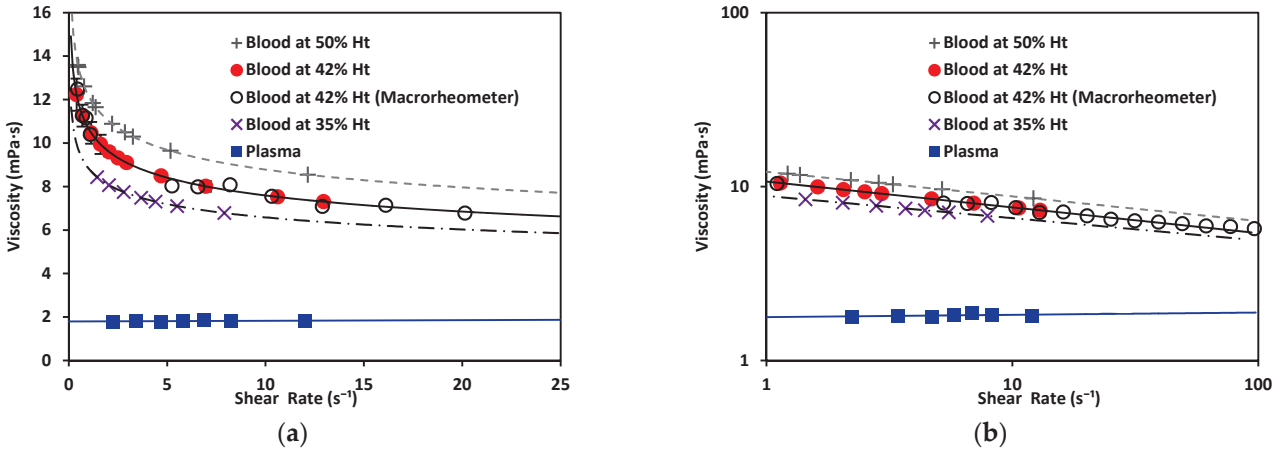

Figure 9. (**a**) Viscosity vs. shear rate of blood, a non-Newtonian fluid, at 50% Ht, 42% Ht, and 35% Ht. Blood at 42% Ht using the macrorheometer (white circles). Viscosity vs. shear rate of plasma, a Newtonian fluid. (**b**) Viscosity vs. shear rate of non-Newtonian and Newtonian fluids in log–log scale.

Regarding the rheological properties of RBCs, blood showed higher resistance to flow at low $\dot{\gamma}$ values. In contrast, at higher values of $\dot{\gamma}$, blood showed a more Newtonian behavior, which was reflected in the nearly flat region on the viscosity vs. shear rate plot. This distinct shear-thinning curve behavior could only be properly observed when shear rates as low as $1\ s^{-1}$ were reached. For this reason, it was important to choose a range of pressure that allowed for this $\dot{\gamma}$ regime to be available. Residual fit for both methods was a useful way to determine the accuracy differences between our technology and a commercial rheometer (see Figure 10).

Residuals, R, for the micro- and macrorheometer were calculated as the difference between experimentally obtained viscosity, η, and predicted viscosity, $\eta_{Predicted}$ (Equation (14)).

$$R = \eta - \eta_{Predicted} \quad (15)$$

The theoretically predicted viscosity of blood, $\eta_{Predicted}$, for both methods was obtained by calculating viscosity at each shear rate, using the fit of viscosity vs. shear rate

from plots in Figure 9. For the micro- and macrorheometer, the calculation was made using Equations (15) and (16) respectively:

$$\eta_{\text{Predicted micro}} = 10.674\dot{\gamma}^{-0.148} \quad (16)$$

$$\eta_{\text{Predicted macro}} = 10.687\dot{\gamma}^{-0.146} \quad (17)$$

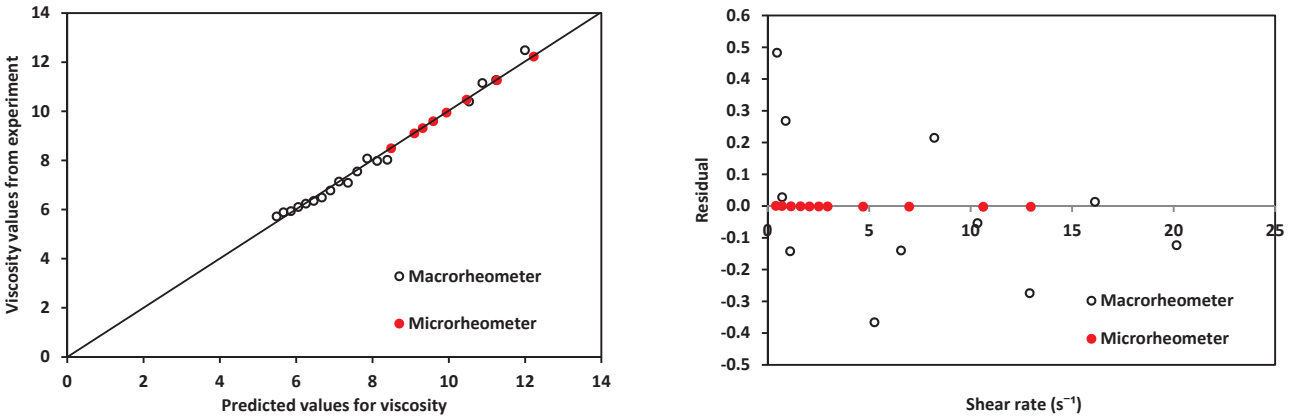

(**a**) (**b**)

Figure 10. (**a**). Experimentally obtained viscosity values vs. predicted values for both devices using blood. (**b**) Residuals for macro and microrheometers.

A good correlation was observed when plotting experimentally obtained values for viscosity and theoretically predicted values using the power-law model shown in Figure 10a, thus confirming that the experimentally obtained data was close enough to theoretically expected values. In addition, residuals' plotted vs. predicted values in Figure 10b show that the macrorheometer residuals were larger than those obtained with our microrheometer. The accuracy of the prediction for the macrorheometer in this experiment was lower than the accuracy of our microrheometer by three orders of magnitude. Residuals for our microrheometer were closer to zero. At these low shear rates, from 1 to 25 s^{-1}, our technology performed with higher accuracy. This could be explained by the fact that blood is a complex fluid of the shear-thinning type. We decided to work on this $\dot{\gamma}$ window to obtain the nonlinear viscosity of blood and to avoid hemolysis. Our microrheometer had the advantage of being able to operate under low shear conditions with high stability. This makes it suitable for applications such as the analysis of blood, where low-shear-rate performance is necessary. At the shear-rate values required to observe the non-Newtonian behavior of blood, the microrheometer results presented herein had a smaller deviation. This can be attributed to the high stability at low shear rates. These low shear rates could be reached thanks to the size reduction achieved by using a microchannel. Moreover, a benchtop rheometer for laboratory use also requires a rather large sample of blood. For the macrorheometer experiments, the sample amount was 1.19 mL for each run. The microrheometer required samples of approximately 250 µL; this constituted 21% of the sample required for the benchtop device.

4. Conclusions

The technology presented here was based on the detection of the advancement of the fluid front using electrodes printed underneath a microfluidic channel. The accuracy of the method was tested by measuring the viscosities of plasma, DI water, and a commercial viscosity standard. Experiments to measure human blood viscosity also were performed. Unlike other microfluidic capillary viscometers, the microrheometer presented here was based on the detection of the fluid/air interface as it advanced through a microchannel. Through the experimental method described, it was possible to produce a series of shear

rates that constituted a proper range to observe how the viscosity of non-Newtonian fluid changed as the applied pressure increased. Effective pressure, the pressure acting on the fluid is composed of all the interactions between the pressures acting in the system.

The characterization of the non-Newtonian behavior was obtained by applying the power-law model in Equation (2). The experimentally obtained results included a shear-rate window range of less than 1 s^{-1} up to 100 s^{-1} for both Newtonian and non-Newtonian fluids. The values obtained for viscosity—1.05 mPa·s for water and 1.8 mPa·s for plasma—fell in line with the values found in the literature [36,39]. Alternatively, we used the calibration standard MGVS60 to test the accuracy of the setup and obtained a viscosity value of 5.88 mPa·s, showing a difference of less than 2% from the target viscosity indicated by the manufacturer at 24 °C. On the other hand, blood results showed shear thinning behavior, due to the presence of mainly red blood cells, under normal morphological conditions [2]. This confirmed that the experimental conditions were adequate to observe the shear-thinning behavior and the action of red blood cells on the viscosity of the whole fluid. The viscosity of blood at $\dot{\gamma} = 1$ was 12.2 mPa·s for the sample at 50% Ht; 10.67 mPa·s for 42% Ht; and 8.81 mPa·s for 35% Ht. In addition, the viscosity value obtained for blood at 42% Ht using a macrorheometer for comparison was 10.69 mPa·s. As expected, as the hematocrit level increased, so did the value of viscosity. We therefore concluded that the new method proposed in this article is a reliable and accurate device that exhibits a degree of sensitivity capable of differentiating between these distinct hematocrit percentages. In addition, we measured the viscosity of DI water, MGVS60, and blood using a macroscopic rheometer for comparison purposes. Focusing on non-Newtonian fluids, we compared the behavior of the residuals of blood viscosity obtained with both rheometers.

Throughout this study, it has been demonstrated that the microrheometer using electronic detection of the fluid front can deliver viscosity results comparable to those obtained using traditional equipment, while saving time and reducing the sample size and space required. At the same time, this technique permits a better control at low shear rates for shear-thinning fluids, such as blood. The development of this experimental and theoretical method for blood will be useful in the near future to determine the presence of RBC abnormalities through the rheological characterization of blood. It could be useful for medical diagnosis in the study of diseases associated with changes in blood viscosity, operating in a wide range of shear rates [41].

Author Contributions: Conceptualization, A.H.-M.; investigation, L.M.-M.; supervision, C.T.-S., A.H.-M. and T.A.; validation, C.R.-L.; visualization, J.F.-T. and S.L.; writing—original draft, L.M.-M.; writing—review and editing, M.C.-F. All authors have read and agreed to the published version of the manuscript.

Funding: This research was funded by Generalitat de Catalunya, under grants number 2018 DI 068 and 2018 DI 064; Ministry of Economy and Competitivity (MINECO) under grants number MTM2015-71509-C2-1-R, MDM-2014-0445 and FIS2016-78883-C2-1P; Ministerio de Ciencia e Innovación (Spain) under grant number PID2019-106063GB-100; AGAUR (Generalitat de Catalunya) under project 2017 SGR-1061; ANID/PCI CONICYT (Chile) under project MEC80180021.

Institutional Review Board Statement: The study was conducted according to the guidelines of the Declaration of Helsinki, and approved by the University of Barcelona's Bioethics Commission (CBUB) (Project 160016 and date of approval 1 March 2016).

Informed Consent Statement: All the samples were obtained by Banc de Sang I Teixits with the informed consent of the subjects. All the donors are anonymous and healthy. The samples were analytical surplus blood without information or personal data. The blood samples were going to be extracted for routine analysis purposes regardless of this study. The results herein obtained would not affect clinical decisions about the individuals' care.

Data Availability Statement: Data is contained within the article.

Acknowledgments: Lourdes Méndez-Mora and Josep Ferré-Torres acknowledge support from Generalitat de Catalunya under the program Doctorat Industrial (2018 DI 068) and (2018 DI 064). T.A. acknowledges the Spanish MINECO for funding under grant MTM2015-71509-C2-1-R. Tomas

Alarcón acknowledges further support from the Ministry of Economy and Competitivity (MINECO) for funding awarded to the Barcelona Graduate School of Mathematics under the "Maria de Maeztu" program; grant number MDM-2014-0445. Tomas Alarcón has been partially funded by the CERCA Programme of the Generalitat de Catalunya. Aurora Hernandez-Machado acknowledges support from MINECO (Spain) under project FIS2016-78883-C2-1P, Ministerio de Ciencia e Innovación (Spain) under project PID2019-106063GB-100, and AGAUR (Generalitat de Catalunya) under project 2017 SGR-1061. Claudia Trejo-Soto and Aurora Hernandez-Machado acknowledge partial support from ANID/PCI CONICYT (Chile) under project MEC80180021. Along the same lines, the authors extend their gratitude toward Rheo Diagnostics S. L. for making this research possible.

Conflicts of Interest: The authors declare no conflict of interest.

Appendix A

Appendix A.1. Flow Inside a Known Geometry

The flow passing through a known geometry can be obtained as the product of the mean velocity of the fluid multiplied by the cross-section area. The model described herein corresponds to a structure formed by a tubing of length, l_t, and internal radius, r_t, connected into a microfluidic channel of dimensions ω and b. The resistance inside a known geometry is defined by the relation $R_t = \frac{\Delta P}{Q}$. The pressure loss inside the tubing is:

$$\Delta P_t = \eta \frac{8 l_t}{r^2} v_t \tag{A1}$$

According to the mass conservation principle, in our system, $Q_c = Q_t \rightarrow \omega b \dot{h} = \pi r^2 v_t$; therefore, we write velocity inside the tubing as a function of the velocity measured inside the microchannel:

$$v_t = \eta \frac{8 l_t b \omega}{\pi r^4} \dot{h} \tag{A2}$$

The flow can also be obtained from the integration process of mean velocity along with the geometry; a cylinder (the flow into a tube or pipe) or between parallel walls (a rectangular cross-section channel that satisfies the relation $b/\omega \ll 1$). Using cylindrical coordinates of the Stokes [42] equation, an expression for ΔP_t can be obtained, utilizing the average flow velocity inside the tube, v_t:

$$\frac{1}{r} \frac{\partial}{\partial r} \left(\eta r \frac{\partial v_t}{\partial r} \right) = \nabla P_t \tag{A3}$$

where $\nabla P_t = \frac{\Delta P_t}{l_t}$ and ΔP_t is the pressure inside the cylindrical geometry. Defining shear rate as $\dot{\gamma} = \frac{\partial v}{\partial r}$ and using the power-law model in Equation (2) ($\eta(\dot{\gamma}) = m\dot{\gamma}^{n-1}$), the previous equation can be written as follows:

$$\dot{\gamma} = \left(\frac{\Delta P_t}{2 l_t m} r \right)^{\frac{1}{n}} \Rightarrow \Delta \frac{\partial v_t}{\partial r} = \left(\frac{\Delta P_t}{2 l_t m} \right)^{\frac{1}{n}} r^{\frac{1}{n}} \tag{A4}$$

By integrating this expression while imposing a non-slip boundary condition, $v_z(r = R) = 0$, we obtain the velocity component $v_z(r)$:

$$v_z(r) = \left(\frac{\Delta P_t}{2 l_t m} \right)^{\frac{1}{n}} \left(\frac{1}{\frac{1}{n+1}} \right) \left(r^{\frac{1}{n}+1} - R^{\frac{1}{n}+1} \right) \tag{A5}$$

Now, an equation for the flow rate, Q_t, can be defined:

$$Q_t = \int_0^{2\pi} d\theta \int_0^r v_z(r') dr' = r^{\frac{1}{n}+1} \pi r^2 \left(\frac{\Delta P_t}{2 l_t m} \right)^{\frac{1}{n}} \left(\frac{1}{\frac{1}{n}+3} \right) \tag{A6}$$

To determine the flow in a rectangular microchannel, we first need to know the velocity of a plane Poiseuille flow, $v_x(z)$, using the non-slip boundary condition at the position of the solid plates $v_x(z = \pm b/2) = 0$:

$$v_x(z) = \left(\frac{\Delta p}{m h(t)}\right)^{1/n} \left(\frac{1}{\frac{1}{n}+1}\right) \left(z^{\frac{1}{n}+1} - \left(\frac{b}{2}\right)^{\frac{1}{n}+1}\right) \quad \text{(A7)}$$

where ΔP is the pressure inside the microchannel and h(t) is the position of the fluid interface inside the microchannel.

The resulting equation for the flow rate inside the microchannel is:

$$Q = \omega \int_{\frac{-b}{2}}^{\frac{b}{2}} v_x(z)dz = 2\omega \left(\frac{\Delta P}{m h(t)}\right)^{\frac{1}{n}} \left(\frac{b}{2}\right)^{\frac{1}{n}+2} \left(\frac{1}{\frac{1}{n}+2}\right) \quad \text{(A8)}$$

where Q is the flow inside the channel and Q_t is the flow inside the tubing. The term l_t is the tubing length and r is its internal radius. ΔP is the pressure inside the rectangular geometry and ΔP_t is the pressure inside the cylindrical geometry. These parameters can be seen in Figure A1a,b.

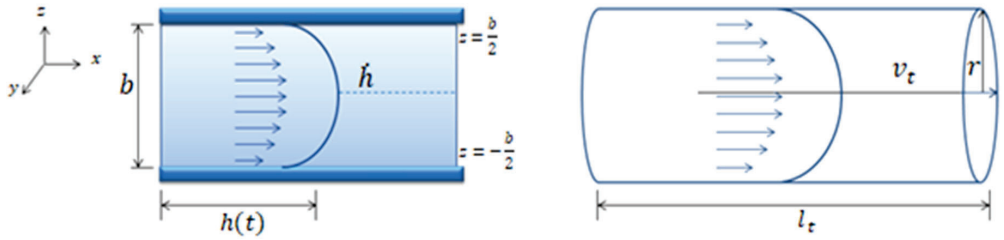

(a) **(b)**

Figure A1. (**a**) Schematic representation of a Poiseuille flow between two parallel walls separated at a distance b. The mean front velocity, $\dot{h}$, and the flow inside the microfluidic channel is $\left(Q = \dot{h}\omega b\right)$. (**b**) Schematic representation of Poiseuille flow in a cylindrical tube of radius r and length l_t. The velocity, is the mean velocity of the fluid inside the cylindrical tube and Q_t is the flow inside the tube ($Q_t = \pi r^2 v_t$).

Given current micromanufacturing techniques, the microchannels are mainly rectangular. Microfluidic systems often need pneumatic systems to apply pressure. To make the connections between the pneumatic systems and the microchannels, tubes are used, with different radii depending on their purpose. For this reason, this study defined a mathematical model describing the flow inside a coupled structure (cylindrical tube–rectangular channel). Due to the mass conservation principle, the flows passing through two coupled geometries are equivalent. This equivalency can be expressed as:

$$Q = Q_t \rightarrow \omega b \dot{h} = \pi r^2 v_t \quad \text{(A9)}$$

where ω and b are the width and height of the channel, respectively; and v_t is the velocity inside the tubing.

From Equation (A9), the velocity inside the tubing can be written as:

$$v_t = \frac{\dot{h}\omega b}{\pi r^2} \quad \text{(A10)}$$

Appendix A.2. Pressure Drop Inside a Microfluidic System

In a closed system composed of a pressure source, a fluid reservoir, and the coupling of tubing with a microchannel of rectangular cross-section (geometries illustrated in

Figure A1a,b), the pressure inside the rectangular microchannel, ΔP, is the summation of all the pressures in the system, as shown in Figure 3, is expressed in Equation (A11):

$$\Delta P = P_p + P_H - \Delta P_t - P_{cap} \quad (A11)$$

where P_p indicates the values set for the pumping source, ΔP_t is the pressure drop due to the coupled tubing, P_H is the hydrostatic pressure, and P_{cap} is the capillary pressure. All these concepts are introduced below.

The hydrostatic pressure, P_H is the one that originates from the fluid height (the difference between the fluid reservoir height and the measurement site height). It can be calculated by multiplying the fluid height inside the reservoir relative to the microfluidic channel, density of the fluid, and gravity: $P_H = \rho g H$.

Capillary pressure, P_{cap}, is defined as the resistance of the hydrophobic channel walls to the fluid advancement. P_{cap} is dependent on the contact angle and the surface tension of the fluid, τ (which is dependent on temperature). Considering the geometrical parameters of a rectangular section channel, with height b and width ω, as shown in Figure A2, P_{cap} can be deduced.

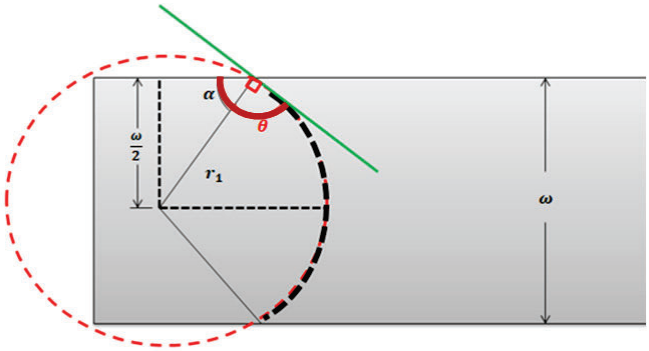

Figure A2. Top view of the contact angle of a fluid–air interface inside a microfluidic channel of width ω and height b.

With the fluid front in Figure A2 expressed in terms of two radii: r_1, shown in the top view, and r_2, the lateral view counterpart, we get:

$$P_{cap} = \tau\left(\frac{1}{r_1} + \frac{1}{r_2}\right) \quad (A12)$$

This is needed to determine the value of the curvature radii, r_1 and r_2. Following the geometrical representation of the rectangular cross-section channel in Figure A2, the tangent curve to the radius on a circumference has an angle of 90°, and the contact angle of the front can be written as:

$$\theta = 90^\circ + \alpha \quad (A13)$$

Then:

$$\frac{\omega}{2} = r_1 \sin\alpha \quad (A14)$$

$$\frac{\omega}{2} = r_1 \sin\left(\theta - 90^\circ\right) \quad (A15)$$

$$\frac{\omega}{2} = r_1(\sin\theta \cos 90^\circ - \sin 90^\circ \cos\theta) \quad (A16)$$

$$\frac{\omega}{2} = -r_1 \cos\theta \quad (A17)$$

Considering the geometrical parameters of a rectangular section channel, with height b and width ω, r_1 can be written as:

$$r_1 = -\frac{\omega}{2\cos\theta} \tag{A18}$$

Since the contact angle on the side of the surface is also θ, and using the same trigonometric as before, r_2 is:

$$r_2 = -\frac{b}{2\cos\theta} \tag{A19}$$

Finally, replacing r_1 and r_2 in Equation (A12), capillary pressure can be calculated using:

$$P_{cap} = -2\tau\cos\theta\left(\frac{1}{b} + \frac{1}{\omega}\right) \tag{A20}$$

The value of capillarity is always positive, since the surface is hydrophobic, and the contact angle is always θ = π/2+α.

The term ΔP can be also understood as the product of the hydraulic resistance inside the microchannel, S (dependent on *m*, *n* and the channel geometric parameters ω and b) and the channel flow, Q. Using Equation (A8), ΔP is:

$$\Delta P = SQ^n = mh(t)\frac{1}{(2\omega)^n}\left(\frac{2}{b}\right)^{1+2n}\left(\frac{1}{n}+2\right)^n Q^n \tag{A21}$$

Considering the flow dependence on front velocity $\left(Q = \dot{h}\omega b\right)$:

$$\Delta P = mh(t)\left(\frac{2}{b}\right)^{1+n}\left(\frac{1}{n}+2\right)^n \dot{h}^n \tag{A22}$$

ΔP_t, similarly to ΔP, can be expressed as the product of S_t and ${Q_t}^n$. S_t is the hydraulic resistance represented by the tubing; it depends on *m*, *n*, and the tubing parameters r, l_t. Q_t is the flow inside the tubing:

$$\Delta P_t = S_t {Q_t}^n = m2l_t\left(\frac{1}{\pi r^2}\right)^n\left(\frac{1}{r^{1+n}}\right)\left(\frac{1}{n}+3\right)^n {Q_t}^n \tag{A23}$$

Taking into account the flow dependence on flow velocity inside the tube $\left(Q_t = \pi r^2 v_t\right)$ and the relation seen in Equation (A10), for the coupled system in this study, ΔP_t can be written as follows in Equation (A24). Due to mass conservation inside the coupled system as shown in Figure 5, ΔP_t depends on *m*, *n*, the tubing, and the microchannel parameters:

$$\Delta P_t = m2l_t\left(\frac{\omega b}{\pi r^2}\right)^n\left(\frac{1}{r^{1+n}}\right)\left(\frac{1}{n}+3\right)^n \dot{h}^n \tag{A24}$$

According to mass conservation, and taking Equation (A21) and Equation (A23) into account, an effective pressure (P_{eff}) defined as the pressure drop caused by the pumping system, the capillary pressure, and the hydrostatic pressure into the whole system can be determined by:

$$\begin{aligned} P_{eff} &= P_p + P_H - P_{cap} \\ &= \Delta P_t + \Delta P = m\left[2l_t\left(\tfrac{\omega b}{\pi r^2}\right)^n\left(\tfrac{1}{r^{1+n}}\right)\left(\tfrac{1}{n}+3\right)^n + h(t)\left(\tfrac{2}{b}\right)^{1+n}\left(\tfrac{1}{n}+2\right)^n\right]\dot{h}^n \end{aligned} \tag{A25}$$

Moreover, Equation (A25) allows for the evaluation of the case in which one of the main terms (relative to the coupled structures of the tubing and microchannel) is much

larger than the other (relative to the microchannel only). P_{eff} is constant and not time-dependent. Then, when the relation in Equation (A26) is satisfied,

$$2l_t\left(\frac{\omega b}{\pi r^2}\right)^n\left(\frac{1}{r^{1+n}}\right)\left(\frac{1}{n}+3\right)^n \gg h(t)\left(\frac{2}{b}\right)^{1+n}\left(\frac{1}{n}+2\right)^n \quad (A26)$$

The term on the right side can be neglected and the expression for P_{eff} is no longer dependent on time (t). Now, Equation (A25) can be simplified to:

$$P_{eff} = m2l_t\left(\frac{\omega b}{\pi r^2}\right)^n\left(\frac{1}{r^{1+n}}\right)\left(\frac{1}{n}+3\right)^n \dot{h}^n = m2l_t\left(\frac{\omega b^2}{\pi r^2}\right)^n\left(\frac{1}{r^{1+n}}\right)\left(\frac{1}{n}+3\right)^n \dot{\gamma}^n \quad (A27)$$

$\dot{\gamma}$ was described in Equation (1) as the ratio between the mean front velocity, $\dot{h}$, and channel height, b.

All the independent variables can now be expressed in the form of a constant K, defined as:

$$K(m,n) = m2l_t\left(\frac{\omega b^2}{\pi r^2}\right)^n\left(\frac{1}{r^{1+n}}\right)\left(\frac{1}{n}+3\right)^n \quad (A28)$$

This depends on the fluid properties (m and n) and geometrical parameters of the system. Now, Equation (A27) can be written as follows, where K depends on the geometrical properties of the setup and the fluid viscosity value:

$$P_{eff} = K(m,n)\dot{\gamma}^n \quad (A29)$$

Appendix A.3. Newtonian Fluids

For the case of Newtonian fluids $(n = 1)$, Equation (A22) and Equation (A24) from Appendix A.2 are simplified to:

$$\Delta P_t(n=1) = m\frac{8\omega b l_t}{\pi r^4}\dot{h} \quad (A30)$$

$$\Delta P(n=1) = m\frac{12h(t)}{b^2}\dot{h} \quad (A31)$$

Due to mass conservation, the pressure for the entire system can be described (as it was in Equation (A25)) as follows:

$$P_{eff}(n=1) = m\left(\frac{8\omega b l_t}{\pi r^4} + \frac{12h(t)}{b^2}\right)\dot{h} \quad (A32)$$

As evaluated in the non-Newtonian case, Equation (A32) allows evaluating when the term relative to the coupled geometry is much larger than the term that only depends on the microchannel, $\frac{8\omega b l_t}{\pi r^4} \gg \frac{12h(t)}{b^2}$; then, the time dependence of the equation also can be neglected in the case of the Newtonian fluids. This allows for Equation (A32) to be expressed as:

$$P_{eff}(n=1) = m\frac{8\omega b l_t}{\pi r^4}\dot{h} = m\frac{8\omega b^2 l_t}{\pi r^4}\dot{\gamma} \quad (A33)$$

Just as before, and now for the Newtonian case, K can be expressed in terms of the geometry of the system and the experimentally obtained front velocity:

$$K(m,n=1) = m\frac{8\omega b^2 l_t}{\pi r^4} \quad (A34)$$

The relation between the pressure and the mean front velocity follows a linear behavior. The equivalent expression for Equation (A29) for Newtonian fluids is:

$$P_{eff}(m, n = 1) = K(m, n = 1)\dot{\gamma} \quad \text{(A35)}$$

Appendix B. Viscosity Data

Fluid	Temperature(°C)	Viscosity η (m × Pas)	Reference
MGVS60	24	6.00	[Paragon Scientific, Ltd.]
Blood plasma	20	1.50–1.81	[Baskurt, 2007] [36]
Water	20	1.002	[Bruus, 2008] [35]
Blood at 44% Ht	22	9–10 at (1 s^{-1})	[Thurston and Henderson, 2006] [40]

References

1. Gupta, S.; Wang, W.S.; Vanapalli, S.A. Microfluidic viscometers for shear rheology of complex fluids and biofluids. *Biomicrofluidics* **2016**, *10*, 043402. [CrossRef] [PubMed]
2. Merrill, E.W.; Gilliand, E.R.; Cokelet, G.; Shin, H.; Britten, A.; Wells, R.E. Rheology of human blood, near and at zero flow. Effects of temperature and hematocrit level. *Biophys. J.* **1963**, *3*, 199–213. [CrossRef]
3. Merrill, E.W. Rheology of blood. *Physiol. Rev.* **1969**, *49*, 863–888. [CrossRef] [PubMed]
4. Chien, S.; Usami, S.; Bertles, J.F. Abnormal rheology of oxygenated blood in sickle cell anemia. *J. Clin. Investig.* **1970**, *49*, 623–634. [CrossRef] [PubMed]
5. Thurston, G.B. Rheological parameters for the viscosity viscoelasticity and thixotropy of blood. *Biorheology* **1979**, *16*, 149–162. [CrossRef]
6. Wells, R.; Schmid-Schönbein, H. Red cell deformation and fluidity of concentrated cell suspensions. *J. Appl. Physiol.* **1969**, *27*, 213–217. [CrossRef]
7. Rosencranz, R.; Bogen, S.A. Clinical Laboratory Measurement of Serum, Plasma, and Blood Viscosity. *Pathol. Patterns Rev.* **2006**, *125*, S78–S86. [CrossRef]
8. Tropea, C. *Springer Handbook of Experimental Fluid Mechanics*; Springer: Berlin/Heidelberg, Germany, 2007.
9. Fåhræus, R.; Lindqvist, T. The Viscosity of The Blood in Narrow Capillary Tubes. *Am. J. Physiol. Content* **1931**, *96*, 562–568. [CrossRef]
10. Lázaro, G.R.; Hernández-Machado, A.; Pagonabarraga, I. Rheology of red blood cells under flow in highly confined microchannels. II. Effect of focusing and confinement. *Soft Matter* **2014**, *10*, 7207–7217. [CrossRef]
11. Lázaro, G.R.; Hernández-Machado, A.; Pagonabarraga, I. Collective behavior of red blood cells in confined channels. *Eur. Phys. J. E* **2019**, *42*. [CrossRef]
12. Doy, N.; McHale, G.; Newton, M.I.; Hardacre, C.; Ge, R.; MacInnes, J.M.; Kuvshinov, D.; Allen, R.W. Small volume laboratory on a chip measurements incorporating the quartz crystal microbalance to measure the viscosity-density product of room temperature ionic liquids. *Biomicrofluidics* **2010**, *4*, 014107. [CrossRef] [PubMed]
13. Oba, T.; Kido, Y.; Nagasaka, Y. Development of laser-induced capillary wave method for viscosity measurement using pulsed carbon dioxide laser. *Int. J. Thermophys.* **2004**, *25*, 1461–1474. [CrossRef]
14. Pipe, C.J.; Majmudar, T.S.; McKinley, G.H. High shear rate viscometry. *Rheol. Acta* **2008**, *47*, 621–642. [CrossRef]
15. Choi, S.; Park, J.K. Microfluidic rheometer for characterization of protein unfolding and aggregation in microflows. *Small* **2010**, *6*, 1306–1310. [CrossRef] [PubMed]
16. Kang, Y.; Yeom, E.; Lee, S.J. A microfluidic device for simultaneous measurement of viscosity and flow rate of blood in a complex fluidic network. *Biomicrofluidics* **2013**, *7*. [CrossRef]
17. Chevalier, J.; Ayela, F. Microfluidic on chip viscometers. *Rev. Sci. Instrum.* **2008**, *79*. [CrossRef] [PubMed]
18. Clasen, C.; Gearing, B.P.; McKinley, G.H. The flexure-based microgap rheometer (FMR). *J. Rheol.* **2006**, *50*, 883–905. [CrossRef]
19. Lee, T.A.; Liao, W.H.; Wu, Y.F.; Chen, Y.L.; Tung, Y.C. Electrofluidic Circuit-Based Microfluidic Viscometer for Analysis of Newtonian and Non-Newtonian Liquids under Different Temperatures. *Anal. Chem.* **2018**, *90*, 2317–2325. [CrossRef]
20. Del Giudice, F. Simultaneous measurement of rheological properties in a microfluidic rheometer. *Phys. Fluids* **2020**, *32*, 052001. [CrossRef]
21. Solomon, D.E.; Abdel-Raziq, A.; Vanapalli, S.A. A stress-controlled microfluidic shear viscometer based on smartphone imaging. *Rheol. Acta* **2016**, *55*, 727–738. [CrossRef]
22. Srivastava, N.; Burns, M.A. Analysis of non-Newtonian liquids using a microfluidic capillary viscometer. *Anal. Chem.* **2006**, *78*, 1690–1696. [CrossRef]
23. Jackson, G.N.B.; Ashpole, K.J.; Yentis, S.M. The TEG®vs the ROTEM®thromboelastography/thromboelastometry systems. *Anaesthesia* **2009**, *64*, 212–215. [CrossRef]
24. Thakur, M.; Ahmed, A.B. A review of thromboelastography. *Int. J. Perioper. Ultrasound Appl. Technol.* **2012**, *1*, 25–29. [CrossRef]

25. Bandey, H.L.; Cernosek, R.W.; Lee, W.E.; Ondrovic, L.E. Blood rheological characterization using the thickness-shear mode resonator. *Biosens. Bioelectron.* **2004**, *19*, 1657–1665. [CrossRef] [PubMed]
26. Kang, Y.J.; Yoon, S.Y.; Lee, K.H.; Yang, S. A highly accurate and consistent microfluidic viscometer for continuous blood viscosity measurement. *Artif. Organs* **2010**, *34*, 944–949. [CrossRef] [PubMed]
27. Yilmaz, F.; Gundogdu, M. A critical review on blood flow in large arteries; relevance to blood rheology, viscosity models, and physiologic conditions. *Korea-Aust. Rheol. J.* **2008**, *20*, 197–211.
28. Trejo-Soto, C.; Costa-Miracle, E.; Rodriguez-Villarreal, I.; Cid, J.; Castro, M.; Alarcon, T.; Hernandez-Machado, A. Front microrheology of the non-Newtonian behaviour of blood: Scaling theory of erythrocyte aggregation by aging. *Soft Matter* **2017**, *13*, 3042–3047. [CrossRef] [PubMed]
29. Diez-Silva, M.; Dao, M.; Han, J.; Lim, C.T.; Suresh, S. Shape and biomechanics characteristics of human red blood cells in health and disease. *MRS Bull.* **2010**, *35*, 382–388. [CrossRef] [PubMed]
30. Apostolidis, A.J.; Moyer, A.P.; Beris, A.N. Non-Newtonian effects in simulations of coronary arterial blood flow. *J. Nonnewton. Fluid Mech.* **2016**, *233*, 155–165. [CrossRef]
31. Van Kempen, T.H.S.; Peters, G.W.M.; Van De Vosse, F.N.; Van Kempen, T.H.S.; Van De Vosse, F.N.; Peters, G.W.M. A constitutive model for the time-dependent, nonlinear stress response of fibrin networks. *Biomech. Model. Mechanobiol.* **2015**, *14*, 995–1006. [CrossRef]
32. Armstrong, M.; Horner, J.; Clark, M.; Deegan, M.; Hill, T.; Keith, C.; Mooradian, L. Evaluating rheological models for human blood using steady state, transient, and oscillatory shear predictions. *Rheol. Acta* **2018**, *57*, 705–728. [CrossRef]
33. Ramaswamy, B.; Yeh, Y.T.T.; Zheng, S.Y. Microfluidic device and system for point-of-care blood coagulation measurement based on electrical impedance sensing. *Sens. Actuators B Chem.* **2013**, *180*, 21–27. [CrossRef]
34. Trejo-Soto, C.; Costa-Miracle, E.; Rodriguez-Villarreal, I.; Cid, J.; Alarcón, T.; Hernández-Machado, A. Capillary filling at the microscale: Control of fluid front using geometry. *PLoS ONE* **2016**, *11*. [CrossRef]
35. Bruus, H. *Theoretical Microfluidics*; Oxford University Press: Oxford, UK, 2006.
36. Baskurt, O. *Handbook of Hemorheology and Hemodynamics*; IoS Press: Amsterdam, The Neetherlands, 2007.
37. Adamson, A.W.; Gast, A.P.; Wiley, J. *Physical Chemistry of Surfaces*, 6th ed.; Interscience Publishers: New York, NY, USA, 1967.
38. Murillo, C. *Fisicoquímica*, 5th ed.; Levine, I.N., Ed.; McGraw Hill: Madrid, Spain, 2004; Volume 2.
39. Bruus, H. *Understanding Rheology*; Oxford University Press: New York, NY, USA, 2008.
40. Thurston, G.B.; Henderson, N.M. Effects of flow geometry on blood viscoelasticity. *Biorheology* **2006**, *43*, 729–746. [PubMed]
41. Colomer, J.; Hernández-Machado, A.; Alarcón Cor, T. Method and Apparatus for Measuring Rheological Properties of Newtonian and Non-Newtonian Fluids. International Patent EP3093647A1, 17 November 2016.
42. Guyon, E.; Hulin, J.-P.; Petit, L.; Mitescu, C.D. *Physical Hydrodynamics*, 2nd ed.; Oxford University Press: Oxford, UK, 2015.

b. Hemorheology and diseases that affect the red blood cell.

Article II: Blood Rheological Characterization of β-Thalassemia Trait and Iron Deficiency Anemia Using Front Microrheometry

Authors: L. Méndez-Mora, M. Cabello-Fusarés, J. Ferré-Torres, C. Riera-Llobet, E. Krishnevskaya, C. Trejo-Soto, S. Payán-Pernía, I. Hernández-Rodríguez, C. Morales-Indiano, T. Alarcón, J.-L. Vives-Corrons, A. Hernandez-Machado

Journal: Frontiers of Physiology

Year: 2021

Volume and Issue: 12

Doi: 10.3389/fphys.2021.761411

Impact Factor: 4,0

Quartile: Q1

Citations: 6

Blood is a non-Newtonian fluid of the shear thinning type. Its viscosity decreases as the pressure applied onto it increases. The viscosity of blood is highly affected by the shape and size of red blood cells (RBCs), hemoglobin (Hb) content, membrane rigidity and hematocrit concentration. Diseases that alter the RBC conditions have the potential of affecting the viscosity of whole blood samples. For this reason, this work focuses on the development method for the detection of differences in the viscosity of blood between samples from patients with beta-thalassemia traits (β-TT), iron deficiency anemia (IDA) and blood from healthy donors nondependent on the hematocrit level of each sample. The viscosity is calculated as a function of the mean front velocity by detecting the sample fluid-air interface advancing through a microfluidic channel. The main contribution of this research is establishing the

basis of a point-of-care device for the rapid and cost-effective detection of β-TT without the need of big and complex equipment and the use of reactants.

The first part of the study consists in the normalization of healthy and non-healthy blood samples. This is done to remove the effects of hematocrit differences on the viscosity value obtained for each one. To do this, we employ a mathematical model that relates the viscosity of a blood samples to the viscosity of its plasma [84]. By taking one healthy sample and separating it into three hematocrits, we can test how the model can be used to calculate a unique curve characteristic of the blood samples in study. We repeat the same for one β-TT sample. The effects caused by the hematocrit are removed, so the viscosity changes observed can be attributed to variations in the RBC caused by the disease state.

Next, we apply the same procedure to β-TT, IDA and healthy samples. This results in samples that appear to show in group differences despite not having the effects of hematocrit. At this point we introduce the Median Corpuscular Volume (MCV) of the red blood cell. We noticed that a smaller MCV accounted for a bigger viscosity when compared to samples with the same condition. With this classification, we compare the three groups of MCV present in the β-TT samples. Following this, we compare the β-TT samples to IDA samples with the same MCV, to confirm if the effects that we observed in viscosity are caused only by microcytosis. The results showed that when compared, the β-TT and IDA samples.

Because the samples are of different hematocrit, the value of the viscosity with respect to the plasma of each one is normalized. The effective viscosity is calculated, making a relationship between the pressure slope (plasma velocity of each sample; Newtonian relationship and η_{eff} therefore constant slope) and the point-to-point slope of the sample to be normalized (which will be non-Newtonian):

$$\eta_{eff} = \frac{\dot{h}_{plasma} \Delta P_{muestra}}{\dot{h}_{muestra} \Delta P_{plasma}}$$

The hematocrit-normalized viscosity of each sample is then calculated with respect to the highest hematocrit.

$$\eta_{htc} = 1 + (\eta_{eff} - 1)\frac{\phi_{max}}{\phi_{muestra}}$$

Where is the maximum hematocrit with respect to which you want to normalize, is the hematocrit of the sample to be normalized.

To determine the *bending number*, an energy deformability ratio of the red blood cells of each sample is made. For this, values of *shear rates* and viscosity of plasma corresponding to the points where the value of the viscosity differs to the minimum are related. The energy difference of two samples is obtained using:

$$\frac{E_{0A}}{E_{0B}} = \frac{\eta_{pA}\dot{\gamma}_A}{\eta_{pB}\dot{\gamma}_B}$$

Once the energy ratio is calculated, the shear rate of the samples is multiplied and rescaled so that the viscosity normalized by hematocrit of each sample can be drawn as a band of minimum and maximum for beta-thalassemia, regardless of hematocrit and donor.

In this article, we used the hematocrit normalization technique by Trejo et al.,[84]. This allowed us to obtain a single viscosity range for healthy donors. Using the same method, a normalized viscosity curve of beta-thalassemia is calculated. The hematocrit normalized viscosity does not show the effects of hematocrit levels on the blood viscosity. Therefore, is a useful method to perform comparisons between samples from the same or different patients, both in healthy and non-healthy conditions, independent of their hct (%). Thanks to this method, we obtained curves with clearly differentiated parameters for healthy blood, β-TT, and IDA in Figure 29.

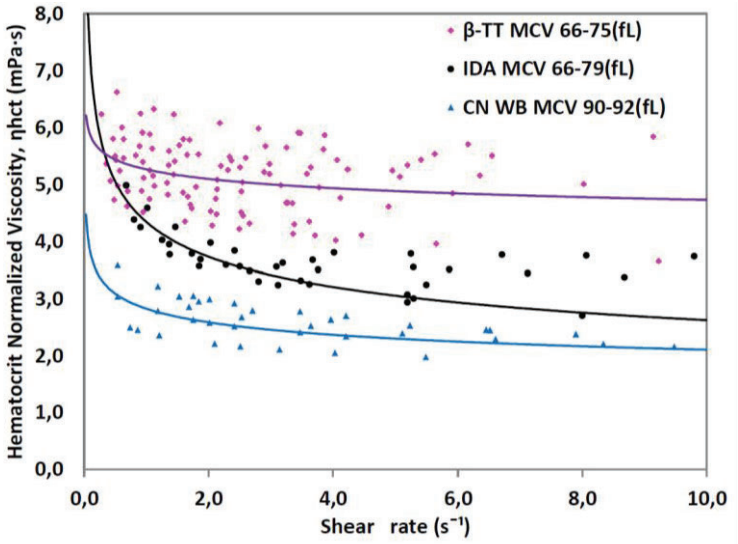

Figure 29. Hematocrit normalized viscosity for ten samples of b-TT, five samples of IDA and five samples from healthy donors (CN). Whole blood in all cases.

The results show that the MCV seems to affect the viscosity of the samples. Samples with distinct MCV did not follow the normalized curve path. Once the samples were segregated into three groups based on their MCV, a clear pattern showed up. As a general observation, lower MCV accounted for higher viscosity values. For this motive, it is reasonable to make a comparison between β -TT and IDA samples with similar MCV only. It was found, however, that even at comparable MCV and after hematocrit normalization, β-TT has a higher viscosity than both IDA and control samples. This difference in viscosity might be caused by differences in the affected deformation capability of RBCs and the membrane changes caused by the a chains disorders that characterize β-TT [85].

frontiers in Physiology

ORIGINAL RESEARCH
published: 21 October 2021
doi: 10.3389/fphys.2021.761411

Blood Rheological Characterization of β-Thalassemia Trait and Iron Deficiency Anemia Using Front Microrheometry

Lourdes Méndez-Mora[1], Maria Cabello-Fusarés[2], Josep Ferré-Torres[1], Carla Riera-Llobet[1], Elena Krishnevskaya[3], Claudia Trejo-Soto[4], Salvador Payán-Pernía[5], Inés Hernández-Rodríguez[6], Cristian Morales-Indiano[7], Tomas Alarcón[2,8,9], Joan-Lluis Vives-Corrons[3] and Aurora Hernandez-Machado[1,2,10]*

[1] Department of Condensed Matter Physics, University of Barcelona, Barcelona, Spain, [2] Centre de Recerca Matemàtica, Barcelona, Spain, [3] Red Cell Pathology and Hematopoietic Disorders (Rare Anemias) Unit, Josep Carreras Leukaemia Research Institute, Badalona, Spain, [4] Instituto de Física, Pontificia Universidad Católica de Valparaiso, Valparaiso, Chile, [5] Red Blood Cell Disorders Unit, Hematology Department, Hospital Universitario Virgen del Rocío, Instituto de Biomedicina de Sevilla (IBIS/CSIC), Seville, Spain, [6] Hematology Service, Institut Català d'Oncologia, Germans Trias i Pujol University Hospital, Badalona, Spain, [7] Laboratory Medicine Department, Laboratori Clínic Metropolitana Nord, Hospital Universitari Germans Trias i Pujol, Badalona, Spain, [8] Institució Catalana de Recerca i Estudis Avançats, Barcelona, Spain, [9] Departament de Matemàtiques, Universitat Autónoma de Barcelona, Bellaterra, Spain, [10] Institute of Nanoscience and Nanotechnology, University of Barcelona, Barcelona, Spain

The purpose of this work is to develop a hematocrit-independent method for the detection of beta-thalassemia trait (β-TT) and iron deficiency anemia (IDA), through the rheological characterization of whole blood samples from different donors. The results obtained herein are the basis for the development of a front microrheometry point-of-care device for the diagnosis and clinical follow-up of β-TT patients suffering hematological diseases and alterations in the morphology of the red blood cell (RBC). The viscosity is calculated as a function of the mean front velocity by detecting the sample fluid-air interface advancing through a microfluidic channel. Different viscosity curves are obtained for healthy donors, β-TT and IDA samples. A mathematical model is introduced to compare samples of distinct hematocrit, classifying the viscosity curve patterns with respect to the health condition of blood. The viscosity of the fluid at certain shear rate values varies depending on several RBC factors such as shape and size, hemoglobin (Hb) content, membrane rigidity and hematocrit concentration. Blood and plasma from healthy donors are used as reference. To validate their potential clinical value as a diagnostic tool, the viscosity results are compared to those obtained by the gold-standard method for RBC deformability evaluation, the Laser-Optical Rotational Red Cell Analyzer (LoRRCA).

Keywords: beta-thalassemia trait, iron deficiency (anemia), anemia, hemorheology, rheology, microfluidics, blood rheology, microrheometer

OPEN ACCESS

Edited by:
Paola Bianchi,
IRCCS Ca' Granda Foundation Maggiore Policlinico Hospital, Italy

Reviewed by:
Pedro Moura,
Karolinska Institutet (KI), Sweden
Giovanna Tomaiuolo,
University of Naples Federico II, Italy

****Correspondence:***
Lourdes Méndez-Mora
lmendemo9@alumnes.ub.edu

Specialty section:
This article was submitted to Red Blood Cell Physiology, a section of the journal Frontiers in Physiology

Received: *19 August 2021*
Accepted: *30 September 2021*
Published: *21 October 2021*

Citation:
Méndez-Mora L, Cabello-Fusarés M, Ferré-Torres J, Riera-Llobet C, Krishnevskaya E, Trejo-Soto C, Payán-Pernía S, Hernández-Rodríguez I, Morales-Indiano C, Alarcón T, Vives-Corrons J-L and Hernandez-Machado A (2021) Blood Rheological Characterization of β-Thalassemia Trait and Iron Deficiency Anemia Using Front Microrheometry. Front. Physiol. 12:761411. doi: 10.3389/fphys.2021.761411

INTRODUCTION

Blood is a biological fluid composed of red blood cells (RBCs), white blood cells (WBC), and platelets suspended in plasma, a Newtonian fluid containing organic molecules, proteins and salts (Baskurt and Meiselman, 2003). The viscosity of plasma is constant; it does not depend on the pressure that is applied onto it (Késmárky et al., 2008). Whole blood is a non-Newtonian shear-thinning fluid, and its viscosity decreases when an increasing pressure is applied. WBCs and platelets can affect blood rheology but, under normal conditions, RBCs represent most of the cellular components and make the biggest contribution to viscosity (Pop et al., 2002). As a result, the viscosity of blood depends mostly on the ability of RBCs to deform under circulation flow (Baskurt and Meiselman, 2003; Cokelet and Meiselman, 2007; Mehri et al., 2018).

Red blood cells have a characteristic discoid shape with a biconcave profile, under normal physiological conditions; the well-known discocyte shape (Diez-Silva et al., 2010). This shape combines a large area to volume ratio, which is an important factor to maximize oxygen diffusion. The erythrocytes have a unique ability to deform and pass through small capillaries before rapidly recovering their initial shape. The deformation capacity of RBCs is mainly due to three factors; their large area to volume ratio; the viscosity of the intracellular fluid that is dominated by the presence of hemoglobin and the viscoelastic properties of the cell membrane (Lázaro et al., 2013; Tomaiuolo, 2014). However, the deformability of RBCs is impaired in some pathological conditions as a result of defects in cell membrane skeletal architecture (Faustino et al., 2019; Hymel et al., 2020), erythrocyte aging (Diez-Silva et al., 2010; Simmonds et al., 2013), and mechanical damage (Rico et al., 2018).

β-thalassemia syndromes are a heterogeneous group of genetic conditions characterized by reduced or abolished synthesis of the hemoglobin subunit beta (hemoglobin beta chain). The β-thalassemia carrier state is also referred as heterozygous β-thalassemia or β-thalassemia trait (β-TT) (Galanello and Origa, 2010). When β-TT is present, RBCs show rheological abnormalities (Berga et al., 1989). The RBC membrane can be affected due to a selective interaction between the α-chain excess and the erythrocyte membrane cytoskeleton (Rachmilewitz and Kahane, 1980), while other alterations are caused by hemoglobin denaturalization (Fiorelli et al., 1996). In addition, microcytosis, or decreased mean corpuscular volume (MCV) of RBCs, is present in β-TT carriers. Previous works suggest that the decreased RBC deformability is probably due to microcytosis (Rasia et al., 1986; Iborra et al., 2003). More recently, by comparing two non-healthy sets of samples, of iron deficiency anemia (IDA) (DeLoughery, 2017) and β-thalassemia trait, a study based on ektacytometry showed two distinct deformation patterns, indicating that the observed decrease in the deformability is not only due to microcytosis (Payán-Pernía et al., 2021). Osmotic gradient ektacytometry measures RBC deformability under defined shear stress as a function of suspending medium osmolarity (Llaudet-Planas et al., 2018). IDA and β-TT are two very common causes of microcytic hypochromic anemia in the Mediterranean region (Galanello and Origa, 2010).

Alterations in the deformation capacity of RBCs can produce changes in the non-linear rheological behavior of the whole blood; these alterations are potentially detectable via a rheometry study. Rheological measurements are usually performed with rotational rheometers, a type of shear rheometer (Macosko, 1994). However, this type of equipment is expensive, requires a considerable laboratory space and must be operated by trained personnel. Moreover, the measurements take several minutes and need a large sample amount. For these reasons, there is a demand for Point-of-care (PoC) devices for analyzing the rheological properties of whole blood. To be efficient and cost-effective, many portable PoC devices employ microfluidic devices that generally consist of low-cost microfluidic chips, that are easy to fabricate and are made of glass, polydimethylsiloxane (PDMS) and other polymeric materials that are biocompatible and widely available.

The microfluidic approach permits to obtain a high precision measurement of blood conditions in motion with only one drop of blood, in a time and cost-effective way in comparison to rotational rheometers (Davies and Stokes, 2008; Pipe and McKinley, 2009; Choi and Park, 2010; Galindo-Rosales et al., 2012). Many applications that aim at analyzing the properties of the blood through its rheological characterization, employ microfluidic devices that measure the behavior of blood as a function of the shear rate (Srivastava and Burns, 2006; Fedosov et al., 2011; Tomaiuolo, 2014; Rico et al., 2018; Rodriguez-Villarreal et al., 2020). In addition, some microfluidic applications permit the observation of the flow of blood under high confinement conditions (Davies and Stokes, 2008; Bartolo and Aarts, 2012; Lázaro et al., 2014). PoC diagnostics, including microfluidic tools, are very promising for early detection of different diseases, and for the monitoring of health conditions.

In this work, a PoC front-microrheometer with electronic detection is used to characterize blood samples from different donors. The viscosity value as a function of the shear rate of the blood front is measured, details on the mathematical model developed can be found in previous works (Trejo-Soto et al., 2017, Trejo-Soto et al., 2018; Méndez-Mora et al., 2021). Three types of samples are analyzed: control samples from healthy donors, and blood samples from IDA and β-TT patients. Due to the morphological and membrane differences of the RBCs in the three groups, it is expected to obtain a distinctive viscosity pattern for each group. As it is expected that RBCs volume has an impact on blood viscosity, and the microcytosis is present in IDA and β-TT blood donors, the samples are classified in terms of the MVC of their RBCs, ensuring that microcytosis does not mask other rheological effects.

The main purpose of this study is to demonstrate that the micro-rheometer developed can differentiate distinct hematological pathologies, regardless their hematocrit percentage. This is done by the differentiation, through whole-blood viscosity, between two very common conditions that affect RBCs, IDA, and β-TT, beyond the effect of the low MCV that characterizes both of them, and after hematocrit normalization. The research represents and advancement in the development of PoC devices for the diagnosis of anemia-related

diseases. This is of global concern, since information about the precise world distribution and frequency of the inherited and acquired hemoglobin disorders is still limited (Williams and Weatherall, 2012). It is also an issue of particular interest in the developing countries, where anemia is more prevalent (Kassebaum et al., 2016).

MATERIALS AND METHODS

Mathematical Model

The method used here to analyze the fluid flow consists of the study of the fluid-air interface advancement. Inside a microfluidic channel, the front velocity $\dot{h}$, is the change in position of the fluid, $h(t)$ through time along the microfluidic channel. The term $h(t)$ is the average position of the front $h(t) = \frac{1}{N}\sum_{j=1}^{N} h_j(t)$, where $h_j(t)$ is the fluid front position. Shear rate, $\dot{\gamma}$ is the normalization of mean front velocity ($\dot{h}$) according to the depth of the microchannel, b:

$$\dot{\gamma} = \frac{\dot{h}}{b} \tag{1}$$

According to the Ostwald-De Waele Power-Law model for fluids, the viscosity can be expressed as a function of shear rate:

$$\eta(\gamma) = m\dot{\gamma}^{n-1} \tag{2}$$

where m is a prefactor obtained experimentally, n is a constant that depends on the studied fluid and defines the nature of its viscosity, being n = 1 for Newtonian fluids. To remove the effects on viscosity caused by distinct hematocrit levels in different samples, the first step is to calculate the effective viscosity, (η_{eff}). This is the viscosity of blood relative to the viscosity of plasma. It consists of establishing a relation between the pressure versus shear rate fit for plasma and the sample that needs to be normalized (Trejo-Soto and Hernández-Machado, 2021). This is expressed as follows:

$$\eta_{eff} = \frac{\dot{\gamma}_{Plasma}\Delta P_{Sample}}{\dot{\gamma}_{Sample}\Delta P_{Plasma}} \tag{3}$$

where ΔP_{Sample} and ΔP_{Plasma} are the pressure inside the microfluidic system for the blood sample and its plasma, respectively. Analogously, $\dot{\gamma}_{Sample}$ and $\dot{\gamma}_{Plasma}$ are the shear rates of the blood and plasma samples, respectively. Finally, (η_{eff}) is normalized with respect to the maximum hematocrit level of the studied samples. The hematocrit normalized viscosity (η_{hct}), is calculated using the following equation:

$$\eta_{hct} = 1 + \left(\eta_{eff} - 1\right)\frac{\phi_{max}}{\phi_{sample}} \tag{4}$$

where ϕ_{max} is the maximum hematocrit with respect to which the different samples need to be normalized. ϕ_{sample} is the hematocrit of the sample being normalized.

Experimental Method

The experimental setup used consists of a microfluidic channel with 24 gold electrodes, a pumping source, and a computer terminal (Méndez-Mora et al., 2021). A series of shear rates is obtained by applying a set of pressures on the sample fluid. The fluid front advancement is detected in a fast and accurate manner by the gold electrodes printed beneath the microfluidic channel. The microfluidic chips made of polydimethylsiloxane (PDMS) attached to glass substrates by oxygen plasma bonding. The microfluidic channel and the electrodes have been fabricated

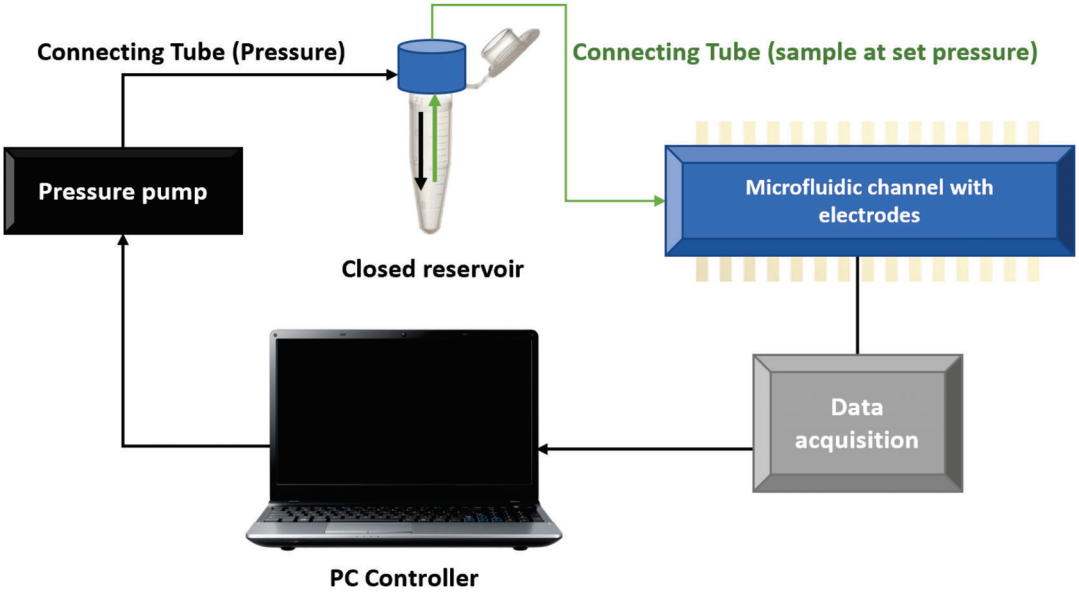

FIGURE 1 | Schematics of the microfluidic setup. A micropump is used as a pressure source. The pump is connected to the reservoir with the fluid sample using a tube. The fluid is flowing through the microchannel. The microfluidic consumable is made of PDMS sealed on a glass substrate with electrodes.

using lithography techniques (Qin et al., 2010). The distance between electrodes is 350 μm. There are four groups of electrodes, and each has six pairs of electrodes. The distance between each group of electrodes is 8.5 mm. The channel width is $\omega = 1000$ μm height $b = 300$ μm and the length from inlet to outlet is $l_c = 4$ cm. PDMS, glass, and Tygon tubes are biocompatible.

Using a tube of an internal diameter of 254 μm and length 20 cm the pump is connected to a closed reservoir holding the fluid, and this communicates the reservoir with the microchannel. The pump is easy to control through the computer, using a simple graphic interface. Different pressures for the Fluika Pump are set to run the experiment, from 1,000 to 5,000 Pa The electrodes in the microfluidic channel are connected to a data acquisition system by a set of contact pins. As soon as the pressure starts being applied, the electronic reading is activated thanks to the controller of a myRIO National Instruments card. This tool communicates the fluidic pump and the electronic reading pins, through the computer. The sample fluid comes out of the reservoir at the set pressure and advances through the channel. As the fluid enters the microchannel and contacts the electrodes, it acts as a switch and sets the time required for the fluid front to reach each electrode pair. Using the time data and the distance between electrodes, it is possible to calculate the fluid front velocity. All these tests are performed at room temperature (∼24°C). The way these microfluidic elements are connected is displayed in **Figure 1**.

The experimental setup is comprised of a pumping source that connects to a fluid reservoir. The sample stored in the reservoir is pushed out through a connecting tube of radius r, and length l_t. The tube transporting is connected into the microfluidic channel of rectangular cross-section, of width ω and height *b*. The pressures acting on the system depicted in **Figure 1**, relate to each other as:

$$\Delta P = P_p + P_H - \Delta P_t - P_{cap} \tag{5}$$

Here ΔP, the pressure drop inside the microchannel, is the summation of all the pressures involved in the experiment. The set pressure P_p, is the pressure coming from the pumping source. The hydrostatic pressure P_H is the product of the density ρ, gravity g, and height of the fluid with respect to the channel height H; expressed as $P_H = \rho gH$. The pressure drop represented by the tube connection is ΔP_t. The capillary pressure, $P_{cap}$is defined as the resistance that the hydrophobic channel walls oppose to the fluid advancement. P_{cap} is dependent on the contact angle and the surface tension of the fluid, τ .

Thanks to the mass conservation principle, the flow inside the system is $Q = Q_t \rightarrow \omega b\dot{h} = \pi r^2 v_t$, where Q_t and v_t, are the flow and velocity inside the tube, respectively, and Q is the flow inside the channel (Méndez-Mora et al., 2021). The relation $v_t = \frac{\dot{h}\omega b}{\pi r^2}$ is valid for the coupled system and ΔP_t can be written as:

$$\Delta P_t = m2l_t \left(\frac{\omega b}{\pi r^2}\right)^n \left(\frac{1}{r^{1+n}}\right) \left(\frac{1}{n}+3\right)^n \dot{h}^n \tag{6}$$

Now, the effective pressure inside the system can be calculated as:

$$\begin{aligned} P_{eff} &= m2l_t \left(\frac{\omega b}{\pi r^2}\right)^n \left(\frac{1}{r^{1+n}}\right) \left(\frac{1}{n}+3\right)^n \dot{h}^n \\ &= m2l_t \left(\frac{\omega b^2}{\pi r^2}\right)^n \left(\frac{1}{r^{1+n}}\right) \left(\frac{1}{n}+3\right)^n \dot{\gamma}^n \end{aligned} \tag{7}$$

The mean front velocity $\dot{h}$, at each set pressure is experimentally obtained. By calculating velocity values and the channel dimensions, shear rate values are obtained. By fitting a curve for the relation between P_{eff} and $\dot{\gamma}$, the next relation is obtained:

$$P_{eff} = K(m,n)\dot{\gamma}^{n-1} \tag{8}$$

All the independent variables are grouped in K, which depends on the fluid properties (*m* and *n*) and the geometrical parameters of the system (ω, *b*, l_t, *r*),

$$K(m,n) = m2l_t \left(\frac{\omega b^2}{\pi r^2}\right)^n \left(\frac{1}{r^{1+n}}\right) \left(\frac{1}{n}+3\right)^n \tag{9}$$

Patients and Sample Preparation

A total of five patients with IDA, 15 patients with β-TT, and 10 normal controls (healthy individuals) were included in the study. The ages range for patients was from 18 to 95 years old. None of the patients had been transfused in the previous months. IDA was considered present when serum ferritin (SF) was <15 μg/L, or when SF was <30 μg/L, and transferrin saturation index (TSI) was <20%. IDA is present when (Hb < 12.0 g/dL in non-pregnant adult women and Hb < 13.0 g/dL in adult men). β-TT was diagnosed if mild microcytic anemia was present in absence of iron deficiency and the Hb analysis showed an increase in HbA2 (>3.5%) with or without an increase in Hb F (if present, <5%). All subjects in the control group had normal Hb levels, RBC indices, and iron parameters.

Samples were collected in ethylenediaminetetraacetic acid (EDTA) anticoagulant tubes during the course of routine analysis, shipped and stored at a temperature of 4°C, and processed within 24 h after the extraction. Complete blood count (CBC) parameters were assessed on a Sysmex XN-10 (Sysmex Corporation) analyzer. Total iron-binding capacity (TIBC), and serum ferritin (SF) were measured on Architect ci16000 System (Abbott Laboratories). Serum iron (SI), and (TIBC) by enzymatic methods, and SF by a two-step chemiluminescent micro-particle immunoassay (CMIA). The (TSI) was calculated as the ratio of iron to TIBC. Hb analysis was performed using high-performance liquid chromatography (HPLC) on a D-10 Dual A2/F/A1c (Bio-Rad Laboratories) or capillary electrophoresis on a Capillaris-2 Flex Piercing (Sebia). The use of the samples was authorized by the Bioethics Committee of the University of Barcelona (IRB 00003099) and the Ethics Committee of IJC [Comité Ético de Investigación Clínica (CEIC)].

Samples with different hematocrit concentrations were manually prepared by properly mixing plasma and RBC in the desired ratio. To obtain plasma, whole blood samples were centrifuged at 2,500 rpm for 5 min. The plasma that rests at the top is collected with a pipette. The different hematocrit

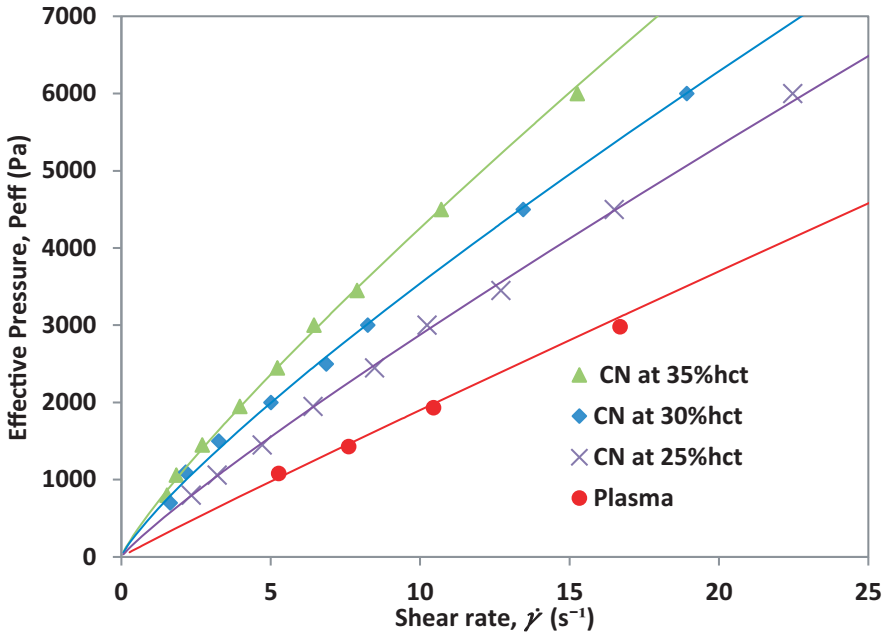

FIGURE 2 | Effective pressure vs. shear rate for blood from a healthy donor at different hematocrit levels.

concentrations hct (%) are prepared by taking plasma previously separated from whole blood and then adding to it the desired volume of RBCs corresponding to each hematocrit percentage. The sample volume prepared for each individual experiment is 500 μL.

RESULTS AND DISCUSSION

Blood Viscosity Normalization by Hematocrit

The hematocrit value in blood samples has a high impact on blood viscosity differences between different patients with the same blood conditions (Baskurt and Meiselman, 2003). Heterogeneity across patients regarding blood viscosity is expected to be present, mostly due to variations in hematocrit, hct (%). To observe differences in viscosity caused by blood abnormalities and be able to compare the blood viscosity curve of different patients, blood viscosity needs to be normalized to account for variations in hematocrit. To validate the normalization procedure, we first take a control sample (CN) from a healthy donor and prepare three different hct (%): 35%, 30%, and 25%. Viscosity is calculated for each hematocrit using Eq. 2. By using Eqs. 3, 4, the effects of hematocrit are removed. The effective pressure, P_{eff} as a function of the shear rate, $\dot{\gamma}$ for each prepared hematocrit and plasma are presented in **Figure 2**.

As seen in **Figure 2**, the shear rate, which is the normalization of the front velocity respect to the channel height, increases as the hct (%) value decreases under constant pressure conditions. Plasma has the highest front velocity when the same pressure is applied. Once the mean front velocity associated with each set pressure has been measured, it is possible to calculate the effective viscosity for the different hematocrit samples according to their plasma. The effective viscosity, η_{eff} is calculated using Eq. 3. The effective viscosity η_{eff} depends on plasma viscosity. The result is shown in **Figure 3**.

The normalization of viscosity according to hematocrit can be done by applying Eq. 4, which takes the highest hematocrit from the sample measured and compares it to the reduced hematocrit samples. Since the samples come from the same donor, if the equations were properly deduced, all curves must collapse onto a single viscosity curve for all the hematocrit levels, meaning that the differences observed before are only due to hematocrit

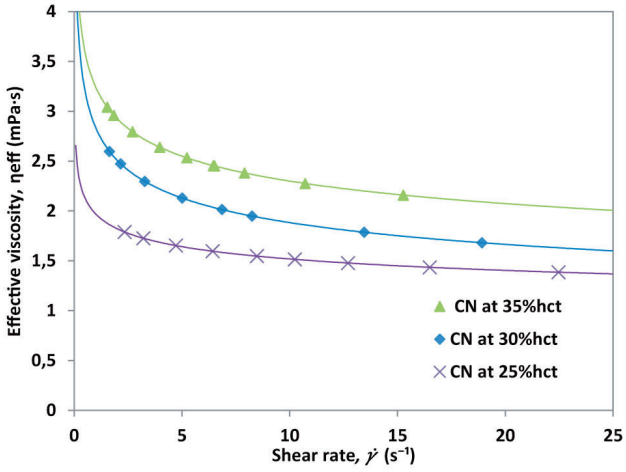

FIGURE 3 | Effective viscosity vs. shear rate for different hematocrit of healthy blood from a single healthy donor (CN).

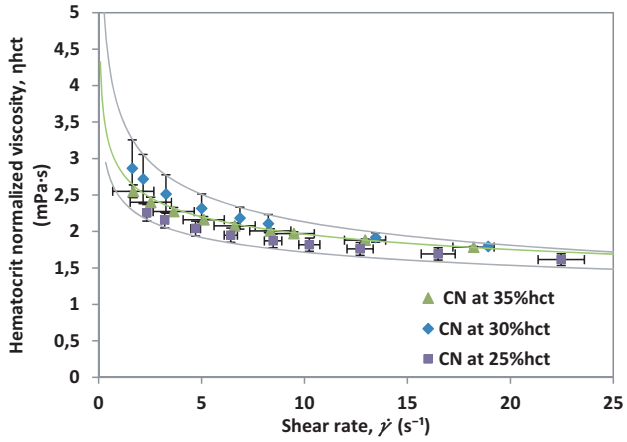

FIGURE 4 | Hematocrit normalized viscosity vs. shear rate for different hematocrit percentages from a single healthy donor (CN).

variations. The hematocrit normalized viscosity, η_{hct} is presented in **Figure 4**.

The results presented in **Figure 4**, indicate that the method employed is useful to remove effects caused by hematocrit differences. Furthermore, it will be helpful to contrast with samples that show differences related to RBCs count and abnormalities affecting the cells in suspension.

The shear rate response for each sample will depend, mostly, on the percentage of RBCs present in suspension. This response can also be affected by the presence of abnormalities developed by the blood cells, such as in β-TT. To validate the normalization of viscosity for non-healthy donors, the same experiment is conducted with β-TT samples. For validation, three hematocrit percentages (25%, 30%, and 35% hct) from a single β-TT patient are prepared. Note that β-TT samples are tested at lower $\dot{\gamma}$ to avoid hemolysis. The effective viscosity, η_{eff} is calculated for each hematocrit using Eq. 3. The resulting curves are presented in **Figure 5**.

After calculating η_{eff}, hematocrit normalized viscosity, η_{hct} is calculated using Eq. 4. By taking $\phi_{max} = 35\%$ hct, a normalized curve for β-TT is obtained, it is presented in **Figure 6**.

The results obtained in **Figures 4**, **6** demonstrate that the method presented makes it possible to normalize different samples by hematocrit, regardless of their health condition. Using this normalization, curves for diverse pathologies could be compared without the effects of different hematocrit levels. For comparison purposes, we contrast both curves (healthy donors and β-TT donors) in **Figure 7**, where the measurements obtained for each patient collapse into well differentiated curves.

Moreover, the method used to measure viscosity allows us to obtain points at low shear rates, giving us the advantage to observe the shear-thinning behavior of blood. This also makes it possible to observe that viscosity values are larger at low $\dot{\gamma}$ for β-TT than for healthy samples. The hematocrit normalized viscosity curves obtained in **Figure 6** for β-TT show higher viscosity than the control samples in **Figure 4**.

Study of Beta-Thalassemia Trait Samples

When beta-thalassemia is present, RBC indices show microcytic anemia. Thalassemia major is characterized by reduced Hb level (<7 g/dl), mean corpuscular volume (MCV) > 50 < 70 fL and mean corpuscular hemoglobin (MCH) > 12 < 20 pg. Thalassemia intermedia is characterized by Hb levels between 7 and 10 g/dl, MCV between 50 and 80 fL, and MCH between 16 and 24 pg. Thalassemia minor (BT Trait) is characterized by reduced MCV and MCH, with increased Hb A2 level (Galanello

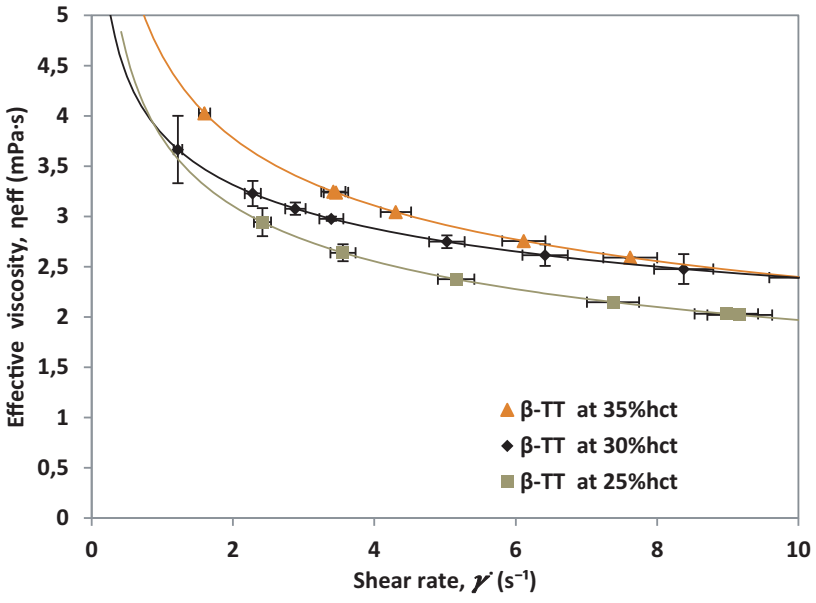

FIGURE 5 | Effective viscosity vs. shear rate from a patient with β-TT at three different RBCs concentrations.

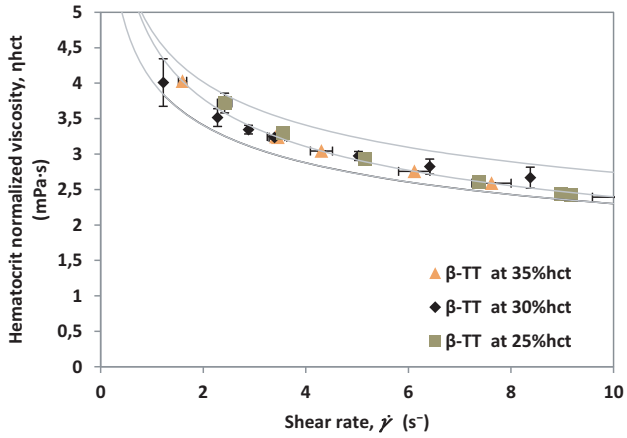

FIGURE 6 | Hematocrit normalized viscosity vs. shear rate for different hematocrit percentages from a single β-TT donor.

et al., 1989; Galanello and Origa, 2010). To carry out this study, whole blood samples from healthy donors and patients diagnosed with β-TT are used. To avoid effects caused by the variation of microcytosis, the samples were classified into three groups, according to their MCV, as presented in **Table 1**.

For each MCV group, five samples from different patients were tested. The effective viscosity was calculated with Eq. 3. The η_{hct}, obtained by using Eq. 4, for all the measured samples are presented in **Figure 8**. A tendency line indicating the average value obtained for each kind of sample is included.

TABLE 1 | Classification of β-TT and CN samples according to their MCV.

Group	Type	MCV (fL)
Lowest	Beta-thalassemia	58–65
Very low	Beta-thalassemia	66–70
Low	Beta-thalassemia	71–75
Normal volume	Healthy blood	90–92

As seen in **Figure 8**, β-TT samples with the smallest MCV (58–65 fL) have a higher viscosity than β-TT samples with higher MCV (66–70 fL and 71–75 fL). This indicates that the size of the erythrocyte may be affecting the viscosity measurement results. When two or more samples have equivalent hct (%) and different MCV, it implies that the number of RBCs is greater as lower is the MCV, which generates a greater number of cell rows in the flow when circulating through the microchannel. This effect, studied in detail for healthy red blood cells in a previous work (Lázaro et al., 2019) implies a stronger RBC interaction which leads to an increase in the magnitude of the viscosity, similar to the effect on viscosity observed in **Figure 8**. The parameters *m* and *n* describing the viscosity curves, calculated using Eq. 2, for each sample included in **Figure 8**, are presented in **Table 2**.

The β-TT samples with the smallest MCV values have the highest average *m* value, which equals the value of viscosity at $\dot{\gamma} = 1$. β-TT samples with MCV between 66 and 75 fL have very similar rheological parameters. The curves in **Figure 8** differ

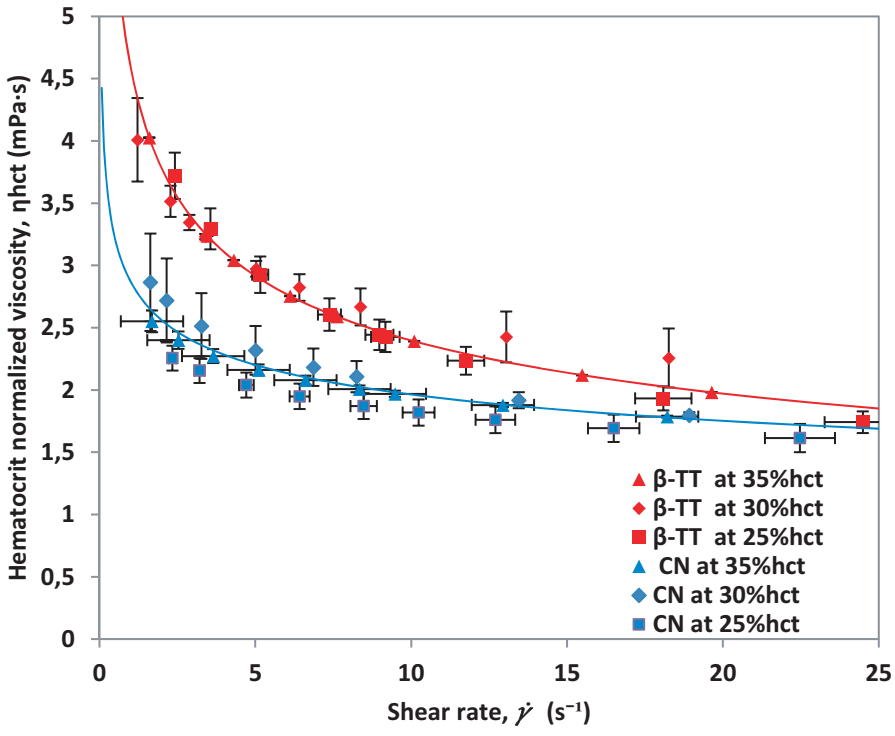

FIGURE 7 | Hematocrit normalized viscosity vs. shear rate for β-TT samples and healthy blood samples.

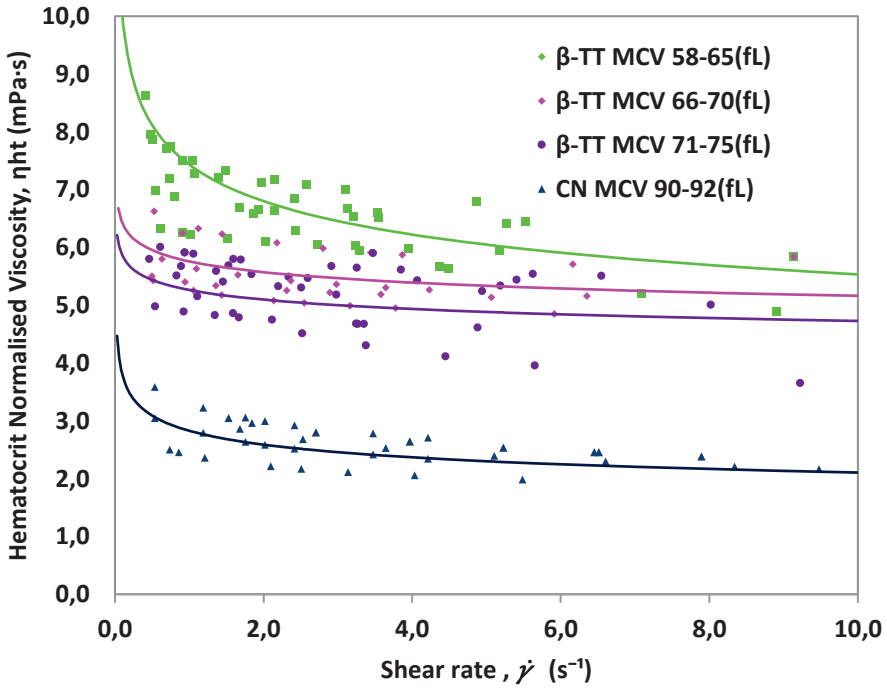

FIGURE 8 | Hematocrit normalized viscosity for β-TT and healthy control blood (CN) classified by MCV in **Table 1**. Whole blood is used in all cases.

TABLE 2 | Average values of *m* and *n* for healthy blood and β-TT samples according to MCV in fL.

Type	Group	*m*	*n*	MCV (fL)
β-TT	Lowest	7.4295	0.872	58–65
β-TT	Very low	5.7582	0.953	66–70
β-TT	Low	5.6265	0.955	71–75
CN	Normal volume	2.8272	0.880	90–92

Viscosity is normalized by hematocrit.

from those of healthy blood for two reasons, because the MCV is different, and because the mechanical properties of healthy and pathological red blood cells are different. We want to verify that alterations such as the changes in cell morphology and rigidity caused by the presence of β-TT, have a direct effect on the viscosity. The normal reference range for MCV is typically 80–100 fL, but this value is altered in some conditions.

Comparison of Blood Samples With Microcytic Red Blood Cells: Iron Deficiency Anemia and Beta-Thalassemia Trait

Anemia is a condition in which the number of red blood cells, and consequently their oxygen-carrying capacity, is insufficient to meet the physiologic needs of the body, and it is diagnosed as a decrease in the blood hemoglobin concentration (Hb) (Vitamin and Mineral Nutrition Information System (VMNIS), 2011). Iron deficiency limits the synthesis of heme, which in turn limits the synthesis of hemoglobin (Nagababu et al., 2008; DeLoughery, 2017), as it happens in β-TT as a result of a mutation. It is also characterized by decreased ferritin, and MCV, while total iron-binding capacity and red blood cell distribution are increased. Hypochromic red blood cells can be also be observed by visual inspection on a blood smear (Wagley, 1953; DeLoughery, 2017).

To confirm that the alterations seen in the viscosity of β-TT samples are not only attributed to microcytosis, we compared results obtained from samples with MCV of 66–75 fL to results of samples of IDA patients, with similar values of MCV. Using the same method as in **Figure 8**, we tested ten β-TT samples with MCV between 66 and 75 fL, five IDA samples with MCV between 66 and 79 fL and five samples from healthy donors with MCV between 90 and 92 fL. The results are shown in **Figure 9**.

Figure 9 shows that despite having similar MCV, β-TT and IDA samples have different viscosity patterns. The *m* and *n* parameters describing the viscosity curve for each group are presented in **Table 3**.

Iron deficiency anemia and β-TT curves have a different viscosity pattern even though they have similar MCV, indicating that pathological RBC conditions are reflected in viscosity, and they can be differentiated with the micro-rheometer. The IDA viscosity results show a much less Newtonian behavior; the *n* value differs more from 1 than that obtained with the β-TT samples. Since both diseases present Hb deficiency and RBCs with similar MCV, we conclude that the difference observed in viscosity between the β-TT and IDA cannot be considered a consequence of differences in RBC size. The higher viscosity obtained for the β-TT samples might be attributed to a greater rigidity in the RBC membrane. This can be caused by the excess of α chains that bind to the RBC membrane (DeLoughery, 2017; Payán-Pernía et al., 2021).

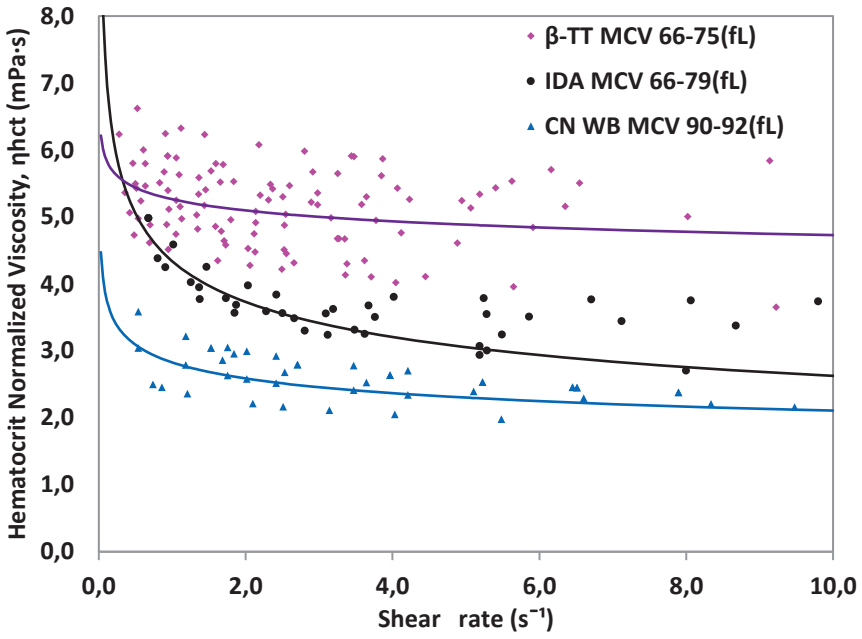

FIGURE 9 | Hematocrit normalized viscosity for ten samples of β-TT, five samples of IDA and five samples from healthy donors (CN). Whole blood in all cases.

TABLE 3 | Average values of *m* and *n* for IDA and samples according to MCV after normalizing by hematocrit.

Sample	Type	*m*	*n*	MCV fL
β-TT	Beta-thalassemia trait	5.6923	0.954	66–75
IDA	Iron deficiency anemia	4.3391	0.782	66–79
Control	Healthy blood	2.8272	0.880	90–92

Deformability Changes in Beta-Thalassemia Trait and Iron Deficiency Anemia

To verify that the differences in viscosity found between β-TT, IDA, and healthy donors are caused by changes in the properties of RBCs, we compare the results obtained with the LoRRCA ektacytometer between the samples. By measuring the elongation index, the LoRRCA can detect elasticity changes in single cells. The measurements performed determine elongation of a huge number of RBCs utilizing laser detection, at different osmolarity values, as illustrated in **Figure 10**.

The elongation index (EI) depicted in **Figure 10** is determined by the expression:

$$EI = \frac{A - B}{A + B} \tag{10}$$

where A and B are the major and minor dimensions of the RBC, respectively. With this test, it is possible to obtain a characteristic profile of each sample, according to the deformability of the RBCs as a function of osmolarity. These results do not depend on the hematocrit value of the samples.

Figure 11 shows the Osmoscan curve for the healthy subjects, IDA samples and β-TT samples. These results were previously described and differences between the three groups were statistically significant, reflecting deformability differences between these three states (Payán-Pernía et al., 2021). When β-TT is present, the ektacytometry curve is displaced to the left with respect to healthy RBC, revealing a decrease in the RBC deformability capacity.

The osmotic gradient ektacytometry analysis shown in **Figure 11** was performed using the Osmoscan module of the LoRRca MaxSis (RR Mechatronics). By measuring elongation index, LoRRCA can detect individual erythrocyte deformability in a mixture of RBCs. When β-TT is present, the ektacytometry curve is displaced to the left with respect to healthy RBC. IDA samples, however, show a shift that put them in between β-TT and the control samples. By observing **Figures 9**, **11**, it is possible to establish that alterations in RBC wall rigidity can be translated into viscosity changes. After normalizing the hct (%), the viscosity of samples for IDA falls below the viscosity of β-TT and over the viscosity of control samples. As seen in **Figure 10**, β-TT samples have a higher viscosity than control samples. This is consistent with samples that appear to have a left shift in their ektacytometry measurements. Observing the two results together lets us have a bigger picture of the effects of single cell rheology. LoRRCA is very powerful at finding individual differences within cells. The results obtained in this study, demonstrate that our method can detect the presence of these alterations through the study of the fluid front rheology of the whole blood. Therefore, the method proposed can distinguish differences between healthy blood and blood affected by pathologies that modify the red blood cell rheology. Changes in viscosity seem to have a direct relation to individual cells' changes in β-TT.

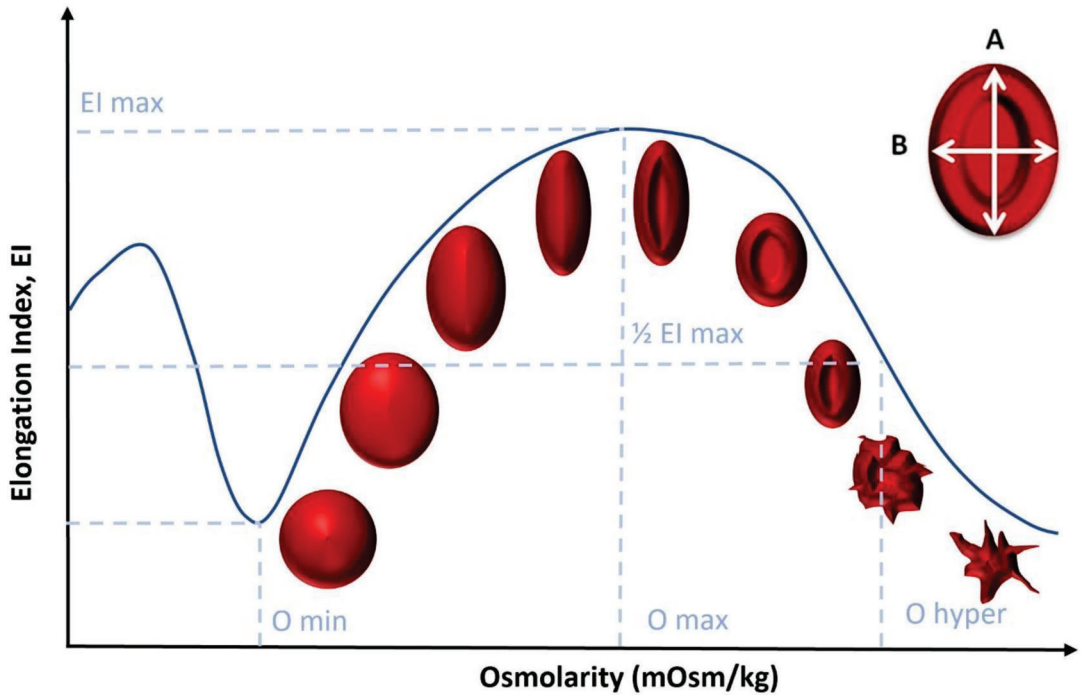

FIGURE 10 | RBC elongation index evolution as the osmolarity increases using LoRRCA.

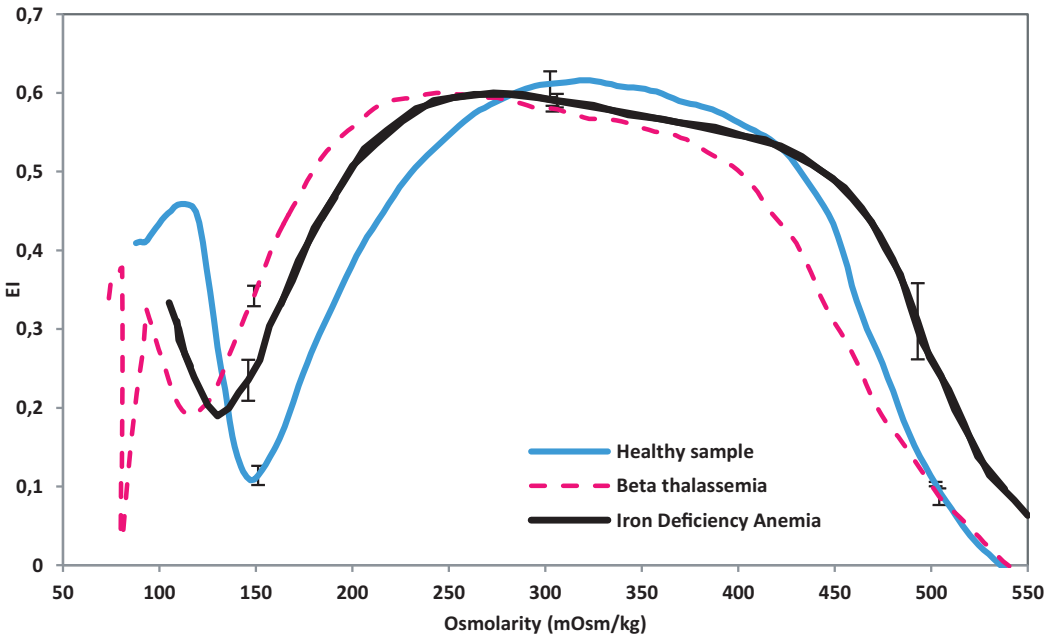

FIGURE 11 | Osmoscan curve obtained from LoRRCA. Ten samples of β-TT, five samples of IDA and five samples from healthy donors were used. IDA curve adapted from Payán-Pernía et al. (2021).

CONCLUSION

Through this study, we have seen that the micro-rheometer presented here has great potential as a diagnostic tool for hematological diseases. This has been demonstrated by differentiating three sets of samples, from healthy donors, β-TT and IDA patients. Using a microfluidic method we have been able to distinguish between samples with different RBCs abnormalities, despite the fact that the donors of each set have different ages and distinct hct (%). Comparison with a

standardized red blood cell elasticity characterization method, the LoRRCA ektacytometer, has allowed us to verify that our findings were correct.

The sample characterization techniques used in this paper are based on the use of normalized curves, differentiated for distinct pathologies. Using a mathematical method for hematocrit normalization (Trejo-Soto and Hernández-Machado, 2021), a single viscosity curve is calculated for healthy donors. Using the same method, a normalized viscosity curve of β-TT is obtained. The hematocrit normalized viscosity η_{hct}, does not contain the effects caused by hematocrit levels. This was made to perform an adequate comparison between samples from the same or different patients, both in healthy and non-healthy conditions, independent of their hct (%). Thanks to this method, we obtained curves with clearly differentiated parameters for healthy blood, β-TT, and IDA.

The experimental results herein obtained, show that the MCV seems to affect the viscosity of the samples. Samples with distinct MCV did not follow the normalized curve path. Once the samples were segregated into three groups based on their MCV, a clear pattern showed up. As a general observation, lower MCV accounted for higher viscosity values. For this motive, it is reasonable to do a comparison between β-TT and IDA samples with similar MCV only. It was found, however, that even at comparable MCV and after hematocrit normalization, β-TT has a higher viscosity than both IDA and control samples. This difference in viscosity might be caused by differences in the affected deformation capability of RBCs and the membrane changes caused by the α chains disorders that characterize β-TT (Payán-Pernía et al., 2021).

Reasoning on the basis that high blood viscosity might be caused by changes in the RBC wall rigidity, it is plausible to infer that these differences may be reflected in an ektacytometry analysis. It was found that the osmotic gradient curve obtained by LoRRCA for IDA samples is shifted to the left of the curve for healthy donors and to the right of the curve for β-TT patients, reflecting that the rigidity of RBCs in IDA samples is higher than that of healthy donors, and at the same time smaller than the rigidity of RBCs in β-TT samples. This is compatible with the viscosity results in which IDA samples have a lower viscosity than β-TT patients and higher than healthy donors. The differences observed in viscosity between the samples analyzed could be a result of changes in the rigidity of the RBCs when β-TT is present (Payán-Pernía et al., 2021).

The general conclusion of this work is that the micro-rheometer is a promising tool for early detection of different blood diseases can differentiate between two types of blood diseases, β-TT and IDA, regardless their hematocrit level and the presence of microcytosis. It has been also demonstrated that blood viscosity is an accurate indicator of the blood health condition, especially when the pathology in study targets the RBC and affects its shape, deformation capacity and size. Furthermore, the samples show a clear difference when compared to healthy samples, by using the microrheology technique described. A correct characterization on blood has been made through an adequate setup, without the need of complex equipment and with just a small sample. At the same time, the results obtained are comparable to those delivered by standard diagnostic techniques, such as LoRRCA, which is the gold standard method for ektacytometry evaluation of RBCs. The results obtained are important for the development of a functional point-of-care diagnosis device for the fast and effective detection of hemolytic anemias such as IDA and β-TT. PoC devices can provide a very positive outcome for populations located in remote areas of the world where the access to resources is limited. Diagnostic tools that provide fast and reliable results constitute an easy way to keep the follow up of patients up to date, without the need of commuting and the use of hospital facilities. In the near future, a cheap, easy to use, and small device can be used for both triage in hospitals and at home by patients suffering of RBC altering conditions such IDA and β-TT.

DATA AVAILABILITY STATEMENT

The original contributions presented in the study are included in the article/supplementary material, further inquiries can be directed to the corresponding author/s.

ETHICS STATEMENT

The studies involving human participants were reviewed and approved by the Ethics Committee of IJC [Comité Ético de Investigación Clínica (CEIC)] and the Bioethics Committee of the University of Barcelona (IRB 00003099). The patients/participants provided their written informed consent to participate in this study.

AUTHOR CONTRIBUTIONS

AH-M and J-LV-C conceived the study. LM-M and MC-F performed the experiments, processed the data, and wrote the manuscript. CR-L and JF-T helped to interpret the results. EK collected and analyzed the samples prepared by IH-R and CM-I. SP-P, TA, AH-M, MC-F, and CT-S supervised the research work and revised the results and discussion. All authors contributed to the manuscript revision, read, and approved the submitted version.

FUNDING

LM-M and JF-T received funding from programs Doctorat Industrial (2018 DI 068) and (2018 DI 064) from AGAUR (Generalitat de Catalunya). EK receives funding from Institut Josep Carreras (IJC) under program Equality Plus, project number 2019-1-TR01-KA202-076789. TA acknowledges funding under grant numbers MTM2015-71509-C2-1-R and MDM-2014-0445. TA has been partially funded by the CERCA Program of the Generalitat de Catalunya. AH-M acknowledges funding under project FIS2016-78883-C2-1P, Ministerio de Ciencia e Innovacion (Spain) under project PID2019-106063GB-100 and

3. Acknowledgements

I would like to thank my advisors Aurora Hernández Machado and Tomás Alarcón for all the guidance and help during this long journey. My tutor, Mauricio Moreno, opened his laboratory doors to me where I got started into the world of clean rooms and the fabrication of microfluidic channels. Thanks for all the time and effort you all three put into teaching me how to always find a way.

I am especially grateful to Claudia Trejo and John González, who transmitted part of their lab expertise and experience so I could survive after a long day of experiments and get good samples! I could not forget to add Maria Cabello to that mix; thank you for your mentoring when we had to put hands on data and start writing interesting articles.

I extend my gratitude to Hernando del Portillo and his team at IS Global. Marc, thank you for all your dedication and care put into all the experiments.

To the friends made along the way, which made my time in the lab and outside of it more interesting: Pamela, Josep, Andreu, Carla, and Minerva. Working together has been awesome, but building a friendship with all of you has been even better.

And lastly, I dedicate this thesis to my dear family. My mom and dad, who put all their human and material resources into giving me all the support and love that I needed so I can pursue the career path I wanted, even beyond their means. To my brothers, David, and Daniel, who always cheered me up when rainy days came along. To my aunt Lourdes and uncle Ferenc, who became my second parents when I crossed the Atlantic Ocean, 10 years ago, to start this adventure in Barcelona. To my beloved husband Alessandro and my lovely baby Ulisse, who gave me the inspiration I needed to complete my thesis. Mamma, Papà, Davide, Angela, Ettore e Rosa, questi ringraziamenti sono dedicati anche a voi! Una mención especial a mis tías Angela y Mili, por siempre creer en mí y en mi talento.

Finally, I would like to dedicate my thesis as an inspiration to the future generations, my cousins Matheo, Rosanna, and Gabriel, hoping to be a good model for you in your professional path.